NEW METHODS FOR CONTROLLING COUPLING EFFECTS IN CAVITY MAGNON-POLARITON SYSTEMS

BY:

PAUL HYDE

A thesis submitted to the Faculty of Graduate Studies of:

THE UNIVERSITY OF MANITOBA

in partial fulfilment of the requirements of the degree of:

DOCTOR OF PHILOSOPHY

Department of Physics and Astronomy

University of Manitoba

Winnipeg

Abstract

By mediating interactions between light and matter, polaritons offer a window into the fundamental nature of material dynamics and have enabled the development of modern wireless communications technologies. In microwave cavity systems, confined photons interacting with coherent magnon excitations can produce high rates of light-matter coupling and allow the properties of the cavity magnon-polaritons coupling these systems to be studied in new detail. In this dissertation, we employ microwave cavity systems to develop new methods for controlling the coupling properties of cavity magnon-polaritons. We demonstrate that magnon-polariton coupling can be used to indirectly couple two orthogonal cavity resonance modes together, using their mutual coupling to a resonant magnetic system as a bridge across which energy and dynamic information can be transferred. The strength of this indirect coupling can be controlled through tuning the resonant properties of the individual cavity or magnon systems, and in future may be employed to link many photon and magnon systems together. Using a specially designed cavity system, we are also able to compare the coupling effects seen in cavity magnon-polariton systems to those observed in polariton systems involving non-magnetic excitations. These measurements show that the dynamics of polariton coupling are common throughout all systems, but that in cavity magnon-polariton systems the averaged permeability of the entire cavity-material volume plays an important role in determining the strength of coupling effects. We further study the properties of magnon-polariton coupling in systems where the magnon mode has been excited to amplitudes where non-linear effects become significant. We find that bistable resonance properties related to those observed in uncoupled non-linear magnon systems are present in these systems, and that further bistable behaviours unique to coupled systems can be created by controlling the individual properties of the cavity or magnon systems. By uncovering new properties of light-matter coupling in cavity magnon-polariton systems and new methods for controlling this coupling, this dissertation reveals a host of potential applications for these systems in future data storage and processing technologies, and additionally shows that the observed coupling dynamics can be extended into other varieties of polariton systems involving non-magnetic excitations.

Contents

List of Tables

List of Figures

List of Publications

The following list of publications were developed during my doctoral studies and serve as the basis of my thesis report:

Indirect coupling between two cavity modes via ferromagnetic resonance

Paul Hyde, Lihui Bai, Michael Harder, Christophe Match, and Can-Ming Hu

Appl. Phys. Lett. **109**, 152405 (2016)

Linking magnon-cavity strong coupling to magnon-polaritons through effective permeability

Paul Hyde, Lihui Bai, Michael Harder, Christopher Dyck, and Can-Ming Hu

Physical Review B **95**, 094416 (2017)

Direct measurement of foldover in cavity magnon-polariton systems

P. Hyde, B.M. Yao, Y.S. Gui, Guo-Qiang Zhang, J.Q. You, and C.-M. Hu

Physical Review B **98**, 174423 (2018)

I was also involved with the development of these further publications during my doctoral studies. Although they will not be discussed in detail in this thesis report, their topics are closely related to those covered and will be discussed where relevant.

Spin rectification for collinear and noncollinear magnetization and external magnetic field configurations

Y. Huo, L.H. Bai, *P. Hyde*, Y.Z. Wu, and C.-M. Hu

Physical Review B **91**, 174430 (2015)

Spin dynamical phase and antiresonance in a strongly coupled magnon-photon system

Michael Harder, *Paul Hyde*, Lihui Bai, Christophe Match, and Can-Ming Hu

Physical Review B **94**, 054403 (2016)

Topological properties of a coupled spin-photon system induced by damping

Michael Harder, Lihui Bai, *Paul Hyde*, and Can-Ming Hu

Physical Review B **95**, 214411 (2017)

Cavity Mediated Manipulation of Distant Spin Currents Using a Cavity-Magnon-Polariton

Lihui Bai, Michael Harder, *Paul Hyde*, Zhaohui Zhang, Can-Ming Hu, Y.P. Chen, and John Q. Xiao

Phys. Rev. Lett. **118**, 217201 (2017)

Acknowledgements

Over the course of my studies I have had the opportunity to work and collaborate with numerous people, whose assistance and support have been invaluable for the completion of this thesis. First and foremost I would like to thank my advisor, Prof. Can-Ming Hu, for his guidance throughout my graduate studies. From first encouraging me to begin my graduate studies, to leading me through new and innovative fields of research, and finally helping me to make my own published contributions to these fields, his support was always felt. I thank him for allowing me to work with his exceptional research group and for always encouraging me to push further in my research.

I was extremely fortunate to work with many talented individuals in the Dynamics Spintronics Group during my studies. Of special note I need to thank Lihui Bai and Michael Harder for their valuable help in designing and performing experiments, developing theoretical models, and parsing my research into publishable results. I also must thank Yongsheng Gui for his invaluable assistance throughout my graduate studies, and especially for his help during many tedious months of thesis writing. Many other members of the Dynamic Spintronics Group, both past and present, have made positive contributions to my research and life during my studies. I would like to thank them all for sharing their insights and friendship with me. I wish all of them the very best in their future academic and professional careers.

My academic career was made possible by the outstanding environment of the Department of Physics and Astronomy at the University of Manitoba, and I feel an obligation to thank the numerous professors who guided me towards a deeper understanding of the physical world and who each contributed to my academic development. I should also thank the support staff within the department, for their assistance in navigating the sometimes overwhelming world of academic research. Thanks must also go to the members of my PhD supervisory committee, Prof. Byron Southern, Prof. Cyrus Shafai, and Prof. Christopher Wiebe, for taking the time to review my work and for providing valuable feedback on it. Appreciation also goes to the University of Manitoba Graduate Fund, whose financial support was most welcome during my studies.

Finally, I would like to reserve the most special thanks to my family, for their love and encouragement during my university career. I was extremely fortunate to have the unwavering support of my parents through all stages of my life, and their guidance has played a significant role in shaping the person I am today. Through teaching me the value of hard work and critical thinking, they set me on a path towards my current career and have been instrumental to its success. My grandmother also played no small part in helping me through my university studies; her deliveries of baked goods were always a welcome reminder of home during long months of study and I shall always be grateful for her love and support. There have been many others whose support and guidance has led me to where I am today, and I cannot list them all, but their help has not been forgotten and I cannot thank them enough. A final thanks to Justin Yanick, for being the best of friends and the coolest of dudes.

I have been very fortunate to live in an age and country which allows me to pursue my full potential through university studies. I recognize that many others of no less talent and ability than me may not have had this opportunity due to political, social, or financial factors, and hope that one day all may be free to follow their dreams and pursue knowledge in all areas of life.

Chapter 1

Introduction

One of the most remarkable things about modern physics is the difference between physical reactions at large and small scales. While at macroscopic scales objects move and interact following mostly intuitive Newtonian dynamics, at quantum scales a new dynamics regime takes over and the motion of particles becomes governed by probability functions with interactions taking place via the transmission of gauge bosons such as photons (electromagnetic forces) or gluons (strong interaction). In situations where these quantum interactions are dominant a whole new wealth of material behaviours can occur, producing such remarkable effects such as superconductivity[1], particle tunnelling[2], quantum entanglement[3], and magnetoresistance effects[4]. These effects of these quantum behaviours are often unintuitive from a Newtonian perspective, but in many material systems the interplay of these behaviours has led (and continues to lead) to many previously unknown physical properties[5][6]. For this reason the field of condensed matter research is today one of the largest branches of physical studies, and, due to the rapid integration of these quantum material properties into electronics and communications systems, is also a research field driving the development of multi-billion dollar industries.

Within the field of condensed matter physics, one of the most important interactions is that which occurs between electromagnetic (EM) radiation and magnetic materials. Although the general properties of magnetism have been known and studied for hundreds of years[7], the unique interactions these materials can have with EM radiation only began to be studied in the 20th century when they were found to strongly absorb radiation at certain frequencies[8][9]. Later research showed that this EM absorption is a result of interactions between photon excitations and the magnetic spin polarizations of a magnet, the latter of which undergo collective Larmor precession at some resonance frequencies[10][11]. A theoretical understanding of ferromagnetic resonance (FMR) was first developed in 1935 by Lev Landau and Evengy Lifshitz[12], describing how periodic magnetic motions can be excited by EM fields. Further developments by T.L. Gilbert in 1955 expanded Landau and Lifshitz's model to include the effects of damping forces[13]. This model of resonant ferromagnetic behaviour, termed the Landau-Lifshitz-Gilbert (LLG) model, permitted the dynamics and characteristics of ferromagnetic (FM) materials (such as the effects of demagnetization, anisotropy, and damping forces) to be studied in unprecedented detail by describing the absorption and dispersion of EM radiation incident on the material near resonance[14].

The basis of FMR lies in the general principles of ferromagnetism, where exchange interactions between neighbouring magnetic moments results in parallel moment configurations having lower energies[15]. When any of these moments is influenced by an incoming photon the resonant effects produced are not limited to the single moment which receives this energy, but are spread through the entire ferromagnetic sample through exchange interactions between moments. These collective FM excitations can be considered a form of quasiparticle, called a magnon, which carries energy and spin polarization through the lattice structures of FM materials. These magnon excitations include the resonant motions described by the LLG model[16], but also includes inhomogeneous excitations such as spin waves which may propagate through material structures[17]. Magnons are generally excited in FM materials through the absorption of EM photons and can similarly lose energy via radiative damping, emitting energy (via magnetic induction) back into the environment as EM photons[18]. The interaction between photons and magnons during these energy exchanges are governed by another form of quasiparticle called magnon-polaritons (MPs), which exist as superpositions of magnon and photon excited states[19]. Combining the quantum electrodynamic properties of photons with the magnetic properties of magnons, magnon-polaritons exist at an exciting crossroads of physical research, holding the keys to converting information and energy between photon and magnon systems.

As the effects of an individual photon excitation on a magnon system are generally quite small, individual MP interactions can be difficult to detect. Thus in order to study MPs, and the interactions they represent, a method must be found to increase their rate of production within a system. By entrapping the photons involved in these interactions within a cavity resonator, a continuous source of photon-magnon interactions can be produced with a relatively low power input. The closed system of the cavity resonator also provides a further benefit; as the resonant EM fields (photons) within the cavity drive resonant motion (magnons) within an FM material, and the resonant motion of the FM material generates EM field emissions (through inductive radiation) in the cavity system, a coupled feedback loop is created. Within the enclosed cavity system the photon and magnon resonance states both become influenced by each other. In cavity and magnon systems with low damping and high coupling, energy losses are minimized and energy may be traded between photon and magnon excitations many times. This continual back-and-forth flow of energy via photon-magnon interactions in a closed system creates a new hybridized quasiparticle, the Cavity Magnon-Polariton (CMP). Unlike most MP systems, where a constant stream of input photons are required to observe polariton coupling effects, in closed cavity systems CMPs can be continually generated with minimal photon input. This allows the cavity system to be measured separately from any input photons, simplifying measurements and making the effects of polariton coupling clearer to observe. These advantages permit CMP systems to give an unprecedented view of the basic properties of magnon-photon interactions.

Early measurements of coupling in CMP systems was limited by the competing demands placed on the magnon subsystems involved; they had to consist of macroscopic sized samples to achieve strong coupling to cavity photons, but needed to be small enough that they could be uniformly excited by a microwave field into a single homogeneous resonant mode. It wasn't until 2010 that Soykal and Flattè showed theoretically that CMP systems could be created using low-damping, high-spin-density, ferromagnetic materials up to millimetre scales in size; utilizing the fact that the dynamics of single-domain magnetic crystals can be approximated as those of a single stable macrospin[20][21]. In 2013 the first demonstration of strong CMP coupling was realized by Huebl *et al.*, who placed a supercooled Yttrium-Iron-Garnet (YIG) sample in a planar superconducting resonator[22]. This demonstration ignited a flurry of activity in CMP studies, and soon coupled CMP systems were being realized at room temperature[23], in 3D microwave cavities[24][25], and using split-ring resonators[26][27][28][29][30]. Although YIG continues to be one of the most widely used magnetic samples in CMP systems, due to its combination of low damping and high spin density, magnon resonances in other magnetic samples have also been used to produce CMPs, such as gadollinium-iron-garnet (GdIG)[31], lithium ferrite[32], and the chiral magnetic insulator Cu_2OSeO_3[33].

Beyond simply demonstrating CMP coupling, recent studies have rapidly advanced the scope of CMP studies; to the ultrastrong CMP coupling regime at the quantum limit of hybridization[34][35][36] and to CMP coupling involving spin waves[37][38][39][40], qubit resonators[24][41], multiple cavity modes[42], and multiple magnon modes[43][44][45][46]. Developments into new spintronic methods to electrically probe the magnon response during CMP coupling have also introduced new techniques for studying these systems[37][43][47]. With improved CMP systems and measurement techniques new CMP coupling effects have been discovered and analysed, including; exceptional points of the CMP eigenspectrum[52][53], coherent perfect absorption[53], and the impacts of non-linear Kerr effects[54][55][56]. The wealth of possible applications of CMP systems is already being explored, despite the field being less than a decade old, with on-chip devices demonstrating voltage control of CMP coupling[52], electromagnetically induced transparency being demonstrated[29][53], quantum information systems being developed involving magnon dark modes coupled to a cavity system[45], the design of CMP systems capable of converting microwave signals to optical frequencies[54], and CMP coupling involving active resonators with extremely high Q factors[55]. With the vast majority of new developments in CMP theory and technology taking place only in the past few years the field of CMP coupling appears to be only warming up, with the new discoveries and applications listed here to be used in the near future to discover more about these intriguing systems and the fundamental nature of photon-magnon coupling.

1.1 Thesis Relation to Recent Works

Studying the fundamental properties of photon-magnon coupling through CMP systems has already revealed many new coupling behaviours and applications, as have been listed above. To further research in this field new methods for tuning CMP systems during coupling must be developed to explore new dynamic behaviours. Broadly speaking, tuning in CMP systems can involve changing the properties of the magnon resonance, the cavity resonance, or the coupling forces between them. Tuning any one of these properties is often difficult, since (aside from external field control of magnon resonance) they are largely dependent on material or structural properties of the resonant subsystems. During my doctoral research I was involved with works exploring new topological properties of CMP systems via tuning the magnetization of a magnon system relative to resonant cavity fields and allowing switching between strong and weak coupling regimes[52], and with works using spintronic probes to study how CMP coupling can be used to manipulate the spin properties of multiple distantly separated magnon systems[43]. Both of these studies show how different forms of manipulating CMP systems can reveal new physical insights and applications. However, the basis of my thesis report will discuss contributions made to CMP studies through the development and application of new methods to tune coupled CMP systems through unique cavity and FM resonator effects. The new dynamic behaviours and applications found in these works will be discussed in greater detail in the body of this report, which is organized as follows;

Chapter 2: This chapter introduces the key concepts and theories necessary for the understanding of magnon-photon coupling and the production of CMPs. Emphasis is placed first on the description of individual FM and cavity resonators, before a discussion of how resonant modes in these systems can influence each other to produce a coupled CMP system. Theoretically, coupled CMPs are described using both the quantum Jaynes-Cummings model as well as a classical coupled harmonic oscillator model, which are shown to produce equivalent results for the coupling cases we study. A brief description of the input-output theory is then presented and used to derive the transmission and reflection properties of the CMP system from the coupled dynamic equations calculated using these models.

Chapter 3: This chapter extends the models of CMP coupling to systems involving multiple photon resonance modes simultaneously coupling to a single magnon mode. Although previous works have shown that multiple magnon subsystems can be simultaneously coupled to a single cavity mode to create a chain of indirectly coupled FM systems, our work extends beyond this by indirectly linking not multiple subsystems, but different orthogonal excitation modes of a single cavity subsystem. By designing a cylindrical microwave cavity with tunable height we were able to achieve simultaneous strong coupling between each cavity mode and the Kittel resonance mode of a YIG sample. During this indirect coupling the resonant motion of each individual cavity excitation is seen to influence the dynamics of the other orthogonal cavity mode; this is evidenced by the aligning of the two cavity modes to either in-phase or out-of-phase motion (depending on the coupled mode) during indirect coupling. Finally, by tuning the height of the cavity, we show that the strength of the indirect coupling between cavity modes is inversely related to the difference between the resonance frequencies of the two modes. Thus we show that the dynamics of indirect coupling can be tuned by controlling either the dynamic phase or frequency of two indirectly coupled resonators relative to each other. The results discussed in this chapter are published in Appl. Phys. Lett. **109**, 152405 (2016)[42].

Chapter 4: This chapter explores the connection between magnon-polariton (MP) coupling produced in cavity systems and similar light-matter coupling produced by polaritons at different photon frequencies. In coupled CMP systems, polaritons are produced by coupling between microwave cavity photons and resonant magnon modes in a magnetic material; at higher frequencies phonon-polaritons can be produced in material samples by coupling infrared photons with collective lattice vibrations termed phonons, and exciton-polaritons can be produced by coupling optical photons with excitations produced by electron holes or quantum wells within a material. In measurements of phonon-polariton and exciton-polariton systems, one of the most notable features of polariton coupling is the creation of a frequency gap, where no coupled modes can exist, as the frequency of the resonant photons is shifted. This gap, termed the polariton gap, is a result of changes to the electromagnetic properties of a material during coupling to photon modes. As most cavity systems have no means to adjust the properties of their resonant states, similar measurements cannot be performed on CMP systems, and thus no polariton gap has been measured in them. Although their coupled subsystems might differ, the light-matter interactions experienced in all polariton systems are expected to be the same, and many features of polariton coupling are expected to be shared. Thus the absence of a polariton gap in measurements of cavity MPs has produced speculation that there are factors influencing coupling in cavity systems which are absent in other systems. To settle this speculation we develop a model describing polariton coupling in CMP systems, which is based on the experimental differences between them and other polariton coupled systems. This model accounts for the much reduced polariton gap seen in CMP systems and is seen to agree with other models of polariton coupling. Using the adjustable cavity developed for the previous chapter, we perform the first measurements of the polariton gap in a CMP system; showing that a small polariton gap is present in the system, whose magnitude agrees with that predicted by our coupling model. Using this model we are additionally able to show that the polariton coupling gap commonly measured in phonon-polariton and exciton-poalriton systems is closely related to the Rabi oscillation gap typically measured in CMP systems, confirming that the coupling forces present in all varieties of polariton systems are the same. The results discussed in this chapter are published in Physical Review B **95**, 094416 (2017)[57].

Chapter 5: This chapter explores the impacts of non-linear Kerr effects in resonant FM systems involved in CMP coupling. These Kerr effects are produced at high resonant amplitudes and can generate remarkable effects on the dynamics of FM resonance, producing bistable resonance lineshapes. By exciting resonance in a YIG sample to high amplitudes during CMP coupling, these bistable resonant effects are found to extend into the CMP system. Combining models of non-linear dynamics in FM resonators with models of CMP coupling between cavity and FM systems, we are able to describe the lineshapes produced by non-linear CMP systems and predict the boundaries of bistable regions of resonance. The ability to control these bistable regions through tuning the driving microwave frequency, external field strength, or applied microwave power shows that non-linear CMP systems could provide versatile platforms for new switching or data storage technologies. Additionally, since our model describing these non-linear light-matter interactions is not necessarily limited to FM systems, the non-linear dynamics seen in our coupled system should be reproducible across many other areas of physics and engineering. The results discussed in this chapter are published in Physical Review B **98**, 174423 (2018)[56].

Chapter 6: This chapter will conclude the dissertation, summarizing the results of the previous chapters and exploring possible areas of future research based on their results.

Chapter 2

Theoretical Background

2.1 Ferromagnetic Resonance

The interactions between EM fields and material dynamics can take many complex forms, and is the basis of many fields of study in condensed matter physics. As a consequence of the numerous fundamental physical phenomena discovered and described by these studies, EM fields and their interactions with magnetic materials now form the basis of modern telecommunications and data processing technologies which have had a major impact on the way modern society shares and analyses information[58][59][60]. One of the earliest studied forms of interaction between EM fields and materials was in ferromagnets, which can be induced into resonant behaviour (ferromagnetic resonance, FMR) in the presence of on oscillating EM field matching their precession frequency[61]. Indeed, despite resonant ferromagnetic behaviour having been studied since the early 20th century, new physical behaviours and effects are still actively studied today[62][63][64], including in the chapters of this thesis. One of the first models to describe ferromagnetic resonance was developed in 1935 by Lev Landau and Evgeny Lifshitz[12]. The Landau-Lifshitz model they developed follows from the Heisenberg equation of motion for a collection of spin operators (with a magnetization, $\vec{M}$, being produced by Zeeman-type interactions) as they interact with a magnetic field $\vec{H}_i$;

$$\frac{d\vec{M}}{dt} = -\gamma(\vec{M} \times \vec{H}_i) \tag{2.1.1}$$

Here the term $\gamma = \mu_0 g_e |q|/2m$ is termed the gyromagnetic ratio of each ferromagnetic spin, where q and m are the charge and mass of the spin moment and g_e is the Landé g factor (which is approximately

2 for a free electron, but may deviate from this value in ferromagnetic materials)[65][66]. If the magnetic field experienced by magnetic moments within the material, $\vec{H}_i$, is produced by an externally applied static field, we can see from Eq. 2.1.1 that the interactions between $\vec{M}$ and $\vec{H}_i$ will generate a torque on the spin moment. This torque will cause the magnetic moment, $\vec{M}$, to precess about H_i; if the magnetic moment does not experience any damping effects to its motion this precession could continue indefinitely. However all physical materials exhibit some non-zero damping effects (mainly due to spin-lattice or spin-spin relaxation interactions)[67][68], which will cause the precessional motion to spiral inwards and eventually cause $\vec{M}$ to align with the applied field. By applying an additional oscillating field to the material, such that $\vec{H}_i = \vec{H}_{i0} + \vec{h}_i e^{-i\omega t}$, the effects of damping in the system can be countered and the precessional motion of the spin moment can be continually driven to resonant behaviour, a process known as ferromagnetic resonance (FMR)[69][70].

2.1.1 Landau-Lifshitz-Gilbert Description

Although the Landau-Lifshitz model of FMR is able to describe the physical origin of resonant behaviour in magnetic materials, without accounting for damping effects the dynamics of FMR behaviour near resonant frequencies could still not be described. For a fuller description of FMR dynamics a damping-inclusive model of ferromagnetic resonance was developed by T.L. Gilbert in 1955, termed the Landau-Lifshitz-Gilbert (LLG) equation[13]. In this model the effects of damping can be introduced to the Landau-Lifshitz equation through the addition of a damping term dependent on the precession of $\vec{M}$, resulting in;

$$\frac{d\vec{M}}{dt} = -\gamma(\vec{M} \times \vec{H}_i) + \frac{\alpha}{|\vec{M}|}\left(\vec{M} \times \frac{d\vec{M}}{dt}\right) \tag{2.1.2}$$

where α is called the Gilbert damping parameter and has a microscopic origin in spin-orbit interactions within the FM material[71]. The magnitude of α is temperature dependent in magnetic materials, typically increasing as the material's temperature is increased towards its Curie Point[72][73]. The Gilbert damping term in the LLG equation can be seen to produce a torque on $\vec{M}$ perpendicular to its precessional motion, which will force $\vec{M}$ towards the orientation of the applied static field $\vec{H}_{i0}$. As the magnitude of this damping term is dependent on the precession of the magnetic moments, systems with large precession amplitudes (large $d\vec{M}/dt$) will experience strong damping effects while systems with smaller precession amplitudes will experience less damping losses.

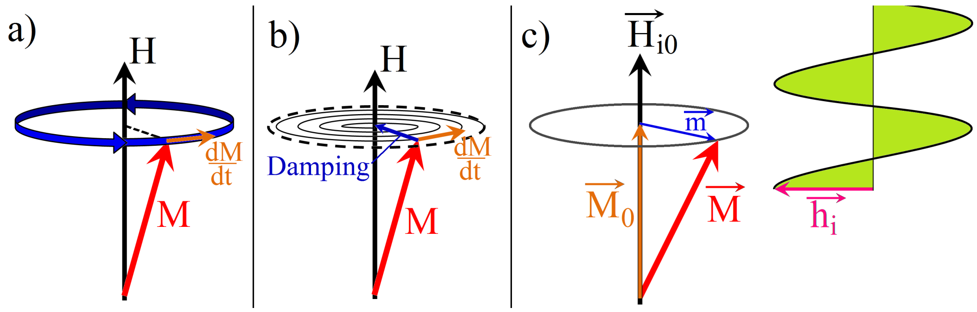

Figure 2.1: **(a)** A diagram of the precessional motion of a spin moment $\vec{M}$ about an applied field $\vec{H}$ in the absence of damping. **(b)** The behaviour of the same moment when the effects of damping are considered, with the damping resulting in a spiralling decay of the precessional motion. **(c)** A diagram of the vector components of a spin moment, $\vec{M}$, during resonant motion as it is being polarized and driven by static ($\vec{H}_{i0}$) and oscillating ($\vec{h}_i$). The magnetic spin and field vectors in this diagram are given in Eqs. 2.1.3 and 2.1.4.

As it only needs to be strong enough to counter damping losses, an applied driving field with frequency ω will generally be much smaller than any static field applied to the material. Applying this driving field allows us to write the field experienced by the magnetic moments, $\vec{H}_i$, as a combination of a large applied static field $\vec{H}_{i0}$ and the smaller oscillatory driving field $\vec{h}_i$. Because it is mainly the component of the applied driving field which is perpendicular to the magnetization $\vec{M}$ which generates torque on the moments, we can define $\vec{H}_{i0}$ as lying parallel to the $\hat{z}$ axis, with the expectation that $\vec{h}_i$ will have components in the $\hat{x}-\hat{y}$ plane to generate precession when $\vec{M}$ is polarized mainly along the $\hat{z}$ axis. We can similarly separate the magnetic moment of the material, $\vec{M}$, into a large $\hat{z}$ polarization component produced by the presence of a strong static field along this axis, with smaller oscillations in the $\hat{x}-\hat{y}$ plane produced by its precessional motion. Thus we write;

$$\vec{H}_i = \vec{H}_{i0} + \vec{h}_i e^{-i\omega t} = (0, 0, H_{i0}) + (h_{ix}, h_{iy}, 0)e^{-i\omega t} \tag{2.1.3}$$

$$\vec{M} = \vec{M}_0 + \vec{m} e^{-i\omega t} = (0, 0, M_0) + (m_x, m_y, 0)e^{-i\omega t} \tag{2.1.4}$$

Inserting these expressions for $\vec{H}_i$ and $\vec{M}$ into the LLG equation will now allow us to describe the motion of the magnetic moments in response to the driving field. After performing the cross products and removing negligibly small terms of order $\vec{m} \times \vec{h}_i$, we find;

$$\vec{m} = \frac{\gamma}{i\omega}(\vec{M}_0 \times \vec{h}_i + \vec{m} \times \vec{H}_{i0}) + \frac{\alpha}{M_0}(\vec{M}_0 \times \vec{m}) \tag{2.1.5}$$

Having arrived at this expression, we can now separate the applied fields into two distinct elements. The first element ($\vec{H}$ or $\vec{h}$) is composed of the field externally applied to the sample (applied static field and driving field), while the second element will be produced by demagnetization fields within the sample. These demagnetization fields will tend to oppose externally applied fields and will have strengths dependent on the shape of the sample; as the shape dependent anisotropy energy of a magnetized ferromagnetic sample is minimized when more of its constituent moments are aligned parallel to the sample's surface, demagnetization fields tend to strongly oppose magnetization along shorter dimensions of a sample (hard axes) and more weakly oppose magnetization along longer dimensions (easy axes). The effects of these demagnetization fields can be expressed by amending $\vec{H}_{i0}$ and $\vec{h}_i$ to;

$$h_{ik} = h_k - N_k m_k \tag{2.1.6}$$

$$H_{i0k} = H_k - N_k M_k \tag{2.1.7}$$

Above, the k subscript is used to indicate components along the k^{th} axis of a field vector and value N_k describes the demagnetization factor along the k^{th} axis of the sample. It should clarified that in Eq. 2.1.6 we define $\vec{h}_i$ to be the oscillating field experienced by moments inside the sample, while $\vec{h}$ is the oscillating field applied to the sample; similarly in Eq. 2.1.7 we define $\vec{H}_{i0}$ to be the static field experienced inside the sample, and $\vec{H}$ to be that static field externally applied to the sample. The difference between these internal and external fields is a result of the effects of demagnetization forces. The demagnetization factors within a sample are highly dependent on the geometry of a sample and will obey the sum rule $N_x + N_y + N_z = 1$, with the factor for any given axis generally dependent on the length of the sample along that axis[74]. Thus for an infinitely thin wire sample parallel to the $\hat{z}$ axis we will have $N_x = N_y = 0.5$ and $N_z = 0$, for an infinite planar sample in the $\hat{x} - \hat{y}$ plane we would have $N_x = N_y = 0$ and $N_z = 1$, and for a spherical sample $N_x = N_y = N_z = 1/3$. Applying these amended fields to Eq. 2.1.5 and simplifying the resulting expression now leads us to the Polder tensor, χ, an equation relating the oscillating magnetization of the ferromagnetic sample to the applied driving field[75];

$$\vec{m} = \chi \vec{h} = \begin{pmatrix} \chi_{xx} & i\chi_{xy} & 0 \\ -i\chi_{xy} & \chi_{yy} & 0 \\ 0 & 0 & 0 \end{pmatrix} \vec{h} \tag{2.1.8}$$

The matrix elements of the Polder tensor are can be expressed as;

$$\chi_{xx} = (D + iL)\frac{\gamma M_0[M_0 N_y + (H - N_z M_0)]}{\alpha\omega[2(H - N_z M_0) + M_0(N_z + N_y)]} \tag{2.1.9}$$

$$\chi_{xy} = -(D + iL)\frac{M_0}{\alpha[2(H - N_z M_0) + M_0(N_z + N_y)]} \tag{2.1.10}$$

$$\chi_{yy} = (D + iL)\frac{\gamma M_0[M_0 N_x + (H - N_z M_0)]}{\alpha\omega[2(H - N_z M_0) + M_0(N_z + N_y)]} \tag{2.1.11}$$

We can see in these Polder tensor elements that the resonant behaviour of magnetic moments within a material will be highly dependent on the geometric properties of the bulk material sample being excited (which determine the N_k demagnetization parameters). The terms L and D in Eqs. 2.1.9, 2.1.10, and 2.1.11 are respectively termed the Lorentzian and Dispersive lineshape amplitudes of the resonant motion. These amplitudes determine the shape of the precession amplitude peaks near resonance and have opposite symmetries about the resonant field, they are defined by;

$$L = \frac{\Delta H^2}{(H - H_r)^2 + \Delta H^2} \tag{2.1.12}$$

$$D = \frac{\Delta H(H - H_r)}{(H - H_r)^2 + \Delta H^2} \tag{2.1.13}$$

where we have defined H_r, the external static field strength which must be applied to the sample to excite resonance at a frequency ω, according to the Kittel resonance formula[76];

$$\omega^2 = \gamma^2[H_r + M_0(N_y - N_z)][H_r + M_0(N_x - N_z)] \tag{2.1.14}$$

and ΔH has been defined as a measure of the width of the measured resonant lineshape near H_r, which

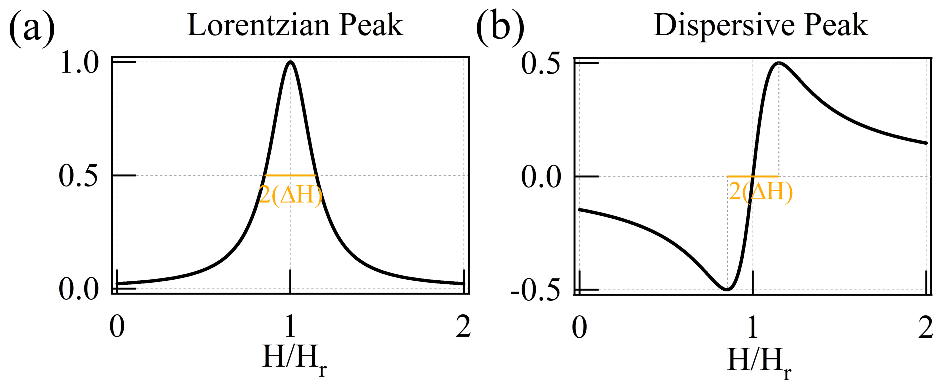

Figure 2.2: Plots of the resonant peak shapes near resonance for a system with **(a)** an entirely Lorentzian amplitude and **(b)** an entirely Dispersive amplitude. The equations describing these amplitude peak shapes are given in Eqs. 2.1.12 and 2.1.13.

is closely tied with damping effects in the resonant system. For an entirely Lorentzian lineshape ($D = 0$) ΔH will be half the field width of the lineshape, measured at half its maximum amplitude [see Fig. 2.2(a)]. For a completely dispersive lineshape ($L = 0$) this ΔH value will represent the field displacement between H_r and the position of the positive or negative amplitude peaks [see Fig. 2.2(b)]. The value of ΔH can be expressed as;

$$\Delta H = \frac{\alpha\omega}{\gamma} \frac{2H + M_0(N_x + N_y - 2N_z)}{H + H_r + M_0(N_x + N_y - 2N_z)} \tag{2.1.15}$$

For $H \approx H_r$ we can see that this expression will reduce to $\Delta H \approx \alpha\omega/\gamma$. It should be briefly noted here that an underlying assumption of the calculations used to derive the Polder tensor here is that the amplitude of the precessional motion of the magnetic moments is assumed to be small ($M_z \gg m_x, m_y$). This assumption has been applied to our calculations after the addition of the demagnetization fields to our calculations in Eqs. 2.1.6 and 2.1.7 as $M_z \approx M_0$ to simplify the resulting calculations. This assumption of low precession amplitude is found to be valid for many resonant systems. The dynamic motion of the magnetic moments for higher amplitude precession can be calculated using $M_z = \sqrt{M_0^2 - m_x^2 - m_y^2}$ (this is done later in Sec. 5.2) and results in non-linear behaviour such as lineshape foldover and bistable mode solutions[57][77].

2.1.2 Applications of FMR and Magnon Excitations

Physically, the resonant behaviours described by FMR are only one variety of the many possible magnon excitations in magnetic materials. In the uniform FMR mode, often referred to as the Kittel mode, the resonant motion of the magnetic moments throughout the material is homogeneous and can be excited by the application of a uniform oscillating field. Closely related to resonant motion in magnetic materials are magnon excitations known as spin waves. Unlike resonant magnon modes, in which all spin moments within a material are excited into related oscillatory motion, spin waves are inhomogeneous excitations which can propagate and carry spin polarization through a material's spin lattice structure. The most basic spin wave excitation would involve a uniformly polarized collection of spins where one spin is suddenly flipped to oppose the others. As the system is allowed to evolve with time the polarization of this single flipped spin will spread through the rest of the spin population through exchange interactions over the spin lattice, travelling in a fashion similar to ripples on a pond (in 3 dimensions) after a pebble is tossed in. Eventually lattice damping effects will cause the rippling effects to decay and the system will stabilize. The wavelength and excitation frequency of spin waves are broadly dependent on the strength of exchange interactions between spins on a lattice, but will vary depending on the external dimensions and polarization of a magnetic sample. One form of spin waves are produced in thin film samples when edge pining effects can result in standing spin waves propagating perpendicular to the film's surface. These waves are termed Perpendicular Standing Spin Waves (PSSWs), and have dispersions which can be calculated by the addition of an additional exchange interaction term to the LLG equation[78]. Ignoring damping effects these PSSW frequency dispersions are;

$$\omega_r^2 = \gamma^2 \left(H + M_0 + \frac{2Ak_z^2}{\mu_0 M_0} \right) \left(H + \frac{2Ak_z^2}{\mu_0 M_0} \right) \qquad \text{PSSWs for } \vec{M}_0 \text{ in-plane} \tag{2.1.16}$$

$$\omega_r = \gamma \left(H - M_0 + \frac{2Ak_z^2}{\mu_0 M_0} \right) \qquad \text{PSSWs for } \vec{M}_0 \text{ out-of-plane} \tag{2.1.17}$$

where we have defined A as the exchange stiffness constant between spins in the material[79], and k_z to be the propagation vector of the wave perpendicular to the surface of the film. Observing these PSSW dispersions we see that for the case of $k_z = 0$ the dispersions of the Kittel FMR mode is reproduced, showing that resonant FMR modes within magnetic systems can be described as a special case of spin wave excitation. We can also note that these spin wave modes will have higher excitation frequencies than the Kittel FMR mode, and will thus require more energy to excite. Other forms of spin waves include Damon-Eshbach waves (surface spin waves), and backward/forward volume modes, which have similar dispersions to PSSWs but will spread evanescently through the material's structure[80].

Due to reasons of easy generation and detection, much research has historically focussed on studying the Kittel FMR mode in magnetic materials. In addition to microwave absorption effects, resonant behaviour is responsible for the spin rectification effect[81], in which a DC current is generated from an AC input current in a resonant FM system. This effect has been used to develop a spin-torque diode[82], as well as novel imaging techniques utilizing both the amplitude and phase information of EM signals[83][84]. The later development of spin pumping further advanced the realm of possible uses for resonant behaviour[85]; using the resonance in a magnetic material to 'pump' spin polarization into a neighbouring material. This new technique represented a significant advancement in the field of spintronics, which works to develop techniques to transfer polarization without charge currents and the Joule heating effects they bring. The field of spintronics itself is closely tied to studies of spin waves, connecting the propagation of spin waves in magnetic materials to the transport of spin currents in non-magnetic materials[86].

Experimentally, techniques have been developed to detect and study spin waves. These techniques include several varieties of time-domain measurements, which detect the dynamics of magnetic moments when spin waves are present. In Pulse-Inductive Microwave Magnetometry (PIMM) measurements a pulsed EM excitation is used to produce spin waves in a magnetic sample, and a stripline placed next to the sample measures inductive induced voltages generated by spin wave motion[87][88]. Alternatively, spatially resolved Magneto-Optic Kerr Effect (MOKE) measurements employ a femtosecond laser to both excite and detect spin waves; using the changes in the polarization and intensity of light reflected from a magnetized surface to detect spin wave dynamics[89][90]. More recently, X-ray Detected Magnetic Resonance (XDMR) systems have been developed to use x-ray magnetic circular dichroism to probe local spin magnetization in samples and directly observe spin-torque induced spin waves[91][92]. Several additional techniques are also employed to study spin waves based on microwave reflection/transmission/absorption spectra in the field and frequency domain. These techniques can make use of Brillouin Light Scattering (BLS) effects[93][94] in addition to other direct measurements of the $\omega(k)$ spin wave dispersion[95]. Techniques involving spin rectification have also been developed to detect rectified DC signals produced by spin waves[96]. Rectification techniques benefit in that the material carrying spin waves is itself used as the detector; enabling simplified data analysis and increased sensitivity when used together with lock-in techniques[97].

2.2 CMP Coupling and Yttrium Iron Garnet

Although many magnetic materials are able to sustain magnon excitations when exposed to certain combinations of static and EM fields, only a select number possess the certain characteristics which make them ideal for use in coupled CMP systems. These characteristics include a strong coherence between magnetic spins during excitation, strong coupling to EM photons, a relatively high Curie temperature, and a low material damping[20]. A strong interspin coherence is crucial as magnon resonance modes must have a stronger coupling to photon resonance modes than the decoherence rate between magnetic spins to achieve coherent CMP coupling[21]. This interspin coherence assures that all spins of a magnetic system are excited into the same resonant state, and couple equivalently to any incident photons. Magnetic systems with low interspin coherence may form multiple polarization domains and during excitation may produce multiple resonant magnon states. During CMP coupling the presence of multiple magnon modes within a material may produce inhomogeneous dynamics throughout the system and complicate the behaviour of photons interacting with these modes. To ensure homogeneous coherence within a magnetic sample during excitation, the polarization fields must be stronger than any depolarization fields throughout a sample's structure. For this reason magnetic samples used in CMP systems are generally spherical in shape to limit the effects of shape demagnetization fields, though strong external fields applied to a material may overcome demagnetization fields and allow other sample geometries to be excited into a uniform mode[43][47], and commonly consist of crystalline ferromagnetic materials. In small single-crystal samples, the uniform effects of crystalline magnetic anisotropy fields act to ensure uniform dynamics among magnetic spins within the crystal and suppress inhomogeneous behaviours[21]. Once coherently excited into a uniform Kittel resonance mode, the multiple spin systems of a magnetic sample can be approximated as a single macrospin system exhibiting photon-magnon coupling strengths orders of magnitude higher than single spins while maintaining coherence to photon excitations during CMP coupling[20]. This observation is the basis of most CMP systems, and directly led to the rapid development of the field after its publication.

The damping forces in a magnetic material are also an important factor in CMP coupling, as in the coupling process energy must be exchanged between photon and magnon systems before it is lost to damping. The strength of coupling within CMP systems is commonly defined relative to the system's cooperativity,

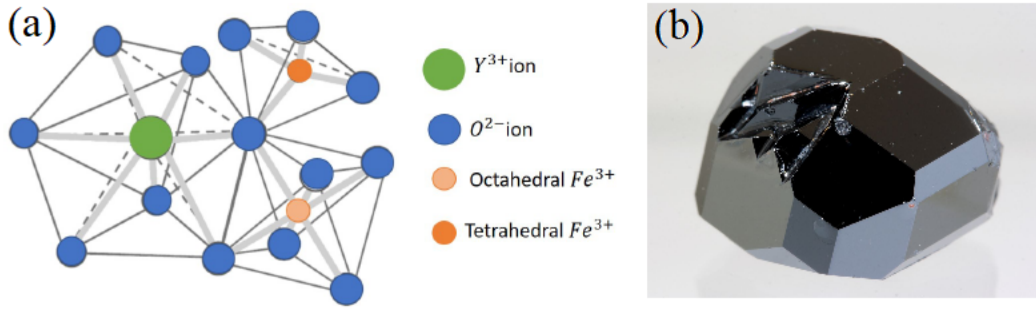

Figure 2.3: **(a)** A schematic diagram of the crystal structure of YIG as described in Ref. [106]. **(b)** A picture of a large crystalline YIG sample[107].

C, defined as[43];

$$C = \frac{g_c^2}{\alpha\beta} \tag{2.2.1}$$

where α refers to the strength of damping in the magnetic material, β is the cavity damping strength, and g_c defines the strength of the coupling forces between the cavity and magnon systems. Strong coupling in CMP systems occurs in cases where $C > 1$; in these cases hybridization between the magnon and photon modes will result in a splitting of the resonant CMP modes during coupling. In systems where $C < 1$, other coupling effects such as electromagnetically induced transparency[103][104] or the Purcell effect[105], may occur which will influence the behaviour of CMP modes during coupling but will not produce the mode splitting indicative of the production of CMPs within the coupled system. We see from Eq. 2.2.1 that producing a strongly coupled CMP system requires not only strong coupling between magnon and cavity systems, but also damping effects small enough to not overcome these coupling forces.

To fulfil the material demands required to produce strongly coupled CMP systems, many studies[43][45][54]

Compound Formula	$Fe_5O_{12}Y_3$	
Crystal Structure	Cubic	[110]
Unit Cell Lattice Parameter	1.2376 nm	[110]
Atoms per unit cell	80	[110]
Curie Temperature	560 K	[111]
Spin Density	2.1×10^{22} cm^{-3}	[112]
Saturation Magnetization	$\sim$178 mT	[42]
Damping Parameter	$\sim 10^{-5}$	[113][110]

Table 2.1: Typical material characteristics of crystalline Yttrium Iron Garnet

have relied on the ferrimagnetic oxide known as Yttrium Iron Garnet (YIG) with a chemical formula $Y_3Fe_5O_{12}$. The crystal structure of YIG is shown in Fig. 2.3; here we can see oxygen ions (O^{2-}) form dodecahedron, octahedron, and tetrahedron structures within the crystal, with a yttrium ion (Y^{3+}) occupying the centre of the dodecahedron formation. At the centres of the octahedron and tetrahedron formations are iron ions (Fe^{3+}), which will be polarized in opposing directions with different spin magnitudes depending on which formation they are centred in[106]. These Fe^{3+} ions are thus responsible for YIG's ferrimagnetic behaviour, resulting in a material which can be polarized similar to ferromagnets but has a relatively high spin density. In addition to its high spin density ($\sim 10^{27}m^{-3}$)[108][109], YIG also has a very low damping factor relative to most ferromagnets ($\sim 10^{-5}$)[113][110], allowing stronger coupling effects to be achieved with smaller samples. The garnet crystal structure of YIG is also a benefit to CMP studies, as it allows homogeneous crystal macrospins to be created up to several millimetres in scale.

In the CMP coupling experiments detailed in this dissertation, we used single-crystal YIG spheres purchased from Ferrisphere Inc. to generate our magnon modes. These spheres were of 1 mm diameter had a surface roughness of approximately 50μm. The resonant frequency, ω, of the Kittel mode of these spherical samples is related to the strength of an applied field, H, through the relation;

$$\omega/2\pi = \gamma(H + H_A) \tag{2.2.2}$$

Where γ is the gyromagnetic ratio of the YIG moments and H_A represents the effect of anisotropy fields (both shape and crystalline) within the sample. The values of γ and H_A for a YIG sample can be determined by placing it within a microwave cavity resonator and fitting the relation between ω and H to Eq. 2.2.2 at frequencies far from any cavity modes (to eliminate any coupling effects). The Gilbert damping parameter of the sample can be determined at an H field value far from coupling as the half-width at half-maximum of the absorption lineshape at resonance. Measurements performed on the samples showed they had a saturation magnetization of $\mu_0 M_0$= 178 mT, and a gyromagnetic ratio of γ= 28 x 2π μ_0GHz/T. Among the samples, Gilbert damping factors were typically between 0.8-1.5 x 10^{-5}. During measurements these samples exhibited strong, clear, resonance behaviours in the Kittel mode, indicating that they are homogeneous crystal samples and can be approximated as magnetic macrospins during CMP coupling.

The measured values of H_A tend to vary between experiments, due mainly to our use of a Hall probe to measure the applied field H. Although Eq. 2.2.2 assumes that H is measured at the position of the YIG sample, practical considerations (electrical connections) require that the Hall probe be positioned outside of the microwave cavity. Thus the H value measured by the probe will differ from the applied field felt by the sample, which will modify the measured value of H_A found by fitting the linear dispersion of Kittel mode to Eq. 2.2.2 far from coupling. Because the relative positions of the YIG sample and the Hall probe may change between experiments, this results in varying H_A values for different experiments, even when similar samples are used. However, because the value of H_A is independent of ω and H variations, the main consequence of a perceived change to H_A is to shift the Kittel mode distribution to slightly higher or lower applied field values (typically on the order of $|\mu_0 \mathrm{H}| \sim 30$ mT), which does not affect our experimental results.

2.3 Cavity Resonators

2.3.1 General Description and Characteristics

In essence, a cavity resonator is a device designed to store EM radiation as resonant modes within a certain volume. These devices operate by reflecting EM radiation at their outer edges through sudden permittivity/permeability shifts, resulting in the formation of stable resonance modes within the cavity[114]. The interior volume of the cavity can either be left empty (air-filled) or filled with a low-loss dielectric material (allowing higher energy resonant modes to be stored within the cavity)[115]. The resonant frequency and field dispersions of the modes able to form within a cavity resonator are highly dependent the cavity's structure and composition. Determining the resonant properties of these modes involves calculating the electric field, $\vec{E}$, and related magnetic field, $\vec{H}$, dispersions which satisfy Maxwell's Equations for electric and magnetic fields throughout the volume of the cavity[116] in the absence of free currents and charges;

$$\vec{\nabla} \cdot \vec{E} = 0 \tag{2.3.1}$$

$$\vec{\nabla} \cdot \mu_0 \vec{H} = 0 \tag{2.3.2}$$

$$\vec{\nabla} \times \vec{E} = -\mu_0 \frac{\partial \vec{H}}{\partial t} \tag{2.3.3}$$

$$\vec{\nabla} \times \vec{H} = \epsilon_0 \frac{\partial \vec{E}}{\partial t} \tag{2.3.4}$$

The $\vec{E}$ and $\vec{H}$ fields are further restricted by boundary conditions at the edges of the cavity. Resonant cavity states can be divided into two mode types depending on the field dispersions at the boundaries; resonant transverse electric (TE) modes are created when the $\vec{E}$ field components tangential to the inner surface of the cavity are equal to zero at the boundaries, while resonant transverse magnetic (TM) modes are created when the $\vec{H}$ field components tangential to the inner surface of the cavity are equal to zero at the boundaries. These two boundary restrictions are not mutually exclusive, and in some cavity designs (notably rectangular cavities) resonant modes can be created which satisfy both conditions and are termed transverse electromagnetic (TEM) modes[114]. The solutions to Eqs. 2.3.1 and 2.3.2 which satisfy these boundary conditions are not necessarily analytical for cavities of arbitrarily shaped volumes. However, for cavities which have certain symmetric properties (rectangular, cylindrical, spherical volumes) the field dispersion solutions can be fairly easily solved[117]. These solutions give us several unique $\vec{E}$ and $\vec{H}$ field dispersions which correlate to stable resonance modes within the cavity, each having a specific resonance frequency. Although the total number of resonance modes able to be excited within a cavity resonator is unlimited, many high energy modes are simply higher order solutions of low energy modes. This allows us to relate these modes through a set of positive integers known as mode numbers (presented here as m, n, and p). For a rectangular cavity of dimensions a, b, and d, the resonant frequency of the stable TEM modes within the cavity can be described by[114];

$$f_{mnp} = \frac{1}{2\pi\sqrt{\epsilon\mu}} \sqrt{\left(\frac{m\pi}{a}\right)^2 + \left(\frac{n\pi}{b}\right)^2 + \left(\frac{p\pi}{d}\right)^2} \tag{2.3.5}$$

where ϵ and μ are the permittivity and permeability of the material filling the cavity. For a cylindrical cavity of radius R and length L, solving Eq. 2.3.1 will produce distinct sets of TE and TM resonance modes, described by[114];

$$f_{mnp} = \frac{1}{2\pi\sqrt{\epsilon\mu}} \sqrt{\left(\frac{X_{mn}}{R}\right)^2 + \left(\frac{p\pi}{L}\right)^2} \qquad \text{for TE Modes} \tag{2.3.6}$$

$$f_{mnp} = \frac{1}{2\pi\sqrt{\epsilon\mu}} \sqrt{\left(\frac{X'_{mn}}{R}\right)^2 + \left(\frac{p\pi}{L}\right)^2} \qquad \text{for TM Modes} \tag{2.3.7}$$

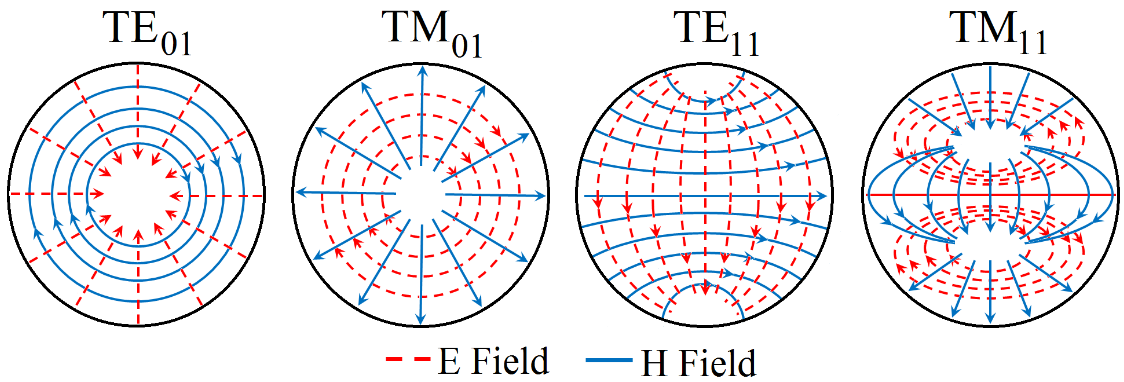

Figure 2.4: Diagrams of the EM field distributions for some of the lower order modes in a cylindrical waveguide. These diagrams only show dispersions along the cross section of the waveguide, moving along the length of the waveguide these dispersions will change periodically depending on the axial component of the excited mode.

where in the above equations X_{mn} refers to the nth zero of the mth Bessel function, and X'_{mn} refers to the nth zero of the *derivative* of the mth Bessel function. Some transverse $\vec{E}$ and $\vec{H}$ field dispersions of the first few TE and TM modes for a cylindrical waveguide are shown in Fig. 2.4; here we see that the dispersions of resonant cavity modes can vary significantly, even between modes having similar resonant frequencies. Although in theory cavity resonators can be designed to have any possible shape or dimensions, in practice most have interior volumes that are either rectangular or cylindrical in shape. This is due to these structures being both simpler to manufacture and having structural symmetries which make their resonant mode distributions easy to calculate[114].

In addition to the field and frequency dispersions of its resonant modes, another important parameter of cavity resonators is their quality factor, Q. This value is defined as the ratio of the total EM energy stored in the cavity during resonance, W_{stored}, to the power loss in the cavity per cycle, P_L[117];

$$Q = \frac{\omega W_{stored}}{P_L} \tag{2.3.8}$$

with ω being the resonant frequency of the mode within the cavity. Losses in well-designed cavities are chiefly due to a combination of conductive losses from currents travelling on the surfaces of the cavity, and dielectric losses produced in the material filling the cavity[118]. To minimize conductive losses cavity resonators are typically made of, or coated by, highly conductive metals such as aluminium, copper, silver, or gold. Dielectric losses can be minimized by filling the cavity with a low-loss dielectric material, air being one simple and effective choice. Within a general cavity system, the conductive, P_{cond}, and dielectric, P_{diel}, losses can be calculated as[118];

$$P_{cond} = \frac{1}{2}\int_{walls} |\vec{J_s}|^2 R_s ds \tag{2.3.9}$$

$$P_{diel} = \frac{1}{2}\int_{V} \vec{J}\cdot\vec{E}*dV \tag{2.3.10}$$

with $\vec{J_s}$ representing the surface current on the walls of the cavity, R_s the surface resistance of the cavity walls, and $\vec{J}$ the electrical current within the dielectric filling of the cavity. By design, the total power loss in most cavities is much smaller than the amount of energy they can store; typical Q-factors can range from a few hundred for simple cavities, up to values of several thousand for specially designed low-loss cavities[119][120].

2.3.2 Measuring Material Properties using Cavity Resonators

In practice, one of the major uses of cavity resonators is in the measurement of material properties through cavity perturbation measurements[121]. The basis of cavity perturbation theory is that very small physical changes to the interior of a cavity can be detected through the effects they have on the measured properties of the cavity. These physical changes can be produced by either changing the dimensions/shape of the cavity (using adjustable walls, for example) or by inserting a small material sample into the cavity[122]. For practical reasons, due to the difficulty of designing adjustable cavities and the ease of placing small samples into a cavity, the latter method is more typically used in measuring material properties. In order to determine the effects of small perturbations to the cavity system, it is necessary to calculate the EM field distributions throughout the perturbed cavity system; while this may be possible in some cases, it is often non-trivial. To get around this limitation, the basic underlying assumption of cavity perturbation theory is employed. This assumption states that for very small changes to the cavity system, the EM field distributions within the cavity will remain essentially unchanged[114]. This makes calculating the material properties of small samples within the system significantly simpler, as with this assumption the only changes to the cavity system upon the introduction of the material sample will be the permittivity/permeability changes at the sample's location.

When performing cavity perturbation measurements the resonant frequency of the cavity is measured before and after a small material sample has been inserted into the cavity. The shift in resonant frequency of the cavity modes is then used to characterize the the material which has been inserted. As seen in Eqs. 2.3.5, 2.3.6, and 2.3.7, the resonant frequencies of cavity modes have relatively simple relations to the electromagnetic properties of the volume within the cavity. This relation and the fact that the resonant frequency of cavity modes can be easily and accurately measured (typically as peaks or dips in the S_{21} transmission of the cavity) make measuring shifts in the resonant mode frequencies of a cavity an ideal tool to characterize material perturbations within the cavity[117]. If we consider initially a general unperturbed cavity, such as that shown in Fig. 2.5(a), the unperturbed electric, $\vec{E}_0$, and magnetic, $\vec{M}_0$, fields are related through Maxwell's equations;

$$\vec{\nabla} \times \vec{E}_0 = -i\omega_0 \mu \vec{H}_0 \tag{2.3.11}$$

$$\vec{\nabla} \times \vec{H}_0 = i\omega_0 \epsilon \vec{E}_0 \tag{2.3.12}$$

where we have used μ and ϵ to be the real permeability and permittivity values of the material filling the cavity, and ω_0 to be the resonance frequency of a stable mode within the unperturbed cavity. By placing a material perturbation, having permeability $\mu + \Delta\mu$ and permittivity $\epsilon + \Delta\epsilon$, within the cavity we change the resonant field distributions near the perturbation, thus altering the resonance frequencies of any stable modes. Here we define $\Delta\mu$ and $\Delta\epsilon$ as the change in permeability and permittivity caused by the introduction of the sample to the cavity. The values of $\Delta\mu$ and $\Delta\epsilon$ are dependent on position within the cavity system; outside the material sample the local permeability and permittivity will be unchanged by the sample (for small samples) and $\Delta\mu$ and $\Delta\epsilon$ will equal zero, while at locations within the material perturbation $\Delta\mu$ and $\Delta\epsilon$ may be quite large. The new relation between the EM field dispersions within the perturbed cavity, $\vec{E}$ and $\vec{H}$, can still be defined using Maxwell's equations similar to before;

$$\vec{\nabla} \times \vec{E} = -i\omega(\mu + \Delta\mu)\vec{H} \tag{2.3.13}$$

$$\vec{\nabla} \times \vec{H} = -i\omega(\epsilon + \Delta\epsilon)\vec{E} \tag{2.3.14}$$

with ω representing the new, perturbed, resonance frequency of the stable mode in Eqs. 2.3.11 and 2.3.12.

By combining Eqs. 2.3.11 and 2.3.12 with Eqs. 2.3.13 and 2.3.14 we can construct an expression for the magnitude of the frequency shift experienced by the cavity resonance mode upon the introduction of the material perturbation. This can be done by multiplying the complex conjugate of Eq. 2.3.11 with $\vec{H}$, the complex cojugate of Eq. 2.3.12 with $\vec{E}$, Eq. 2.3.13 with $\vec{H}_0^*$ (the complex conjugate of $\vec{H}_0$), and Eq. 2.3.14 with $\vec{E}_0^*$ (the complex conjugate of $\vec{E}_0$); creating a coupled system containing both the perturbed and unperturbed EM field distributions. Rearranging these equations and integrating over the volume of the cavity then allows us to write[117];

$$\frac{\omega - \omega_0}{\omega} = -\frac{\int_{V_0}(\Delta\epsilon\vec{E}\cdot\vec{E}_0^* + \Delta\mu\vec{H}\cdot\vec{H}_0^*)dv}{\int_{V_0}(\epsilon\vec{E}\cdot\vec{E}_0^* + \mu\vec{H}\cdot\vec{H}_0^*)dv} \tag{2.3.15}$$

As we have not yet made any assumptions of our system in our derivation this equation represents an exact expression for how the resonant frequency of a cavity would change upon the insertion of a material perturbation, valid for perturbations of any shape, size, or position within the cavity. However, solving Eq. 2.3.15 is generally very difficult because, although the unperturbed EM field distributions $\vec{E}_0$ and $\vec{H}_0$ can be easily determined for most well designed cavities, the perturbed fields $\vec{E}$ and $\vec{H}$ are generally unknown. This equation can be greatly simplified though if we now employ the main assumption of cavity perturbation theory; that for small material perturbations the perturbed EM field distribution within the cavity will be essentially unchanged from the unperturbed distribution. This allows us to approximate $\vec{E} \approx \vec{E}_0$ and $\vec{H} \approx \vec{H}_0$. As we expect only a small change to the resonant frequency of the system for small perturbations, we can also assume $\frac{\omega - \omega_0}{\omega} \approx \frac{\omega - \omega_0}{\omega_0}$ on the left-hand side of Eq. 2.3.15, further simplifying calculations as ω will generally be an unknown parameter. Based on these assumptions, the fractional change in the resonant frequency of the perturbed cavity system can now be written as;

$$\frac{\omega - \omega_0}{\omega_0} \simeq -\frac{\int_{V_0}(\Delta\epsilon|\vec{E}_0|^2 + \Delta\mu|\vec{H}_0|^2)dv}{\int_{V_0}(\epsilon|\vec{E}_0|^2 + \mu|\vec{H}_0|^2)dv} \tag{2.3.16}$$

In the above perturbation equation, we see that the addition of a material perturbation with a positive $\Delta\epsilon$ or $\Delta\mu$ will tend to decrease the resonant frequency of modes within the cavity. By comparing the resonant frequencies of the cavity before and after the perturbation is inserted, the permittivity and permeability of the perturbation can be calculated as $\epsilon_{perturbation} = \epsilon + \Delta\epsilon$ and $\mu_{perturbation} = \mu + \Delta\mu$. An example of this frequency perturbation is shown in Fig. 2.5(c), where the addition of a glass rod ($\epsilon = 4.76 \times \epsilon_0 = 4.21 \times 10^{-11}$ F/m) to a rectangular air filled cavity causes the frequency of a resonant mode within

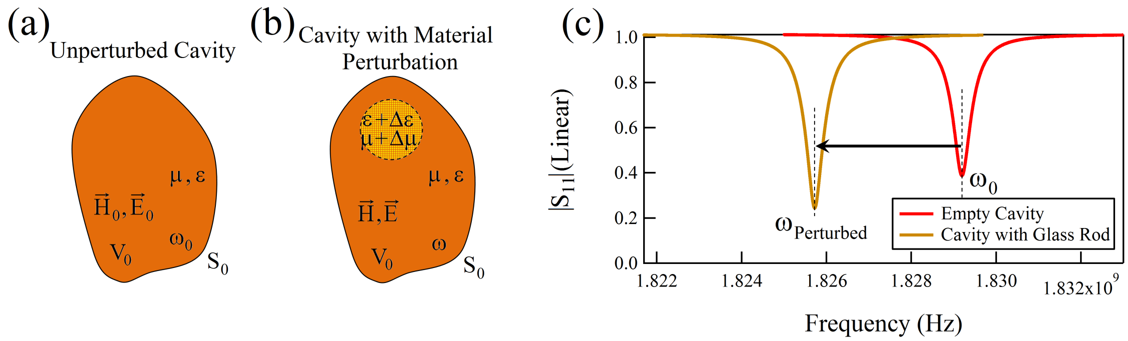

Figure 2.5: **(a)** A diagram of a general resonant cavity system, of volume V_0, filled with a material of permeability μ and permittivity ϵ. At the resonant frequency of this system, ω_0, the magnetic and electric fields within the cavity will have the spatially dependent distributions $\vec{H}_0$ and $\vec{E}_0$. **(b)** Upon the introduction of a material perturbation having permeability $\mu+\Delta\mu$ and permittivity $\epsilon+\Delta\epsilon$, the resonant field distributions within the cavity will be shifted to $\vec{H}$ and $\vec{E}$, and the resonant frequency of the excited cavity mode will be shifted to ω. **(c)** In this rectangular waveguide cavity we see that the introduction of a thin glass rod into the cavity shifts the measured resonant frequency to a lower value. In this system $|S_{11}|$ represents microwave reflection from the cavity system, decreasing when microwaves are absorbed during resonance.

the cavity to decrease. It can be seen in Eq. 2.3.16 that because $\Delta\epsilon$ and $\Delta\mu$ will only have non-zero values at the location of the material perturbation, the magnitude of the $\omega - \omega_0$ frequency shift will vary depending on the size and location of the perturbation. This variation allows the values of either $\Delta\epsilon$ or $\Delta\mu$ to be measured individually by placing the perturbation at locations where either $\vec{E}_0$ or $\vec{H}_0$ equal zero. This specific placement is not always necessary, as for many magnetic materials $\Delta\mu \gg \Delta\epsilon$ and for many dielectric materials $\Delta\epsilon \gg \Delta\mu$[114], meaning that in these materials the right-hand numerator of Eq. 2.3.16 will be dominated by either an $\vec{E}_0$ or $\vec{H}_0$ dependent term.

Looking closely at Eq. 2.3.16, we also see that the magnetic and electric field integrals can be related to the stored magnetic, U_{mag}, and electric, U_{elec}, energies of the original and perturbed cavity systems. This allows us to interpret the frequency shift due to the perturbation in relation to these energies[118];

$$\frac{\omega - \omega_0}{\omega_0} = -\frac{\Delta U_{elec} + \Delta U_{mag}}{U_{elec} + U_{mag}} = \frac{\Delta U_{total}}{U_{total}} \tag{2.3.17}$$

with U_{total} representing the total electromagnetic energy stored in the unperturbed cavity. Thus we see that cavity perturbation theory describes the fractional change in the resonance frequency of a cavity mode caused by a material perturbation to be directly correlated to the change in EM energy stored within the cavity.

The observed frequency shifts of cavity resonance modes due to the inclusion of material perturbations are closely tied to the frequency shifts within cavity magnon-polariton (CMP) systems during coupling. In the latter case, large permeability changes are induced in ferromagnetic samples as they are excited to FMR during coupling to a cavity mode[12]. However, within CMP systems the resonant FM sample couples itself to the cavity system by producing EM fields during its resonant motion. In a strongly coupled system these FM produced fields may have significant effects on the field distribution within the cavity system, even for relatively small FM samples[123]. Thus, although Eq. 2.3.15 would still be correct within coupled CMP systems, the assumption of unchanged EM field distributions used to derive Eq. 2.3.16 would no longer hold. For this reason the perturbation equations derived here have greatly reduced accuracy in measuring the properties of resonant materials, despite the fact that measurements performed on coupled CMP systems are extremely similar to perturbative measurements on non-resonant samples[57][25]. However, within these CMP systems we are still able to determine the dynamic properties of the FM sample (which are closely related to its permeability), through frequency changes in the coupled cavity-magnon modes, using coupled oscillator and Hamiltonian models[56][124].

2.3.3 RLC Oscillator Description

Although physically very different, cavity oscillators and RLC circuits prove to have extremely similar electrical properties[114]. Indeed in many electrical applications, such as signal filters and amplifiers, these two different oscillating electromagnetic systems are used in nearly identical roles, with cavities being generally used where high Q factors are required and RLC circuits being preferred for smaller size and lower cost applications[115][125]. Because of their similar resonant properties, it is common to see cavity oscillators described in terms of an equivalent RLC circuit. In this description the damping of the cavity is analogous to resistance in the circuit, while the $\vec{E}$ and $\vec{H}$ field distributions in the cavity can be related to the fields produced by a capacitor and inductor in an RLC circuit[124][126]. This RLC circuit description of cavity oscillators also proves useful for differentiating between impedance-matched cavity resonators, whose non-resonant impedance matches that of the cables carrying electrical signals to it, and non-impedance-matched cavities[114]. In impedance-matched cavities the S_{21} transmission (ratio of energy transmitted through system relative to the input energy) is generally very high away from resonance, but decreases near the cavity resonance frequency as the impedance of the cavity is changed by the presence of stable resonance modes; these cavities thus display resonant modes as a sharp drop in S_{21} transmission and can be described by a parallel RLC circuit. In non-impedance-matched cavities S_{21} transmission is low far from resonance but the presence of resonant modes in the cavity changes the impedance to match the input cables, resulting in an increased S_{21} transmission; these cavities display resonant modes as S_{21} transmission peaks and are thus described by a series RLC circuit.

Series RLC Circuit

For an RLC circuit with a resistive component R, an inductive component L, and a capacitive component C, similar to the one shown in Fig. 2.6, the basic expression for the impedance in response to an AC input signal is given by[114];

$$Z_{in} = R + i\omega L - i\frac{1}{\omega C} \tag{2.3.18}$$

with ω being the frequency of the input signal. This expression is clearly frequency dependent, with AC current effects inducing resonant interactions between the inductive and capacitive components of the circuit. The expression for the power delivered into the RLC circuit from an AC input can be derived from Eq. 2.3.18 using the complex expression of Joule's Law for resistive heating[118];

$$P_{in} = \frac{1}{2}|I|^2 Z_{in} = \frac{1}{2}|I|^2 \left(R + i\omega L - i\frac{1}{\omega C}\right) \tag{2.3.19}$$

with I being the magnitude of the AC current input into the circuit. We can see from this expression that the real component represents the power dissipated by resistive elements of the system, P_{loss}, similar to damping effects in cavities;

$$P_{loss} = \frac{1}{2}|I|^2 R \tag{2.3.20}$$

while the imaginary components of Eq. 2.3.19 represent energy stored within the circuit system, as either magnetic energies U_m stored as fields within the inductive component or as electric potential energies U_e stored in the capacitive component. As during resonant behaviour these electric and magnetic energies will be continuously traded between the components as the inductor and capacitor continually charge and discharge, the average U_m and U_e values over several oscillation cycles will be equal to half their maximum

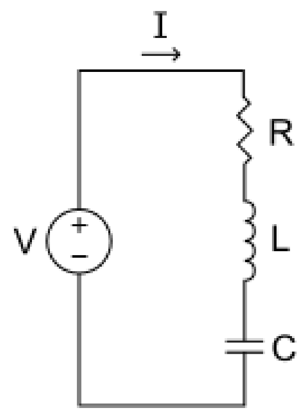

Figure 2.6: A diagram of the layout of a basic series RLC circuit, consisting of a resistor, R, an inductor, L, and a capacitor, C. The circuit is excited by an alternating current of voltage V, frequency ω, and amplitude I.

values as given in Eq. 2.3.19;

$$U_m = \frac{1}{4}|I|^2 L \tag{2.3.21}$$

$$U_e = \frac{1}{4}|I|^2 \frac{1}{\omega^2 C} \tag{2.3.22}$$

The above equations allow us to rewrite Eq. 2.3.18 in terms of the energies stored and dissipated by the elements of the RLC circuit, giving;

$$Z_{in} = \frac{2P_{in}}{|I|^2} = \frac{2P_{loss} + 2i\omega(U_m - U_e)}{|I|^2} \tag{2.3.23}$$

The resonant condition for a series RLC circuit occurs when the impedance is minimized and expressed in entirely real terms. In this state the energies stored in the inductive and capacitive components of the circuit are maximized[114]. We can see from Eq. 2.3.23 that resonance will thus occur when $U_m = U_e$, thus we can define the resonance frequency of the circuit, ω_0, by applying this condition to Eqs. 2.3.21 and 2.3.22;

$$\omega_0 = \frac{1}{\sqrt{LC}} \tag{2.3.24}$$

We can define the quality factor, Q, of our RLC circuit as the ratio of total EM energy stored in the circuit relative to the power lost per oscillation cycle. This is the same definition as we used in Eq. 2.3.8 for our cavity resonator. At the resonant condition of $U_m = U_e$ we find;

$$Q = \omega_0 \frac{U_m + U_e}{P_{loss}} = \omega_0 \frac{2U_e}{P_{loss}} = \frac{1}{\omega_0 RC} \tag{2.3.25}$$

Using the expression in Eq. 2.3.24, we can now express the impedance of our series RLC circuit defined in Eq. 2.3.18 in terms of its resonant frequency;

$$Z_{in} = R + i\omega L \left(\frac{\omega^2 - \omega_0^2}{\omega^2} \right) \tag{2.3.26}$$

For input frequencies near resonance, such that $\omega_0/\omega \approx 1$, we can further express Eq. 2.3.26 in terms of the RLC circuit's Q factor given in Eq. 2.3.25;

$$Z_{in} \simeq i2L \left(\omega - \omega_0 - i\frac{\omega_0}{2Q} \right) \tag{2.3.27}$$

Parallel RLC Circuit

In a parallel configuration, such as that shown in Fig. 2.7, the resonant properties of an RLC circuit are very similar to the series configuration discussed previously. Using the same resistive R, inductive L, and capacitive C components, the input impedance of a parallel RLC circuit in response to an AC input signal is given by[114];

$$Z_{in} = \left(\frac{1}{R} + \frac{1}{i\omega L} + i\omega C \right)^{-1} \tag{2.3.28}$$

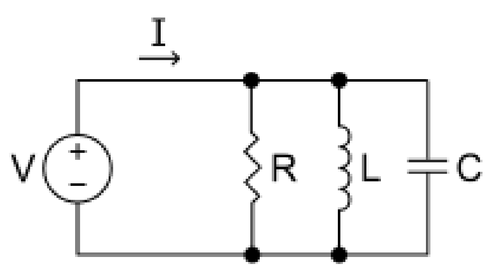

Figure 2.7: A diagram of the layout of a basic parallel RLC circuit, consisting of a resistor, R, an inductor, L, and a capacitor, C, connected in parallel. The circuit is excited by an alternating current of voltage V, frequency ω, and amplitude I.

Similar to the process we used for a series RLC circuit in Eqs. 2.3.19 and 2.3.20, we can use the complex expression of Joule's Law for resistive heating to calculate the complex expressions for the power delivered to the parallel RLC system, P_{in}, and the power dissipated, P_{loss};

$$P_{in} = \frac{1}{2}|V|^2 \left(\frac{1}{Z^*_{in}}\right) = \frac{1}{2}|V|^2 \left(\frac{1}{R} + \frac{i}{\omega L} - i\omega C\right) \tag{2.3.29}$$

$$P_{loss} = \frac{1}{2}\frac{|V|^2}{R} \tag{2.3.30}$$

where V represents the voltage of the input signal. As the electric and magnetic energies stored in the capacitive and inductive elements of the parallel RLC system will be equal to those in Eqs. 2.3.21 and 2.3.22, we are able to describe the impedance of the parallel circuit as;

$$Z_{in} = \frac{|I|^2}{2P_{in}} = \frac{|I|^2}{P_{loss} + 2i\omega(U_m - U_e)} \tag{2.3.31}$$

which is seen to be the inverse of Eq. 2.3.23 for the series RLC circuit. The resonant condition for parallel RLC circuits will thus occur when the impedance of the circuit is maximized, and will again occur when $U_m = U_e$. We thus find that the resonant frequency of a parallel RLC circuit, ω_0, is identical to that of a series RLC circuit containing the same RLC components[114];

$$\omega_0 = \frac{1}{\sqrt{LC}} \tag{2.3.32}$$

Similarly, the Q factor of a parallel circuit can be defined in the same fashion as the series case in Eq. 2.3.25, giving an inverse result;

$$Q = \omega_0 \frac{2U_m}{P_{loss}} = \omega_0 RC \tag{2.3.33}$$

For input frequencies near resonance, we can use the expressions for ω_0 and Q in parallel RLC circuits given by Eqs. 2.3.32 and 2.3.33 to rewrite the impedance given by Eq. 2.3.28 as;

$$Z_{in} = \frac{1}{i2C\left(\omega - \omega_0 - i\dfrac{\omega_0}{2Q}\right)} \tag{2.3.34}$$

which we can see is nearly the exact inverse expression to that of Eq. 2.3.27 for the series RLC circuit.

2.3.4 Calculating S_{21} Transmission for RLC Circuits and Cavity Resonators

The impedance expressions for RLC circuits can be used to express the resonant properties of cavity resonators, with the S_{21} transmission properties of series RLC circuits corresponding with those of impedance-matched cavities, and the S_{21} transmissions of parallel RLC circuits corresponding with those of non-impedance-matched cavities[114]. For a given mnp cavity mode the inductive L_{mnp} and capacitive C_{mnp} properties of a cavity can be calculated as[127];

$$L_{mnp} = \mu V k_{mnp}^2 \tag{2.3.35}$$

$$C_{mnp} = \frac{\epsilon}{V k_{mnp}^4} \tag{2.3.36}$$

with μ and ϵ representing the permeability and permittivity of the material filling the cavity and V defined as the volume of the cavity. The term k_{mnp} is the mode wavenumber of the cavity and is dependent on the shape and structure of the cavity; for a rectangular cavity with dimensions a, b, and d this mode wavenumber can be expressed as;

$$k_{mnp} = \sqrt{\left(\frac{m\pi}{a}\right)^2 + \left(\frac{n\pi}{b}\right)^2 + \left(\frac{p\pi}{d}\right)^2} \tag{2.3.37}$$

While for a cylindrical cavity of radius R and length L the mode number is expressed as;

$$k_{mnp} = \sqrt{\left(\frac{X_{mn}}{R}\right)^2 + \left(\frac{p\pi}{L}\right)^2} \tag{2.3.38}$$

with X_{mn} describing the nth zero of the mth Bessel function for TE modes and the nth zero of the *derivative* of the mth Bessel function for TM modes. From the above expressions, we see that the resonance frequency of a microwave cavity, ω_c, can be expressed in RLC circuit terms as;

$$\omega_c = \frac{1}{\sqrt{LC}} = \frac{1}{\sqrt{\mu\epsilon}} k_{mnp} \tag{2.3.39}$$

which agrees with the expressions for cavity resonance frequencies derived from Maxwell's Equations given in Eqs. 2.3.5, 2.3.6, and 2.3.7. The damping forces within a resonant cavity, β, can also be expressed in terms of the cavity's RLC circuit equivalent, for impedance-matched and non-impedance matched cavities this relation is written as;

$$\beta = \frac{R}{2}\sqrt{\frac{C}{L}} \qquad \text{for Series RLC Circuits} \tag{2.3.40}$$

$$\beta = \frac{1}{2R}\sqrt{\frac{L}{C}} \qquad \text{for Parallel RLC Circuits} \tag{2.3.41}$$

Using the above relations, the impedance of Series RLC circuits (corresponding to impedance-matched cavities) and Parallel RLC circuits (corresponding to non-impedance-matched cavities) can thus be given by[25][114];

$$Z_c = i2L(\omega - \omega_c - i\omega_c\beta) \qquad \text{for Series RLC Circuits} \tag{2.3.42}$$

$$Z_c = \frac{1}{i2C(\omega - \omega_c - i\omega_c\beta)} \qquad \text{for Parallel RLC Circuits} \tag{2.3.43}$$

The S_{21} transmission properties of these two types of RLC circuit systems can be calculated from their impedance properties using scattering theory[114], where the transmission and reflection properties of the circuit are determined from the input and output signals at the ports leading into the system. The total transmission of the system when attached to input/output cables will be affected by the impedance of these cables, Z_0. For the case where Z_0 is equal to the non-resonant impedance of an RLC circuit, the equation for S_{21} transmission is given by;

$$S_{21} = \frac{2Z_0}{2Z_0 + Z_c} \tag{2.3.44}$$

Inserting the calculated impedances of series and parallel RLC circuits from Eqs. 2.3.42 and 2.3.43, we find the following S_{21} transmission dispersions, which have been plotted in Fig. 2.8;

$$S_{21} = \frac{Z_0/L}{i(\omega - \omega_c) + \omega_c\beta + Z_0/L} \qquad \text{for Series RLC Circuits} \tag{2.3.45}$$

$$S_{21} = 1 - \frac{1/4Z_0C}{i(\omega - \omega_0) + \omega_c\beta + 1/4Z_0C} \qquad \text{for Parallel RLC Circuits} \tag{2.3.46}$$

As can be seen in the above equations, the effect of the input/output impedances will be to add an additional damping factor to the measured S_{21} transmission spectra and limit the magnitude of the resonant peak. This factor is typically termed extrinsic damping, as it is external to the dynamics of the RLC oscillator. As this intrinsic damping occurs at the RLC/cable interfaces due to impedance mismatch, it can be limited by closely matching the cable impedance to the non-resonant impedance of a resonant system.

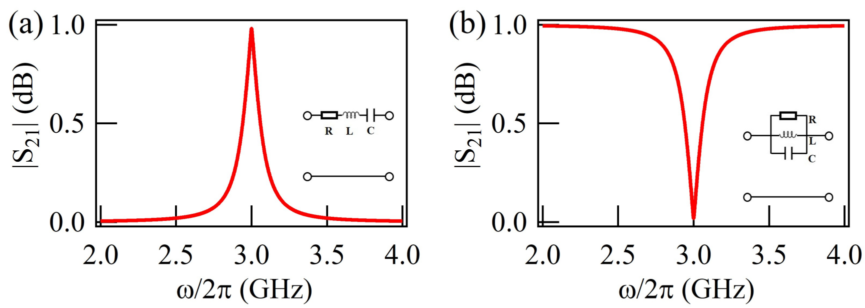

Figure 2.8: Modelled transmission plots representing the S_{21} of **(a)** series and **(b)** parallel RLC circuits. The RLC parameters used to calculate these plots are equivalent for the two circuit configurations.

2.4 Magnon-Photon Coupling

2.4.1 Polaritons

In the previous sections we have discussed some of the possible effects an applied EM field can impart on a material, however the opposite can also occur. Similar to how changing currents and moving magnetic systems can generate EM fields, the changing electromagnetic properties of a material under the influence of an external EM field can generate an EM field of their own[117]. In specially designed systems this material-generated EM field is able to influence the externally applied EM field sufficiently enough to change how it interacts with the material. In these systems a form of feedback loop is created and it is no longer possible to consider either element of the system, the external EM field or the material dynamics, alone without considering the influence of the other element. This process of coupling between the two systems leads to the generation of quasi-particles known as polaritons, which are combinations of EM and material excitations that behave as a single excited state[128].

Mathematically, the production of polaritons in a coupled system is a result of the interplay between photon excitations and Maxwell's equations within a material[129]. According to Maxwell's equations the dispersion of EM fields through a material will be governed by[117];

$$\omega = k/\sqrt{\epsilon(\omega, k)\mu(\omega, k)} \tag{2.4.1}$$

where k is the propagation wavevector of the fields through the material, $\epsilon(\omega, k)$ is the material permittivity, and $\mu(\omega, k)$ is the material permeability[117]. The parameters $\epsilon(\omega, k)$ and $\mu(\omega, k)$ thus determine a material's response to an applied EM field or photon excitation, and are themselves dependent on the lattice, spin, and charge dynamics within the material. Under certain conditions the applied field can generate excitations within the material, such as phonons[129][130], magnons[131], excitons[132], or plasmons[133][134], which exist as dynamic resonance structures formed by a material's lattice, spin, or charge states. While these material excitations are present the $\epsilon(\omega, k)$ and $\mu(\omega, k)$ parameters of the material may be significantly shifted from their original values, significantly altering the propagation of EM waves through the material. As there exist several different possible excitation states within materials, polaritons are typically differentiated based on the specific material and photon excitations which are coupled; for example phonon-polaritons[129][130], magnon-polaritons[117], plasma-polaritons[133][134], and cavity-exciton-polaritons[135][136][137].

The most visible consequence of polariton generation during the interaction between EM photons and a material is a dramatic shift in the $\omega - k$ dispersion of the EM waves near the excitation frequency of the material[130][138]. Following Eq. 2.4.1, as the material properties ϵ and/or μ diverge to $\pm\infty$ values when excitation states are generated, the k propagation vector near these excitation frequencies will similarly diverge to $\pm\infty$. This produces an $\omega - k$ dispersion anti-crossing in coupled polariton systems (similar to that shown in Fig. 2.9), in contrast to the steadily increasing, single-valued, $\omega - k$ dispersions expected in materials where EM photons cannot generate material excitations[139]. The dynamics of coupling between the EM photon and material excitations will further impact the $\omega - k$ dispersion, as the energy (ω at resonance) of the polaritons produced during coupling will be affected if the behaviour of the material excitations is changed, even if k is otherwise unchanged[128][130][137]. The energies of polaritons produced by photons coupling to a material excitation at resonance (photons absorbed by material) are found to be different than those produced by coupling at antiresonance (photons pass through material). As no coupled

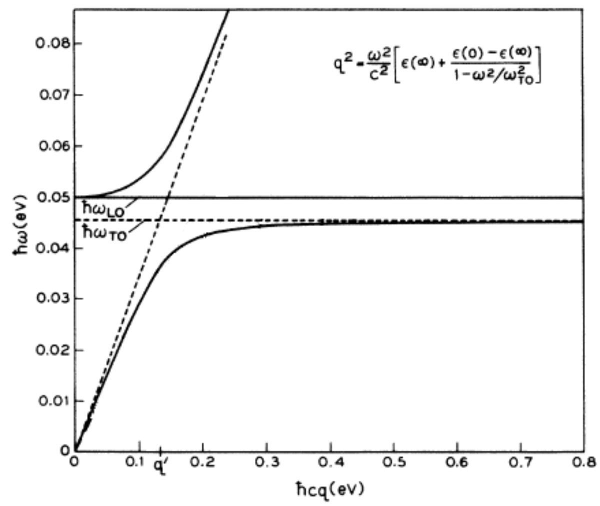

Figure 2.9: A plot of the modelled frequency-wavevector dispersion curves (solid lines) for phonon-polariton coupling in gallium phosphide, modified from Ref. [138], where dashed lines indicate the uncoupled photon and phonon dispersions. In this system changes to the wavevector inside the material, labelled as q here in the x-axis, are influenced by material permittivity changes (described by the upper right-hand equation) near coupling frequencies. This has the effect of producing a mode anticrossing in the dispersion and modifying the frequency of the transverse optical (TO) phonon mode within the material. As the longitudinal optical (LO) phonon is an antiresonance mode, it does not hybridize with light and does not experience the same frequency shift as the TO mode. Thus a polariton gap, where no coupled phonon-polariton modes can exist, appears between the TO and LO phonon modes.

polariton modes are stable between these resonant and antiresonant states (due to the negative permittivity/permeability values)[140], a frequency band in the $\omega - k$ polariton dispersion is produced where no EM waves are able to propagate through the material[139]. This band is shown in Fig. 2.9 for a phonon-polariton system as the gap between photons coupled to the transverse optical (TO) phonon mode of a material and those coupled to the longitudinal optical (LO) phonon mode[138]. The presence of this polariton gap in $\omega - k$ dispersions is a clear sign that polariton coupling is occurring in a system, as it indicates that the resonant properties of both the photon and material excitations are being influenced by each other.

2.4.2 Modelling Magnon-Photon Coupling

The physical background of the coupling between photon and magnon resonance modes can be described as an interplay between Faraday's Law, where the varying magnetization of the magnon system during resonance generates an electric field, and Ampère's Law, where the varying electrical currents produced by EM photons generate magnetic fields[117]. Within a coupled system the magnetic fields produced by the resonant photons act to drive resonant motion in the magnon system, while the electrical fields produced by the magnon system influence the EM dispersion of the resonant photons. Through the effects of these laws, the combined magnon-photon system is described as 'coupled' as the behaviour of the magnon and photon subsystems can no longer be described independently of each other. Although the electromagnetic forces governing this coupling are well understood, mathematically describing coupled magnon-photon systems is complicated by the fact the physical systems involved can contain on the order of $\sim 10^{23}$ interacting particles[141]. Clearly it is unnecessarily complicated, not to mention impossible, to individually describe each quantum interaction within these systems. Thus a simpler model is required to study and understand these systems, one which is able to reduce the numerous EM interactions to a simpler form while maintaining the important dynamic information from the systems.

Jaynes-Cummings Model

For studies focusing on exploring the quantum nature of coupled magnon-photon systems, it is generally desirable to base any model on quantum optics and quantum electrodynamics. In this formulation the canonical Hamiltonian used is one originally designed to describe spontaneous photon emission from polarized spin systems, called the Jaynes-Cummings model[142][143]. For a large collection of spins coupled to a resonant photon system we are able to treat the resonant spin excitations (magnons) as bosons[144][145]. Restricting ourselves to only a single photon resonance mode of frequency ω_c and the lowest energy spin mode (the Kittel FMR mode of frequency ω_r), the Hamiltonian describing the interactions between magnons and photons in a coupled system can be written as (setting $\hbar = 1$)[146];

$$H_{jc} = \omega_c a^\dagger a + \omega_r b^\dagger b + g(a^\dagger b + ab^\dagger) + \Omega_d(a^\dagger e^{-i\omega t} + ae^{i\omega t}) \tag{2.4.2}$$

Here g describes the coupling forces between the magnon and photon systems, while $a^\dagger$ (a) and $b^\dagger$ (b) are the creation (annihilation) operators for the photon and magnon excitations, respectively. The final term in this Hamiltonian describes the oscillatory driving force acting on the photon system over a time t, with magnitude Ω_d and at frequency ω. This driving force is assumed to only interact with the photon system, driving it to resonance, while the magnon system only experiences its effects through its coupling to the photon system. This coupling between the magnon and photon systems is described by the third term on the right hand side of the Hamiltonian, with g describing the strength of the coupling forces between the two systems. To make further calculations simpler, we begin by converting this Jaynes-Cummings Hamiltonian to a rotating reference frame, with respect to the driving frequency ω, using the unitary transformation $R = e^{(-i\omega a^\dagger a t - i\omega b^\dagger b t)}$. This gives;

$$
\begin{aligned}
H &= R^\dagger H_{jc} R - i R^\dagger \frac{\partial R}{\partial t} \\
&= (\omega - \omega_c) a^\dagger a + (\omega - \omega_r) b^\dagger b + g(a^\dagger b + a b^\dagger) + \Omega_d (a^\dagger + a)
\end{aligned}
\tag{2.4.3}
$$

The energy dissipation from this system is defined as[57];

$$
Q = \frac{da^\dagger}{dt}\frac{da}{dt}\beta + \frac{db^\dagger}{dt}\frac{db}{dt}\alpha \tag{2.4.4}
$$

with β representing damping in the photon system and α representing the damping of the magnon excitations. Here we assume that the magnon damping is linear to its excitation amplitude, which is valid for low amplitude excitations[77]. As magnon excitation amplitude increases higher order non-linear magnon damping terms will tend to become more significant; this non-linear damping and the dynamic effects it leads to are further explored in subsequent chapters. With our Hamiltonian, H, and dissipation function, Q, we are able to obtain the quantum Langevin equations for the coupled system through[147];

$$
i\frac{da}{dt} = \frac{\partial H}{\partial a^\dagger} + \frac{\partial Q}{\partial \left(\frac{da^\dagger}{dt}\right)} \tag{2.4.5}
$$

$$
i\frac{db}{dt} = \frac{\partial H}{\partial b^\dagger} + \frac{\partial Q}{\partial \left(\frac{db^\dagger}{dt}\right)} \tag{2.4.6}
$$

This gives us the following equations of motion for our system;

$$
i\frac{da}{dt} = (\omega_c - \omega)a + gb + \Omega_d + \frac{da}{dt}\beta \tag{2.4.7}
$$

$$
i\frac{db}{dt} = (\omega_r - \omega)b + ga + \frac{db}{dt}\alpha \tag{2.4.8}
$$

If the effects of coupling are small relative to the excitation energies of both the photon and magnon subsystems ($g \ll \omega_c, \omega_r$), then to first order we can take the dynamic motions of a and b to be essentially unchanged from the non-interacting case, where $H_0 = \omega_c a^\dagger a + \omega_r b^\dagger b$. From this approximation we determine;

$$a = Ae^{-i\omega_c t} \tag{2.4.9}$$

$$b = Be^{-i\omega_r t} \tag{2.4.10}$$

where we find that the photon and magnon excitations will have large static components (A for the photon system and B for the magnon system) combined with a smaller oscillating component. Assuming that the dynamics of the cavity and magnon resonances will be dominated by the large static amplitude terms, we can write Eqs. 2.4.7 and 2.4.8 as;

$$i\frac{dA}{dt} = (\omega_c - \omega)A + gB + \Omega_d - i\omega_c\beta A \tag{2.4.11}$$

$$i\frac{dB}{dt} = (\omega_r - \omega)B + gA - i\omega_r\alpha B \tag{2.4.12}$$

For the case where the energy lost to damping effects is balanced by the energy provided to the system by Ω_d, our coupled system will be in an equilibrium state. During equilibrium the resonant amplitudes of the photon and magnon subsystems will remain constant, meaning we can set $dA/dt = dB/dt = 0$, and allowing us to write the equations of motion for our coupled magnon-photon system in the following matrix form;

$$\begin{pmatrix} \omega_c - \omega - i\omega_c\beta & g \\ g & \omega_r - \omega - i\omega_r\alpha \end{pmatrix} \begin{pmatrix} A \\ B \end{pmatrix} = \begin{pmatrix} -\Omega_d \\ 0 \end{pmatrix} \tag{2.4.13}$$

This matrix allows the coupled dynamics of the cavity and magnon systems to be determined based on their response to an input signal. The term on the right-hand side of the equation describes the input forces on the magnon and photon systems, here the only driving force is Ω_d which drives the photon system at a frequency ω. On the left-hand side of the equation we see that the amplitudes of each subsystem during coupled resonance (A and B) are determined by a 2x2 coupling matrix based on the intrinsic and coupled properties of the two systems. By calculating the frequencies where the determinant of this coupling matrix equals zero, the eigenfrequencies denoting resonant modes of the coupled system can be found. For each eigenfrequency a respective eigenvector can also be calculated, which allows us to determine the relative phase between the motions of the magnon and photon systems during resonance. In general, if the magnon and photon subsystems are arranged such that their uncoupled resonance frequencies are equal ($\omega_c = \omega_r$) then two resonant frequencies will be possible for the system; in-phase motion with an eigenvector of (1,1), and out-of-phase motion with an eigenvector of (1,-1)[148]. The relative eigenfrequencies of these modes will depend on the nature of the coupling forces between the two systems, with one resonant mode having a resonance frequency higher than that of the uncoupled systems and the other mode having a resonance at a lower frequency.

Harmonic Oscillator Model

Although the quantum Jaynes-Cummings Model allows us to understand the coupled behaviour of a CMP system from a quantum background, in many cases this behaviour can also be modelled using classical methods. In these models the precise electromagnetic origins of the resonant photon and magnon systems can be replaced by assuming that each system acts as a classical mechanical oscillator[149]. The coupling forces g between the two systems can then be modelled as a spring connecting them, resulting in the following well-known equations of motion for a system of coupled oscillators;

$$F(t) = \frac{d^2a}{dt^2} + \omega_c^2 a + 2\beta\omega_c \frac{da}{dt} - 2g\omega b \tag{2.4.14}$$

$$0 = \frac{d^2b}{dt^2} + \omega_r^2 b + 2\alpha\omega_r \frac{db}{dt} - 2g\omega a \tag{2.4.15}$$

Here we describe our photon and magnon systems as 1-dimensional oscillators with respective positions of a and b relative to their unexcited background positions. The uncoupled resonant frequencies of these oscillators are given by ω_c and ω_r for the oscillators respectively representing the photon and magnon systems. The terms on the left-hand side of these equations describe the driving forces on each oscillator; corresponding to our CMP system we only drive the oscillator corresponding to the cavity system. The driving and coupling forces in the system will then accelerate both oscillators (the first terms on the right-hand side). The value of these accelerations will be further determined by the energy of the system during its resonant state (the second terms on the right-hand side), which will be generally dependent on the resonant motion of the oscillators, and damping forces proportional to the velocity of motion in each oscillator (the third terms on the right-hand side). The final terms on the right-hand side of Eqs. 2.4.14 and 2.4.15 determine the strength of the coupling force each oscillator exerts on the other, which is relative to g, the strength of the coupling between the oscillators, and the position of each oscillator relative to its resting position. If the driving force $F(t)$ is periodic of the form $F(t) = fe^{-i\omega t}$ then we can assume that the motions of the two oscillators will also be dominated by periodic terms, such that $a = Ae^{-i\omega t}$ and $b = Be^{-i\omega t}$ where A and B represent the amplitudes of the oscillators' periodic motion. Inserting this into Eqs. 2.4.14 and 2.4.15 allows us to rewrite the equations in matrix form as;

$$\begin{pmatrix} \omega^2 - \omega_c^2 + i2\beta\omega\omega_c & 2g\omega \\ 2g\omega & \omega^2 - \omega_r^2 + i2\alpha\omega\omega_r \end{pmatrix} \begin{pmatrix} A \\ B \end{pmatrix} = \begin{pmatrix} -f \\ 0 \end{pmatrix} \tag{2.4.16}$$

Although the formulation of our coupled CMP system is not exactly the same in this harmonic oscillator model as it is in the quantum model of Eq. 2.4.13, it can be found to be equivalent for input frequencies near coupling where $\omega_c, \omega_r \approx \omega$. In the next section we will see that after calculating the S_{21} energy transmission through our CMP system using both the quantum and harmonic oscillator models results in functionally identical expressions.

2.4.3 Calculating S_{21} Transmission via Input-Output Theorem

Because the coupling effects between magnons and photons must of necessity take place in confinement, we cannot directly observe the dynamics they produce on the coupled systems. Thus, to observe coupling dynamics, we must measure the effects that they have on a measurable aspect of the coupled system. Fortunately within cavity resonators the transmission of electromagnetic fields through the cavity structure is directly tied to the resonant properties of the system[116]. In impedance matched cavities, whose non-resonant impedances are equal to those of the transmission lines carrying electromagnetic signals into them, there will be no signal reflection at off-resonance frequencies. Thus in these cavities the $|S_{21}|^2$ value (which determines signal transmission) will be near unity at these frequencies. However, near resonant frequencies the production of EM resonant modes will cause the impedance of the cavity to change. This impedance difference between the input transmission lines and the cavity will now reflect some portion of the input EM signal, resulting in a decreased $|S_{21}|^2$ transmission compared to the off-resonant case. This process allows the resonant modes of impedance matched cavities to be detected and analysed via $|S_{21}|^2$ dips in the measured transmission spectrum near resonance frequencies[114]. Alternatively, the opposite is true of cavity resonators whose impedance is not matched to the input transmission lines. In these cavities an input EM signal will typically experience large reflection at the input/cavity interface due to the large impedance difference at non-resonant frequencies, resulting in a $|S_{21}|^2$ value near zero. Near frequencies that correspond to resonance modes within the cavity the $|S_{21}|^2$ transmission of EM signals through the cavity will increase as the impedance of the cavity changes and the input signals begin to drive resonance within the system. Because of this, the resonant modes of non-impedance matched cavities can be detected and analysed via $|S_{21}|^2$ peaks in the measured transmission spectrum[114]. The resonant properties of these two types of cavities, impedance matched and non-impedance matched, are thus very similar to (and often described by) models of resonance in Parallel and Series RLC circuits, respectively.

The basis of the input-output theory for modelling S_{21} transmission is that all EM signals sent into a system must be either reflected from or transmitted through it. There are also included in the model terms allowing for the loss of EM energy inside the system due to damping effects and input/output losses, though these are generally small relative to the total transmitted and reflected energies[150][151]. In a coupled CMP system such as the ones studied in this report, only the cavity subsystem is connected to and measured via input and output ports, while the effects of the FM subsystem are measured only via its coupling effects

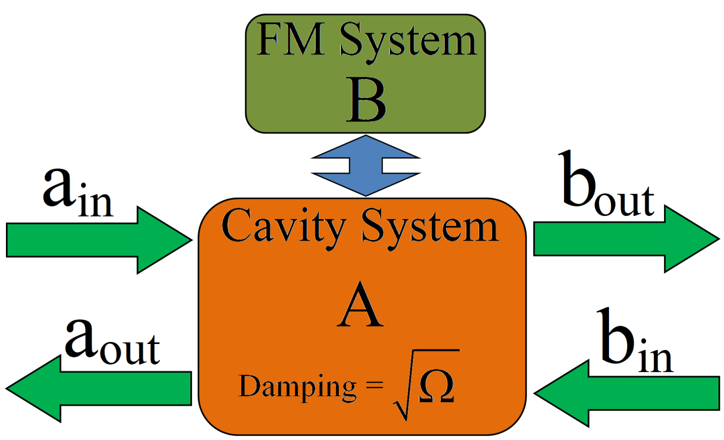

Figure 2.10: A diagram displaying the input-output model of S_{21} microwave transmission through our coupled CMP system. Here microwave signals are sent into, and detected from, the cavity resonator. The dynamics of the FM resonator can be detected through its coupling effects on the field dispersion within the cavity, which will alter the cavity's resonant properties. S_{21} is measured as b_{out}/a_{in} for $b_{in} = 0$

on the cavity system. This set-up is shown in Fig. 2.10, where the resonance amplitudes of the cavity and FM systems (A and B respectively) determine and are determined by the input and output signals at the a and b ports of the cavity. For the coupled CMP system described by this set-up, the input/output equations for an impedance matched cavity can be written as;

$$a_{in} - b_{out} = \sqrt{\Omega}A \tag{2.4.17}$$

$$b_{in} - a_{out} = \sqrt{\Omega}A \tag{2.4.18}$$

For the case of a non-impedance matched cavity, the input-output model equations take the similar form;

$$a_{in} + a_{out} = \sqrt{\Omega}A \tag{2.4.19}$$

$$b_{in} + b_{out} = \sqrt{\Omega}A \tag{2.4.20}$$

These input-output equations relate the input and output fields at each of the two ports of the cavity. The term Ω describes energy losses experienced by the fields as they travel through the system. These energy losses are dependent on the resonance amplitude of the cavity system and are generally dominated by damping losses inside the cavity, though extrinsic damping effects at the ports of the cavity also contribute to reduce Ω[114]. For our quantum model we can write $\Omega = \omega_c\beta - \Omega_{ex}$, while in our harmonic oscillator model we will have $\Omega = 2i\omega_c\omega\beta - \Omega_{ex}$, with Ω_{ex} in both cases representing energy dissipated before reaching the CMP system by extrinsic damping at the cavity ports. With the input and output fields now defined relative to the amplitude of the cavity system via these input-output equations, and the relative amplitudes of the cavity and FM systems defined by Eq. 2.4.13 (quantum model) or Eq. 2.4.16 (harmonic oscillator model) we are now able to quantify the S_{21} transmission through the system by combining terms. As $S_{21} = b_{out}/a_{in}$ for the case that $b_{in} = 0$, we thus find, using the quantum model of coupling for a impedance matched cavity;

$$S_{21} = 1 - \frac{\omega_c\beta - \Omega_{ex}}{i(\omega_c - \omega) + \omega_c\beta + \dfrac{g^2}{i(\omega_r - \omega) + \omega_r\alpha}} \tag{2.4.21}$$

Using the harmonic oscillator model of coupling for an impedance matched cavity similarly yields;

$$S_{21} = 1 - \frac{2i\omega_c\omega\beta - \Omega_{ex}}{\omega^2 - \omega_c^2 + 2i\omega_c\omega\beta + \dfrac{4g^2\omega^2}{\omega^2 - \omega_r^2 + 2i\omega_r\omega\alpha}} \tag{2.4.22}$$

Using the input-output equations for a non-impedance matched cavity as described by Eqs. 2.4.19 and 2.4.20 produces similar results, except resonance effects are in this case observed as transmission peaks. The quantum model for a non-impedance matched cavity thus gives;

$$S_{21} = \frac{\omega_c\beta - \Omega_{ex}}{i(\omega_c - \omega) + \omega_c\beta + \dfrac{g^2}{i(\omega_r - \omega) + \omega_r\alpha}} \tag{2.4.23}$$

In the harmonic oscillator model, a non-impedance matched cavity will give the transmission;

$$S_{21} = \frac{2i\omega_c\omega\beta - \Omega_{ex}}{\omega^2 - \omega_c^2 + 2i\omega_c\omega\beta + \dfrac{4g^2\omega^2}{\omega^2 - \omega_r^2 + 2i\omega_r\omega\alpha}} \tag{2.4.24}$$

We see from the above equations that although the exact form of S_{21} is slightly different for the quantum and harmonic oscillator models, both represent Lorentzian peaks modified by an addition Lorentzian term representing coupling to the FM system. In practice these two theoretical descriptions are thus equivalent.

A further theoretical model for a coupled CMP system involves describing both the cavity and FM systems in terms of their equivalent circuit elements, as was done in Sec. 2.3.3. In this RLC circuit model, the resonant properties of the FM system can be described as a system whose dynamics act to perturb the impedance of the cavity. The impedance effects of an FM system coupled to a cavity can thus be modelled with a complex impedance Z_m of[124];

$$Z_m = \frac{-i\omega_m K^2 L\omega}{\omega - \omega_r + i\alpha\omega} \tag{2.4.25}$$

Here $\omega_m = \gamma M_0$ is the saturation frequency of the FM, with γ being the gyromagnetic ratio in the material and M_0 being the saturation magnetization. The coupling between the cavity and FM systems is in this circuit model represented by K, this coupling parameter corresponds to the parameter used in the harmonic oscillator model via $K = g^2\sqrt{\omega_c/2\omega_m}$[124]. Using the RLC circuit description of a microwave cavity given by Eqs. 2.3.42 and 2.3.43 for Series and Parallel RLC circuits, the total complex impedance experienced by a EM signal through the coupled CMP system can be calculated as $Z = Z_c - Z_m$ for impedance matched cavities and $1/Z = 1/Z_c - 1/Z_m$ for non-impedance-matched cavities[114], giving;

$$Z = \frac{iL}{\omega}(\omega^2 - \omega_c^2 + 2i\beta\omega_c\omega) - \frac{i\omega_m K^2 L\omega}{\omega - \omega_r + i\alpha\omega} \quad \text{for impedance-matched cavities} \tag{2.4.26}$$

$$Z = \frac{\omega}{iC(\omega^2 - \omega_c^2 + 2i\beta\omega\omega_c) - \dfrac{i\omega_m K^2 L\omega}{\omega - \omega_r + i\alpha\omega}} \quad \text{for non-impedance-matched cavities} \tag{2.4.27}$$

Knowing the total impedance of the coupled system we can then calculate the S_{21} transmission through it using the microwave network analysis used in Sec. 2.3.3, finding;

$$S_{21} = \frac{iZ_0/L}{\omega^2 - \omega_c^2 + 2i\beta\omega\omega_c + iZ_0/L - \dfrac{\omega^2\omega_m K^2}{\omega - \omega_r + i\alpha\omega}} \quad \text{for impedance-matched cavities} \tag{2.4.28}$$

$$S_{21} = 1 - \frac{i/4Z_0C}{\omega^2 - \omega_c^2 + 2i\beta\omega\omega_c + \dfrac{i}{4Z_0C} - \dfrac{\omega^2\omega_m K^2}{\omega - \omega_r + i\alpha\omega}} \quad \text{for non-impedance-matched cavities} \tag{2.4.29}$$

We again find that the form of these S_{21} equations is equivalent to those found using the quantum and harmonic oscillator models.

2.4.4 Determining CMP Coupling Strength

Although written in slightly different forms, the coupling strength, g, used in the above models is independent of the coupling description used. The coupling strength between EM photons and a magnetic material described by this term is largely determined by the density of magnetic spins within the material. For a polarized, homogeneous, material approximated as a macrospin state the collective coupling strength between magnetic spins and EM photons g_c can be expressed as[99];

$$g_c = \frac{m_0}{2}\sqrt{\frac{\rho\mu_0\omega_c\rho_m}{\hbar}} \tag{2.4.30}$$

$$= g_s\sqrt{N} \tag{2.4.31}$$

In the first expression, m_0 is the magnetic moment of a single spin, ρ is the number of spins per unit volume in the material, μ_0 is the vacuum permeability, and ω_c is the EM photon frequency. The term ρ_m is the cavity magnetic filling factor and describes the AC magnetic field confinement within the material[100]; it can be roughly calculated as the fraction of magnetic field power interacting with a material relative to the total magnetic field power within the cavity system. In large cavity systems coupling to a small magnetic sample the value of ρ_m may thus be quite small, while for higher frequency systems where resonant photons may be generated within the magnetic sample itself ρ_m values may be close to unity. In macrospin systems, where all the spins of a sample are collectively excited to a single homogeneous excited state, the coupling strength in a CMP system can be reduced to the second expression, Eq. 2.4.31[101][102]. Here the coupling strength can be approximated as proportional to the coupling of a single magnetic spin, g_s, and increases with the square root of the number of spins within the system, N. From this expression we can clearly see that for collectively coupled macrospin systems, coupling strength increases with sample size.

Chapter 3

Achieving Indirect Photon-Photon Coupling using a Resonant Magnon Bridge

In this chapter we present the results of a study which used a CMP system to produce indirect coupling between two orthogonal cavity resonance modes. This was achieved by strongly coupling both cavity modes simultaneously to the same resonant magnon mode of a YIG sphere. Through the use of a height-adjustable cavity and an applied static field, we were able to study how tuning the resonant properties of both the cavity and magnon systems affects the dynamic properties of the indirectly coupled system. These measurements showed that the relative phase difference between the oscillations of the cavity modes has a significant effect on the nature of the indirect coupling between them. For the case where the cavity modes oscillated in-phase with each other, we found the energy transferred between them via indirect coupling was enhanced due to constructive interference between their direct coupling effects on the magnon system. Conversely, for the case where the cavity modes oscillate out-of-phase, their resonant energies were significantly reduced due to destructive interference in the magnon system. A coupled harmonic oscillator model was developed to accurately describe the dynamics and phase-dependent properties measured in our indirectly coupled system.

3.1 Introduction

In CMP systems the periodic behaviours of the photon and magnon oscillations become coupled by the effects of Ampère's and Faraday's Law, through which the motions of one system directly influence the motion of another[117]. This coupling process is not limited to interactions between two systems, it is possible to couple any number of resonators together to create a resonant system having properties dependent on those of its constituent subsystems. The coupling together of multiple subsystems also allows for systems which cannot directly interact with each other to both simultaneously couple to a third system, thereby indirectly influencing each other's motion while using the third system as a bridge over which they can transfer energy and dynamic information. This form of interaction is called Indirect Coupling, and has been extensively studied in optical systems, where two non-interacting cavity modes are coupled indirectly to each other through their interactions with a micro/nano disk resonator[153][154]. These systems are studied for their potential use in optical information technologies, and the effects of the indirect coupling between the optical cavities can be used for optical filtering, buffering, switching, and sensing in photonic crystal structures[155][156].

Recent studies have also begun to use indirect coupling to link the dynamics of magnetic systems together[45][24]. These studies individually couple resonant magnetic systems to a resonant mode of a microwave cavity, allowing the dynamic information from one magnetic system to be transferred to another indirectly. Indirect coupling of multiple systems at room temperature has attracted considerable attention due to its potential applications in hybrid quantum information processing technologies based on resonant magnon dynamics[157][45][158]; technologies similar to how indirect coupling is currently used in optical systems. Notable advancements include tuning the indirect coupling between two YIG spheres to create dark magnon modes, magnon resonance modes within a coupled CMP system which are out-of-phase to the cavity resonance mode and which hold potential for use in long term data storage applications[45]. Indirect coupling via cavity resonance modes has also recently been used to link the dynamics of magnetic systems with quantum bits known as Qubits[24], further extending the possibilities for using CMP systems in quantum computing roles.

The published works discussed above have demonstrated the potential for using cavity modes to indirectly couple resonant systems together. However indirect coupling is not limited to systems connected through cavity modes; in principle any resonant system could be used as a medium for indirect coupling, provided that there is strong coupling between the medium and each of the coupled systems. In our experiment we show that the magnon mode of a YIG sphere can be used as an indirect coupling medium, and indirectly couple the resonances two separate cavity modes together through this magnon mode. As different resonance modes in a cavity system are orthogonal and normally unable to influence each other[117], this experiment shows the possibility for using indirect coupling to exchange information between higher/lower energy resonance modes within one system; a potential which would be of great importance in new quantum data storage systems. Additionally, by showing that resonant magnon systems can be used as mediums in indirect coupling, we present the possibility of creating larger chains or webs of multiple indirectly coupled systems, whose development would be a huge step forward in quantum computing systems and networks.

3.2 Modelling Indirect Coupling

To model the effects of indirect coupling in a system of multiple oscillators, we must set up a system of coupled equations where the motion of each of the indirectly coupled subsystems influence, and are influenced by, a third oscillator. In this model, the dynamic equations for the indirectly coupled subsystems, which we will refer to as systems X and Z, will appear very similar to the direct coupling case;

$$\frac{dX}{dt} = (\omega - \omega_X)X - i\omega\alpha X - g_{XY}Y + \Omega_X \tag{3.2.1}$$

$$\frac{dZ}{dt} = (\omega - \omega_Z)Z - i\omega\delta Z - g_{ZY}Y + \Omega_Z \tag{3.2.2}$$

with both of these subsystems having a dynamic component determined by the amplitude the third oscillator, labelled Y. Here ω_X and ω_Z are the respective resonance mode frequencies of the X and Z systems, while α and δ describe damping factors in each respective system. Each of these indirectly coupled oscillators is driven by an external oscillating force, oscillating at a frequency ω, at amplitudes of Ω_X and Ω_Z respectively. The coupling coefficients between the indirectly coupled oscillators and the third oscillator are labelled as g_{XY} and g_{ZY}, for oscillators X and Z respectively. These coupling forces are not generally equal, as their exact values are determined by how each indirectly coupled oscillator interacts with the third oscillator. In a system involving cavity resonance modes these coupling coefficients will be closely related to the distribution of the electromagnetic fields within the cavity, which will be dependent on the frequency of these fields. Due to the coupling with oscillators X and Z, the dynamics of oscillator Y which indirectly couples them together will take the form:

$$\frac{dY}{dt} = (\omega - \omega_Y)Y - i\omega\beta Y - g_{XY}X - g_{ZY}Z + \Omega_m \tag{3.2.3}$$

where oscillator Y has a resonance frequency ω_Y, damping β, and is driven by an oscillating driving force of amplitude Ω_m.

In the system we experimentally study, the two indirectly coupled modes are produced by resonance within a cylindrical microwave cavity. Based on the design of the cavity, the resonance frequency of the TE and TM modes produced can be determined as[114]:

$$\omega_{mnp} = \frac{1}{\sqrt{\mu\epsilon}}\sqrt{\left(\frac{X_{mn}}{R}\right)^2 + \left(\frac{p\pi}{L}\right)^2} \qquad \text{TM Modes} \tag{3.2.4}$$

$$\omega_{mnp} = \frac{1}{\sqrt{\mu\epsilon}}\sqrt{\left(\frac{X'_{mn}}{R}\right)^2 + \left(\frac{p\pi}{L}\right)^2} \qquad \text{TE Modes} \tag{3.2.5}$$

where the mnp subscripts and coefficients in these resonance mode solutions are the mode numbers of the chosen resonance distribution within the cavity. The parameters R and L describe the radius and length, respectively, of the cylindrical cavity. The values for permeability, μ, and permittivity, ϵ, are determined by the material filling the interior of the cavity; in our experiment we use an air-filled cavity which allows us to approximate $\mu \approx \mu_0$ and $\epsilon \approx \epsilon_0$. Finally, the X_{mn} term represents the n-th zero of the m-th Bessel function and X'_{mn} represents the n-th zero of the derivative of the m-th Bessel function, whose values can be calculated. Each individual TM and TE mode within a cavity is defined as orthogonal to all other modes able to be generated within the cavity, with the modes obeying the following orthogonality relations across the surface boundaries of the cavity;

$$\int_S (\vec{E}_i \cdot \vec{E}_j) dS = 0 \qquad \text{For} \quad i \neq j \tag{3.2.6}$$

$$\int_S (\vec{H}_i \cdot \vec{H}_j) dS = 0 \qquad \text{For} \quad i \neq j \tag{3.2.7}$$

Where $\vec{E}_i(\vec{H}_i)$ and $\vec{E}_j(\vec{H}_j)$ are the electric(magnetic) field vectors at the boundaries of the cavity for modes labelled i and j respectively.

The third oscillator in our system, which indirectly couples these two cavity modes together, is a magnetic resonator. Strong coupling between the magnetic system and the cavity modes is achieved by exciting the Kittel magnon mode within the FM. The resonance frequency, ω_Y, of this mode is dependent on the shape and composition of the FM sample as well as on the strength of an external field, H, magnetizing the material[159]; for a spherical sample it can be calculated as:

$$\omega_Y/2\pi = \gamma(H + H_A) \tag{3.2.8}$$

where γ is the gyromagnetic ratio of the magnetic material and H_A is the anisotropy field in the sample, which may vary with sample shape and the orientation of crystalline axes within the material. Knowing that in our indirectly coupled system this resonance mode will be coupled to two distinct cavity modes, specifically the TM_{012} and TE_{211} modes, we can write the dynamic equations of each sub-component of the system in the form of a single coupled matrix. For a system in equilibrium, where aside from small variations we can take $\frac{dX}{dt} = \frac{dY}{dt} = \frac{dZ}{dt} = 0$, this matrix will appear as:

$$\begin{pmatrix} \omega - \omega_X - i\alpha\omega & -g_{XY} & 0 \\ -g_{XY} & \omega - \omega_Y - i\beta\omega & g_{ZY} \\ 0 & g_{ZY} & \omega - \omega_Z - i\delta\omega \end{pmatrix} \begin{pmatrix} X \\ Y \\ Z \end{pmatrix} = \begin{pmatrix} -\Omega_X \\ 0 \\ -\Omega_Z \end{pmatrix} \tag{3.2.9}$$

In this indirectly coupled system we set $\Omega_m = 0$ as the magnon resonance excited in the FM is not directly driven by an external force, but only through coupling to the cavity resonance modes. We also see in Eq. 3.2.9 that the coupling coefficient between the TE_{211} cavity mode (resonator X) and the magnon resonance is π out-of-phase with the coupling between the TM_{012} cavity mode (resonator Z) and the magnon resonance (becoming negative). This phase shift is introduced based on our experimental observations of the system, and may be due to the phase difference between the oscillating magnetic fields of each cavity mode at the specific location of the FM sample. The oscillation amplitudes of each subsystem (X, Y, Z) can be described as $X = xe^{-i\omega t+\phi_1}$, $Y = ye^{-i\omega t+\phi_m}$, and $Z = ze^{-i\omega t+\phi_2}$, having vector amplitudes of x, y, and z rotating between electric and magnetic fields (for the cavity modes) or about a plane perpendicular to an applied field (for the magnon mode). In general the oscillation of the cavity and magnon modes will not be exactly in phase with each other, and will have relative phase shifts of ϕ_1, ϕ_m, and ϕ_2 respectively, with the value of these phase shifts varying with applied frequency and field.

From Eq. 3.2.9 we can determine the resonant frequency and linewidth of the stable resonance modes by calculating the determinant of the 3×3 coupling matrix. Defining this matrix as M and solving for the complex eigenfrequencies ω_n, where $\det M = 0$, allows the resonant frequency of the system to be calculated as $\mathrm{Re}(\omega_n)$ and the normalized linewidth of these modes as $\mathrm{Im}(\omega_n)/\mathrm{Re}(\omega_n)$. Because the dynamics of our indirectly coupled system is defined as a 3×3 matrix, we expect 3 stable resonance modes to exist for the system. For conditions where the resonant frequencies of the individual X, Y, Z subsystems are far from each other, the resonant behaviours of the coupled system will appear almost unchanged from the uncoupled case. When the resonant frequencies of either of the cavity modes are brought near to the resonant frequency of the magnon mode, we will expect to see typical coupling behaviours such as mode anti-crossing and linewidth changes[119][121]. Only when the resonant frequencies of all three subsystems are brought near to each other will we expect the effects of indirect coupling to become visible, with the strong coupling forces between the cavity and magnon modes carrying dynamic information from one cavity system, across the magnon system, to influence the motion of the second cavity system.

3.3 Experimental Set-up

The system used to study indirect coupling consisted of a cylindrical cavity containing two excited resonance modes, each coupled to the Kittel resonance mode of a YIG sphere. The key feature allowing our system to detect the effects of indirect coupling is a specially designed microwave cavity whose height can be adjusted. This allows the resonance frequency of many of the resonance modes generated in the cavity to be shifted relative to other modes, allowing the resonances of two normally distinct modes to be brought near to each other. The cylindrical cavity was constructed from oxygen-free copper and featured a threaded plunger which could be rotated to increase/decease the length of the inner cavity. Through careful construction we were able to apply this design to our cavity while still maintaining a reasonable Q factor for the cavity (measured $Q \approx 1000 - 10000$ for most cavity modes). Microwave transmission through the cavity was measured via two input/output ports, located on opposite sides of the cavity approximately 1 cm from the base. These ports were connected to thin copper wires which extended roughly 0.5 cm into the interior of the cavity; care was taken to ensure that these wires extended far enough into the cavity to fully excite the desired cavity modes, but not so far as to produce excess damping effects on these modes. The inner diameter of the cavity was 25 mm, and the plunger assembly allowed the height to be tuned over a range between 24 and 45 mm. Within this height range we can adjust the resonance of many resonance modes of the cavity through Eqs. 3.2.4 and 3.2.5. As can be seen from these equations, and a plot of the cavity modes produced within the cavity in Fig. 3.1, all cavity modes are not equally affected by height changes; the main factor being the p value of the TM and TE mnp modes numbers (modes with $p = 0$ are seen to be entirely

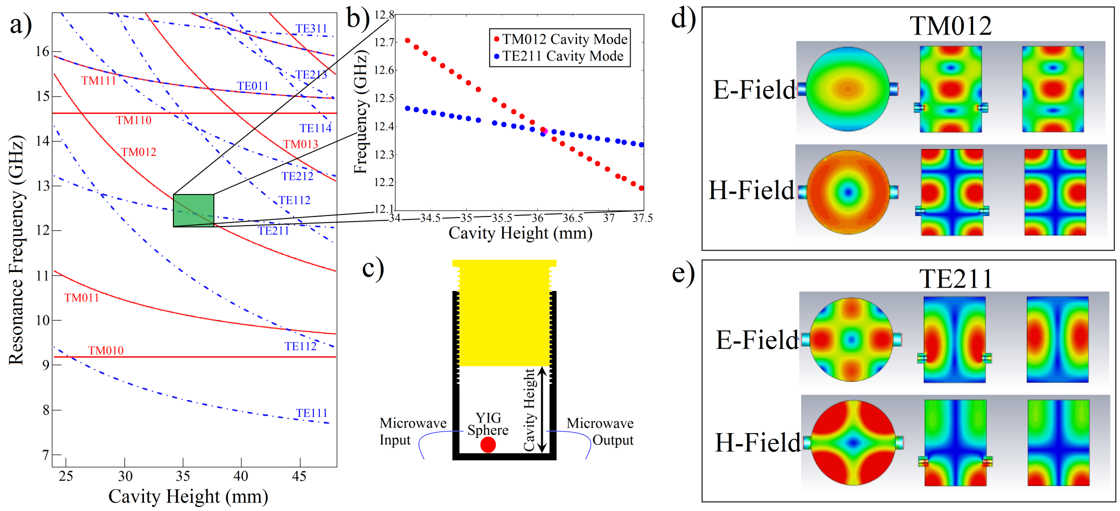

Figure 3.1: **(a)** A plot of how the resonant frequency of modes within our adjustable cavity are calculated to shift as the height of the cavity is changed. Here TE modes are plotted as dashed blue lines, and TM modes are plotted as solid red lines. **(b)** The measured dispersions of the TM_{012} and TE_{211} modes in our cavity as the cavity's height is changed. The inset to (a) relates these mode positions to our calculated values. **(c)** A schematic diagram of our height-adjustable cavity, with a spherical YIG sample placed on the bottom. **(d)** and **(e)**Show calculated E and H field distributions within the cavity for the TM_{011} and TE_{211} resonance modes, respectively. In these figures red indicated the presence of a strong field, while blue indicates a weak field. The distributions are shown as cuts along perpendicular axes of the cavity.

independent of cavity height).

From the plot of the resonant frequencies of the resonant modes produced within the microwave cavity as a function of the cavity's height, several instances where these modes cross each other as cavity height is adjusted can be seen. The two modes we chose to indirectly couple together were the TM_{012} and TE_{211} cavity modes, whose resonance frequencies were observed to cross near a frequency of 12.5 GHz. These modes were chosen for study because in our cavity their crossing point occurs at a frequency and cavity height well separated from all other cavity resonance modes, allowing their interaction with the resonant YIG mode to be studied without interference from other modes. The damping parameters of both these modes were measured independently and were found to be: $\alpha = 1.9 \times 10^{-4}$ for the TM_{012} mode, and $\delta = 0.91 \times 10^{-4}$ for the TE_{211} mode. Measuring the resonance frequencies of these two modes as the height of the microwave cavity is changed, as shown in Fig. 3.1(b), we see no signs of coupling effects such as mode anti-crossing, indicating that the two cavity modes are non-interacting. This agrees with the orthogonality relations in Eqs. 3.2.6 and 3.2.7, which state that all excited resonance modes is a cavity will be orthogonal to each other and non-interacting[114].

The ferromagnetic sample placed in our cavity was a YIG sphere with a diameter of 1 mm, held in position by a small piece of double-sided tape. Measuring the resonant properties of this sample inside the cavity, well away from cavity resonance modes, the saturation magnetization of the sample was determined to be $\mu M_0 = 0.178$ T, the gyromagnetic ratio was $\gamma/2\pi = 28\mu_0$ GHz/T, and the Gilbert damping was found to be $\beta = 1.15 \times 10^{-4}$. In placing the YIG sphere inside the cavity, special care must be taken to ensure that the microwave fields created by the TM_{012} and TE_{211} cavity modes at the location of the YIG are large enough to produce strong coupling between each cavity mode and the FM resonance mode of the YIG. As the TM_{012} mode is circularly polarized about the central axis of the cylindrical cavity [as shown in Fig. 3.1(d)], placing the YIG sample near the outer edge of the cavity with the external field applied along the radial axis parallel to the sample's position will maximize the possible coupling forces between this cavity mode and the FM resonance mode[160]. The microwave field of the TE_{211} cavity mode is not circularly uniform [as shown in Fig. 3.1(e)], thus care was taken to avoid placing the YIG sample in a position near a field node of this mode. Fortunately the sample position chosen for maximum coupling of the YIG to the TM_{012} cavity mode also produced strong coupling between the YIG and the TE_{211} mode; this YIG position relative to these modes is shown in Fig. 3.2. It is also observed that at this location the dominant driving h-fields, which are in the $\hat{z}$-plane normal to the length of the cavity, will be π out-of-phase with each other. This phase difference is accounted for in Eq. 3.2.9 by the coupling constants between each cavity mode and the YIG magnon mode having opposite signs, as the coupling forces each cavity mode will exert on the

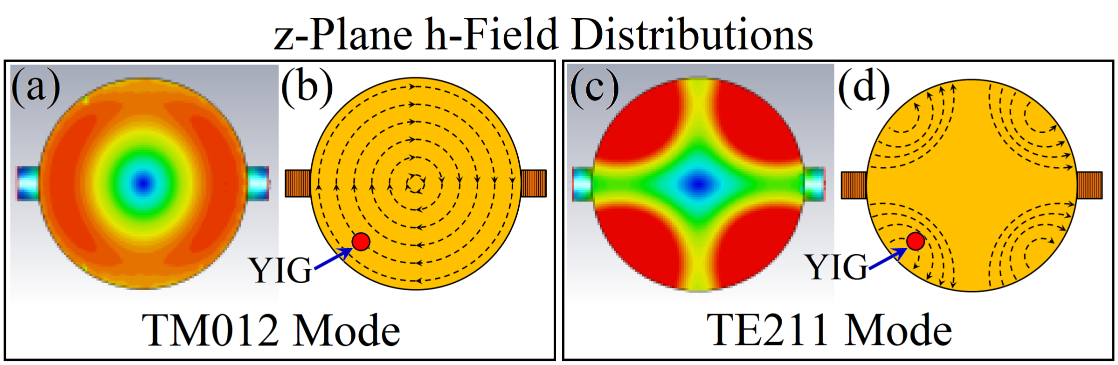

Figure 3.2: Plots of the h-field distributions in the $\hat{z}$-plane (along length of cylindrical cavity) near the YIG sample location for, showing approximate **(a)** Field Amplitudes and **(b)** Field Vectors for the TM_{012} cavity mode. Similarly shown are the **(c)** Field Amplitudes and **(d)** Field Vectors for the TE_{211} cavity mode. The approximate location of the YIG sample in relation to these mode distributions is indicated. Note that at the YIG location the field vectors are roughly anti-parallel to each other, resulting in a phase shift of π between these two modes at this location.

magnon system will be opposite each other.

During analysis of indirect coupling, we measured the S_{21} transmission through the coupled cavity/YIG system. This was done using a Vector Network Analyser (VNA), which sent a microwave signal into the microwave cavity then measured the transmission/reflection response of the coupled system. The output microwave power sent into the system from the VNA was 1 mW. An external static field applied along the radial axis of the cylindrical cavity allows the YIG sample to be excited to resonance; through tuning the strength of this field the resonant frequency of the Kittel FMR mode can be changed according to Eq. 3.2.8. Measurements performed after the YIG had been inserted into the cavity showed that the anisotropy field of the sample was $\mu_0 H_A = 0.0294$ T. This value is dependent on the orientation of the YIG's crystalline axes relative to the applied field, thus care was taken to maintain the sample in a stable configuration during measurements. The ability to control the cavity resonance mode frequencies through tuning cavity height, and to control the FM magnon mode frequency through applied static field strength, allowed us to perform numerous S_{21} transmission measurements with the resonance modes of each subsystem of the indirectly coupled cavity/YIG system at different frequencies relative to each other. This permitted us to study the properties of the CMP system as it is tuned from an uncoupled, to a coupled, and finally to an indirectly coupled state.

3.4 Coupling 2 Cavity Modes via Indirect Coupling

The effect of inserting a YIG sample into our cavity resonator is initially, before the effects of coupling are accounted for, to slightly shift the resonance frequencies of the excited cavity modes through the small perturbations the YIG makes to the electromagnetic properties of the cavity. Because the size of of the YIG sample is so small relative to the volume of the microwave cavity, these perturbative shifts will generally be minor compared to those produced by coupling effects. The effects of the inserted YIG sample on the resonant modes of the cavity only become really significant when the sample is brought near resonance. Near its resonant conditions, the YIG begins to respond to the effects of the cavity resonance, with the oscillating cavity fields driving the magnetic moment of the sample to resonance. The oscillatory motion of the magnetic moment in turn generates its own microwave field within the space of the cavity through Faraday's Law. These generated fields alter the resonant cavity mode field distributions, affecting both the resonant characteristics of the cavity modes and how they drive the magnetic sample. This process of the

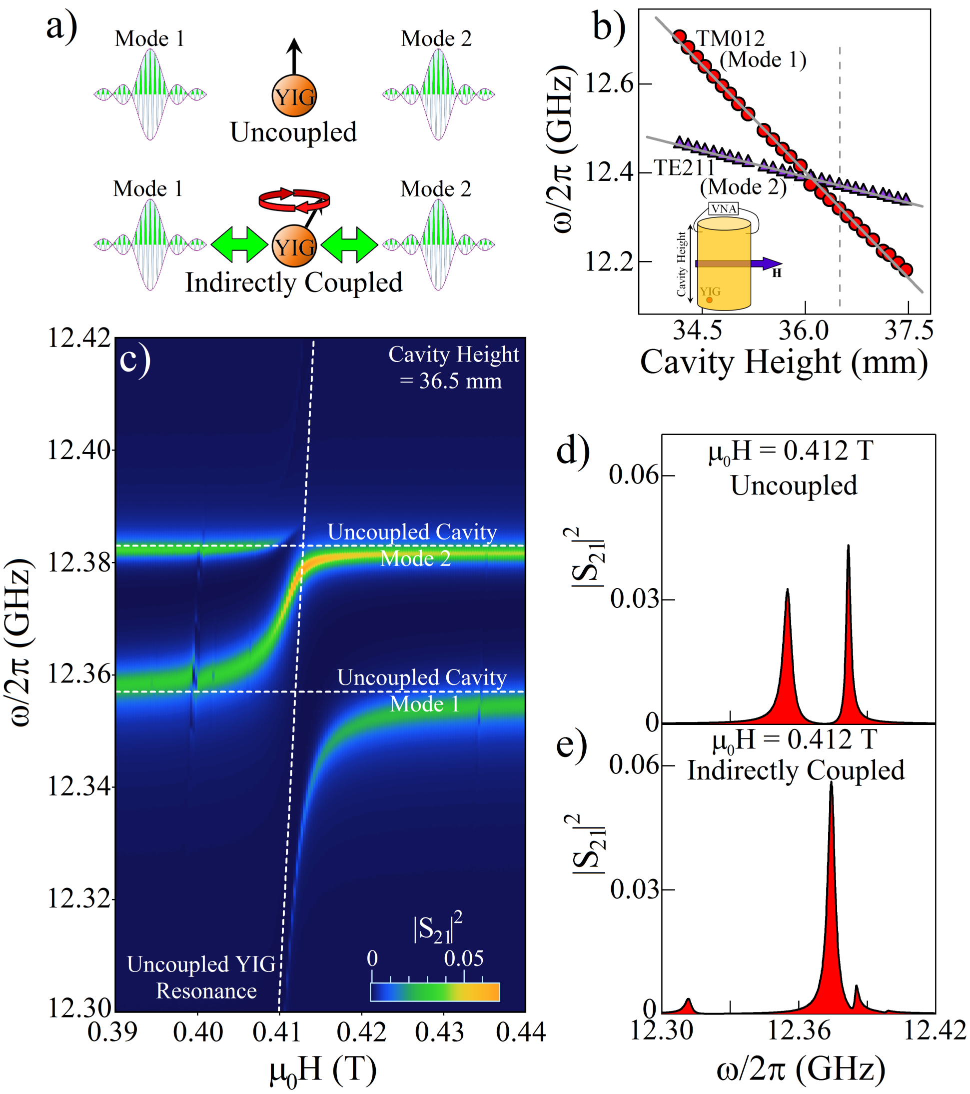

Figure 3.3: **(a)** In a system of uncoupled resonators, the motion of any single resonator does not influence the behaviour of other elements of the system. By simultaneously coupling two uncoupled resonators to a third resonant system, an indirectly coupled system is created. Here even though the cavity modes cannot directly interact, their mutual coupling to the YIG's resonance allows them to use it as bridge to exchange dynamic information between cavity modes. **(b)** The measured (markers) and modelled (solid lines) frequencies of the TM_{012} and TE_{211} cavity modes as functions of cavity height near their crossing point at a height of 36 mm. The inset shows a diagram of the Cavity/YIG system. **(c)** The transmission S_{21} of our indirectly coupled system as a function of external field strength. This measurement was taken at a cavity height of 36.5 mm [dashed line in (b)]. **(d)** The S_{21} transmission of our system in an uncoupled state [no YIG in cavity]. Here the cavity height is 36.5 mm and the external field strength is $\mu_0 H = 0.412$ T. **(e)** The S_{21} transmission of the system in an indirectly coupled state [resonant YIG in cavity], with cavity height and applied field strength unchanged from (d).

resonant cavity and magnetic subsystems both affecting and being affected by the dynamics of each other is the basis of coupled CMP systems.

In Fig 3.3 we can see the effects of this coupling on the TM_{012} and TE_{211} cavity modes. Fig 3.3(d) shows the two modes measured at a cavity height of 36.5 mm without the YIG sample inserted into the cavity, where no coupling will be present. In this plot we can see the transmission peaks representing cavity resonance modes near microwave frequencies of 12.36 GHz for the TM_{012} mode and near 12.38 GHz for the TE_{211} mode. After placing the YIG sample into the cavity, setting the height again to 36.5 mm, and applying an external field $\mu_0 H = 0.412$ T to shift the YIG subsystem's resonance frequency, ω_m, to a value between the two cavity modes, we can see the effects of coupling between the cavity and FM modes in Fig. 3.3(e). In this plot we see that this coupling will produce 3 stable resonance modes within the CMP system. Although in this situation we can no longer identify any of these modes as purely cavity or FM based, we can observe that none of these modes are identical in frequency or amplitude to the uncoupled TM_{012} and TE_{211} modes shown in Fig. 3.3(d). The change seen in both these cavity modes due to the presence of the YIG sample indicates that both are coupled to the YIG resonance mode at the conditions shown in Fig. 3.3(e), though we still require more information about the dynamics of this coupling before we can determine whether or not indirect coupling between the cavity modes present.

As the strength of the external static field on the cavity/YIG system is adjusted we are able to see the dynamics of the coupled modes change as the YIG resonance frequency ω_y shifts relative to the uncoupled cavity mode resonance frequencies; these dynamic changes are shown in Fig. 3.4 for a cavity height of 36.5 mm. In Fig. 3.4(a) we can see the resonance frequencies of the three coupled modes produced within the CMP system; when these modes are far from each other, and the cavity/FM subsystems only weakly coupled, we can label these resonance signals as H-field independent cavity modes or H-field dependent FM modes, but when coupling effects are strong the resonance signals can no longer be described as uniquely produced by a single subsystem of the CMP. Instead, where the dynamics of the subsystems are coupled together the resonance signals represent the combined oscillatory motions of both cavity and FM systems. This mixing of mode features is especially clear when we observe Fig. 3.4(b), which shows the evolution of the normalized line widths, $\Delta\omega/\omega$, of the three stable resonance modes of the CMP system as the applied static H-field is adjusted. Here we see that as the YIG resonance mode (low frequency mode for H-fields much less than coupling) is moved near to each of the cavity modes their damping effects begin to mix and their observed linewidths each begin to move towards an average value. The H-field range over which these

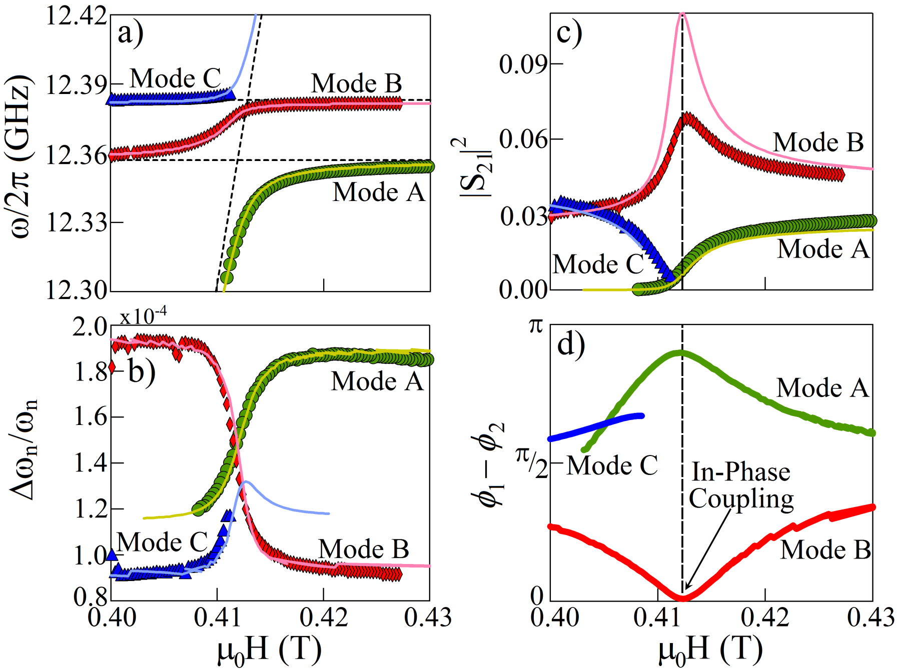

Figure 3.4: **(a)** The ω-H dispersions and **(b)** damping evolutions of the coupled modes in our system. The measured data (points) are compared to calculations from Eq. 3.2.9 (solid lines). **(c)** The measured amplitudes (points) of the coupled modes in our system, $|S_{21}|^2$, are seen to be dramatically enhanced or suppressed during coupling. These measurements are again compared to calculations from Eq. 3.2.9 using the same fitting parameters as used in (a) and (b). **(d)** The relative phase between the TM_{012} and TE_{211} cavity mode oscillations, $\phi_1 - \phi_2$, calculated during indirect coupling. The in-phase position of Mode B is seen to correspond to its maximum amplitude in (c).

linewidths are affected by coupling between cavity and FM modes matches that over which the resonance frequencies of the modes see variations due to coupling effects, showing that the resonance frequency and linewidth changes are both intrinsically connected to CMP coupling in our system.

Using the dispersion and linewidth measurements shown in Fig. 3.4 we can compare our measured results with those predicted using the indirect CMP coupling model of Eq. 3.2.9. Taking the resonance frequencies and damping values of the cavity and YIG resonant modes measured far from coupling, we can use fit the calculated mode frequencies to the measured mode frequencies to determine the coupling coefficients between the YIG sample and the TM_{012} cavity mode, g_{XY}, and between the YIG sample and the TE_{211} cavity mode, g_{ZY}. Based on this fitting, indicated by the solid lines in Fig. 3.4(a), these coupling parameters were calculated to be $g_{XY} = 60$ MHz and $g_{ZY} = 23$ MHz. These coupling coefficients were also fitted for cases where the two cavity modes were well separated from each other (not shown), with similar values being obtained. The reason for the TM_{012} mode being much more strongly coupled to the

YIG resonance signal than the TE_{211} mode is not immediately clear, but is likely related to the differing microwave field dispersions of the two modes in the vicinity of the YIG sample[161][162].

The key information indicating that indirect coupling is present in our CMP system is found when we analyse the $|S_{21}|^2$ transmission amplitudes of the resonant modes during coupling. In Fig. 3.4(c) we plot the transmission amplitudes of the observed resonances labelled Mode A, Mode B, and Mode C in Fig. 3.4(a). Far from coupling we can label these modes as almost entirely produced by the oscillatory motion of one of the three subsystems of our coupled CMP system; at very low applied H fields Mode A represents the ferromagnetic resonant mode of the YIG sample and Modes B and C would represent the cavity TM_{012} and TE_{211} modes respectively, while at very high H fields Modes A and B are the respective TM_{012} and TE_{211} cavity resonances and Mode C would be the FM resonance of the YIG sample. During coupling these modes can no longer be described by the motions of only a single oscillator, but by the combined motion of all three coupled subsystems. Observing the amplitudes of these modes near coupling in Fig. 3.4(c) we see very distinct amplitude changes for each of the three observed modes, with Mode B experiencing a clear increase in $|S_{21}|^2$ transmission amplitude within roughly the same H field range where Modes A and C experience decreases in amplitude. These amplitude changes occur near H fields where the YIG and Cavity subsystems are expected to experience maximum coupling forces from each other, indicating that these amplitude changes are tied to CMP coupling dynamics within the system.

Although amplitude changes are commonly a feature in coupled CMP systems they generally only occur in one direction, with the amplitude of coupled modes either increasing or decreasing as the system moves through the maximum coupled state and oscillatory energy is increasingly transferred from one subsystem to another. As we can generally only measure the dynamics of one of the coupled subsystems, in our system the resonance fields of the cavity modes, this energy transfer will result in amplitude decreases when energy is transferred to unmeasured subsystems. In Fig. 3.4(c) we see this as Modes A and C respectively move to lower and higher H fields their amplitudes approach zero, due to their resonant motion becoming increasingly dominated by the YIG FM resonance, which is more difficult to detect in our CMP system. Comparing the measured $|S_{21}|^2$ amplitudes to those predicted by Eq. 3.2.9 (solid lines), we see that the amplitude maximum observed in Mode B is a predicted feature of an indirectly coupled system which does not occur in coupled systems of two oscillators. The difference between the measured and predicted $|S_{21}|^2$ amplitudes of Mode B in Fig. 3.4 is not immediately clear, but may be a result of additional damping forces produced during indirect coupling which are not present in our model.

With the resonance frequencies and damping of the three modes present in our CMP system measured we now know the measured eigenvalues of the 3×3 coupling matrix of Eq. 3.2.9. For each coupled mode we can thus determine the corresponding eigenvector, which relates the oscillation phase differences between each of the three subsystems of our CMP during their coupled motion. These relative phase differences are unique to each mode and vary as the applied H field is changed and the coupling forces between the three subsystems shifts. In Fig. 3.4(d) we plot the relative phase differences between the TM_{012} cavity mode, ϕ_1, and the TE_{211} cavity mode, ϕ_2, showing how the oscillatory motions of the cavity subsystems changes during coupling. In this plot we see that the phase difference between the two cavity systems, $\phi_1 - \phi_2$, behaves very differently for each of the observed modes in our CMP system. While for Modes A and C the phase difference increases from $\pi/2$ (essentially uncoupled) to nearly π (out-of-phase oscillations) near coupling, for Mode B the phase difference instead decreases from $\pi/2$ to 0 (in-phase oscillations) during coupling. These drastic changes in relative phase between the two cavity systems during coupling provide definitive proof that indirect coupling is present in our system, since the TM_{012} and TE_{211} cavity resonances are entirely orthogonal to each other and normally unable to interact. The fact that in coupled CMP modes these two independent cavity resonances are seen to oscillate either in-phase or out-of-phase with each other indicates that information is being transferred between them via the resonant YIG mode within the cavity, creating an indirectly coupled system.

Comparing the phase differences between the two cavity systems for each measured CMP mode in Fig. 3.4(d) to the measured amplitudes of these modes in Fig. 3.4(c) provides even more information about the dynamics of the indirectly coupled system. Doing this we see that the $|S_{21}|^2$ amplitude peak in Mode B occurs at roughly the same H field where the TM_{012} and TE_{211} cavity resonances are almost exactly in phase with each other. This indicates that while indirectly coupled in Mode B the two cavity systems oscillate in-phase with one another and are able to constructively interfere with each other and transfer energy between them via their mutual coupling to the YIG resonance, increasing measured amplitude of Mode B. Conversely, we see that for Modes A and C the observed $|S_{21}|^2$ amplitude decreases roughly occur at H fields where the two cavity systems oscillate almost entirely out-of-phase with each other, indicating that in these modes the two cavity systems are destructively interfering with each other while indirectly coupled through the YIG.

3.5 Controlling Indirect Coupling

In CMP systems involving a single cavity mode coupled to a magnon mode, the magnitude of resonance frequency and linewidth shifts produced through CMP coupling is observed to increase as the resonant properties of the subsystems are moved closer together[163][164][165]. In the case of an indirectly coupled system like ours, where the dynamics of two independent cavity oscillators are coupled through their mutual interactions with a resonant FM system, the strength of the indirect coupling will be proportional to the strengths of the direct coupling forces between the FM oscillator and the cavity subsystems. To produce strong indirect coupling between the two cavity systems we thus require their uncoupled resonance frequencies to be as near as possible to each other; this allows the FM resonator to be strongly coupled to both cavity systems simultaneously. To study the effects that the resonant frequency separation between the cavity modes has on the indirect coupling between them we can make use of our adjustable-height microwave cavity, which permits us to tune the separation between the cavity modes by changing the dimensions of the cavity.

In Fig. 3.4(c) we saw that one of the resonant modes of the CMP system, labelled Mode B, reaches a peak $|S_{21}|^2$ transmission amplitude during coupling. The H field location of this amplitude peak was measured, and found to correspond to the H field where Mode B crosses the dispersion of ω_y, the uncoupled resonance frequency of the YIG Kittel mode resonance. This crossing can be seen in Fig. 3.4(a). Although the exact

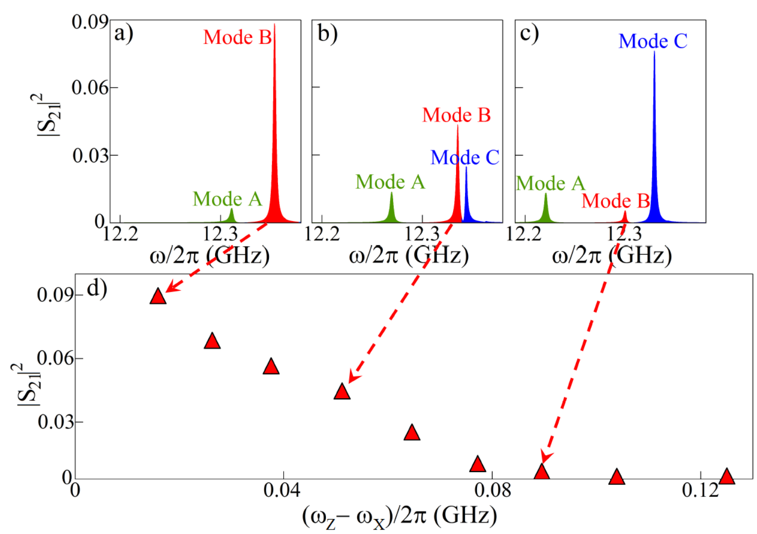

Figure 3.5: **(a)**, **(b)**, **(c)** The $|S_{21}|^2$ transmission spectrum of the observed coupled modes for different frequency differences between the TM_{012} and TE_{211} cavity modes, plotted as $\omega_Z - \omega_X$. **(d)** The amplitude of Mode B at the in-phase point of the two cavity modes, plotted as a function of $\omega_Z - \omega_X$.

position of this crossing is dependent on the coupling strengths between the cavity and FM subsystems, as well as the relative resonant frequencies and damping of the coupled subsystems, the location of the $|S_{21}|^2$ amplitude peak of Mode B, and the location of in-phase oscillation between the cavity subsystems, is seen to follow this crossing position even as these values are shifted.

Fig. 3.5 shows a plot of the $|S_{21}|^2$ transmission amplitude of Mode B relative to the uncoupled distance between the TM_{012} and TE_{211} cavity modes ($\omega_Z - \omega_X$). Here we see that as the distance between the two cavity modes decreases, the measured amplitude of Mode B increases, indicating that an increasing amount of energy is being transferred between the two cavity resonances as the indirect coupling forces between them grow larger. Figs. 3.5(a), (b), and (c) show transmission measurements taken at the crossing H field for various cavity resonance separation frequencies, with Modes A, B, and C labelled. In these plots we can clearly see that as the two cavity modes are moved closer together the amplitude of Mode B increases. We can also observe from these plots that as the $|S_{21}|^2$ transmission amplitude of Mode B increases, the amplitudes of Modes A and C correspondingly decrease (with Mode C no longer even visible in the leftmost plot). This confirms that for Mode B, where the cavity modes move in-phase with each other, the energy contained within the cavity subsystems is increased through constructive interference over their indirect coupling, with this constructive interference increasing as the cavity resonances are moved together. For Modes A and C, where the cavity modes are almost directly out-of-phase with each other, the energy within the cavity subsystems is decreased by destructive interference which also increases as the cavity resonances are moved nearer. Over the same height range which we adjusted the cavity, the change in damping of the cavity resonances was seen to change by less than 10%, showing that the observed Mode amplitude changes are indeed caused by the dynamics of indirect coupling, as opposed to mere physical changes to the coupled subsystems.

3.6 Summary

In summary our experimental observations show that our CMP system allows us to not only observe the effects of indirect coupling, but also to influence them through the use of our height-adjustable cavity. The accurate description of these indirect coupling effects using our indirect coupling model in Eq. 3.2.9 indicates that the dynamics of indirect coupling can be described through an extension of the standard CMP coupling model. However some features of indirect coupling, such as the observed increase/decrease in the

$|S_{21}|^2$ transmission amplitude of the measured CMP modes as the dynamics of the indirectly coupled cavity modes move towards in-phase/out-of-phase motion, are unique to indirectly coupled systems. The ability to control the transmission amplitude of the coupled CMP modes through changing the strength of the applied static field or the dimensions of our microwave cavity is another notable feature of our study. An apparatus which is able to both indirectly couple resonant systems together and control the dynamics and strength of this coupling would be useful in tunable optic and microwave filtering devices.

Chapter 4

Linking Cavity Magnon-Polaritons to Other Coupled Polariton Systems

In this chapter the connection between polaritons produced by magnon-photon coupling in cavity systems and polaritons produced by photons coupling to other material excitation states is explored. Although the light-matter interactions in all coupled polariton systems are expected to be the same, differences between how photons are introduced to material systems during coupling and differences in measurement techniques, mean polaritons produced in CMP systems have transmission spectra which have been difficult to reconcile with polariton coupling models used for other systems. By modelling magnon behaviour during CMP coupling using an effective permeability, based on the volume fraction of magnetic and non-magnetic materials within a cavity during CMP coupling, we show that the observed differences between polaritons in cavity systems and those in other light-matter coupled systems is a result of differing proportions of resonant photons interacting with material excitations during coupling. Using a height adjustable-cavity, allowing the resonant photon mode to be adjusted during CMP coupling, measurements similar to those performed in other polariton systems were performed in our CMP system. These measurements showed that the polariton gap, which is indicative of the creation of polaritons during light-matter coupling, is present in CMP systems, but with a much reduced amplitude. The measured CMP polariton gap was found to agree with that predicted by our effective permeability model, confirming that this model can accurately describe how interactions between photons and material excitations can produce polariton states in coupled light-matter systems.

4.1 Introduction

At a quantum level interactions between photons and materials can be described through the creation of quasi-particles called polaritons, which mediate the transfer of energy and information between the photon and material excitations[166]. There are many varieties of polariton which can be created, with the type mainly depending on the specific material excitation states involved in the coupling[167][168][169][170]. In general these polariton coupled systems display many common features, including mode anti-crossing, damping evolution, and phase induced line shape changes near the coupling point[124][137]. At a basic level, since the underlying light-matter interactions will remain the same, one would expect the effects of polariton coupling to be independent of the individual material excitations involved in the coupling. However, one feature commonly observed in higher frequency measurements of phonon-polaritons (produced by infrared photons coupling to collective lattice vibrations in a material) and exciton-polaritons (produced by optical photons coupling to electron hole or quantum well excitations in a material) has till now not been observed in measurements performed on cavity MP systems. Called the 'Polariton Gap', this feature appears as a frequency band in which no stable polariton modes are possible[167][169][171][172]. This polariton gap is a result of interactions between photon excitations and the dynamic permeability/permittivity of materials near resonance and antiresonance frequencies[173]. In phonon-polariton and exciton-polariton systems this gap can be directly observed and measured by tuning the resonant frequency (k wavevector) of the input photons to the coupled system[167][172]. As the polaritons produced in these systems will have different energies for photons coupled to resonant and antiresonant material excitations, and since between these material excitation states large damping effects block photon propagation[140], a frequency band where no coupled polariton mode can be excited (for any k value) becomes visible as the photon system is tuned.

In contrast, coupling in CMP systems like the ones used in our experiments are typically measured by tuning the resonant behaviour of the magnon system. This produces transmission dispersions which contain mode anti-crossing and lineshape changes, but notably do not exhibit a polariton gap[124][137]. The reason for this may be because even though typical dispersion measurements in CMP systems might find regions where coupled polariton modes cannot be excited, the specific frequency of these regions will change as the magnon system is tuned, leaving no clear polariton gap frequency band where coupled modes are absent for all magnon configurations. The absence of a visible polariton gap in CMP systems has been of some interest to researchers in the field of magnon-photon coupling, since without confirmation that this gap is present the exact nature of light-matter coupling in cavity systems is unclear and a common coupling model for both CMP and other polariton systems cannot be developed.

It is clear that the main reason for the disagreement between measurements of CMP coupling and coupling in other polariton systems is due to the specific process of taking measurements in each system. In higher frequency polariton systems it is relatively easy to control the k wave vector of photons input into the system by changing their frequency[171][172]. Within cavity systems however, the frequency (k wave vector) of photon excitations is determined by the dimensions of the cavity, making consistent measurements of coupling to a magnon mode at different k values difficult without specially designed systems. To study the connection between magnon-polaritons in cavity systems and polaritons produced in other systems we design a microwave cavity with an adjustable height, allowing us to produce a coupled CMP system which can be measured by tuning either the magnon resonance state (through changing static field strength) or the photon k vector (through changing cavity height). The ability to perform both types of measurements on a single coupled CMP system gives us an unprecedented ability to compare them, both to each other and to measurements performed on other coupled systems. We are thus able to use these comparisons to develop a polariton coupling model which describes all observed features of both CMP and other coupled systems.

4.2 Modelling Magnon-Polariton Coupling

The interaction between electric and magnetic fields, and thus the interaction between photon and magnon systems, is governed by Maxwell's equations[116][117]. From these equations, the propagation of an electromagnetic wave travelling through a material can be described through its wave vector k;

$$[k^2 - \omega^2 \epsilon(\omega)\mu(\omega)]h_{em} = 0 \tag{4.2.1}$$

where ω is the frequency of the wave and h_{em} is its amplitude. The parameters $\epsilon(\omega)$ and $\mu(\omega)$ respectively describe the permittivity and permeability of the material the wave is travelling through; in general both these material properties may depend on the frequency of the travelling wave[7].

The effects of the relation described by Eq. 4.2.1 in magnetic materials near resonant frequencies are plotted in Fig. 4.1, which shows how the permeabilities and wave vectors of three related systems are expected to change based on the frequency of an input electromagnetic signal. The plots in the left column of this figure describe an electromagnetic wave travelling through air. In this case, the relative permittivity and permeability of air are independent of frequency (at least within the frequency ranges we measure)[7]. As shown for μ_{air} in Fig. 4.1(b), there will be no magnetic coupling effects influencing the travelling wave's propagation. The resulting $\omega - k$ dispersion can thus be described as $k^2 = (\omega^2\epsilon_{air}\mu_{air})/c^2$, and is shown in Fig. 4.1(c).

The centre column of Fig. 4.1 describes the case for an electromagnetic wave travelling through a magnetic material. This scenario is related to the systems used to study phonon-polariton and exciton-polariton coupling (except in these systems it is typically material permittivity changes that produce resonant features), where photons are sent directly into a material sample to study coupling interactions. In this case the relative permeability of the magnetic material, μ_m will have a strong dependence on the frequency of the electromagnetic signal, especially near its resonant frequency. For simplicity, and because for many magnetic materials the change in ϵ is minor compared to the change in μ[174], we shall assume ϵ is approximately constant within the frequency range we are interested in here (in phonon-polariton and exciton-polariton systems the reverse assumption is applied). For a magnetic material polarized by an external field parallel to the propagation of the input electromagnetic signal (and to k), we can expect MP coupling effects to exert the following relation on μ_m in response to the electromagnetic signal[174];

$$\mu_m = 1 + \chi_L + \chi_T \tag{4.2.2}$$

where, following from the Landau-Lifshitz-Gilbert equation (for small damping), the variables χ_L and χ_T refer to the longitudinal and transverse elements of the Polder tensor[175]. These elements are here defined as;

$$\chi_L = \frac{\gamma M_0 \omega_{FMR}}{\omega_{FMR}^2 - \omega^2} \tag{4.2.3}$$

$$\chi_T = \frac{-i\gamma M_0 \omega}{\omega_{FMR}^2 - \omega^2} \tag{4.2.4}$$

The parameters γ and M_0 describe the gyromagnetic ratio and saturation magnetization, respectively, of the magnetic material. The term ω_{FMR} describes the uncoupled ferromagnetic resonance frequency of the material, which for a bulk medium would occur at $\omega_{FMR} = \gamma H$, where H is the strength of an applied static field[174].

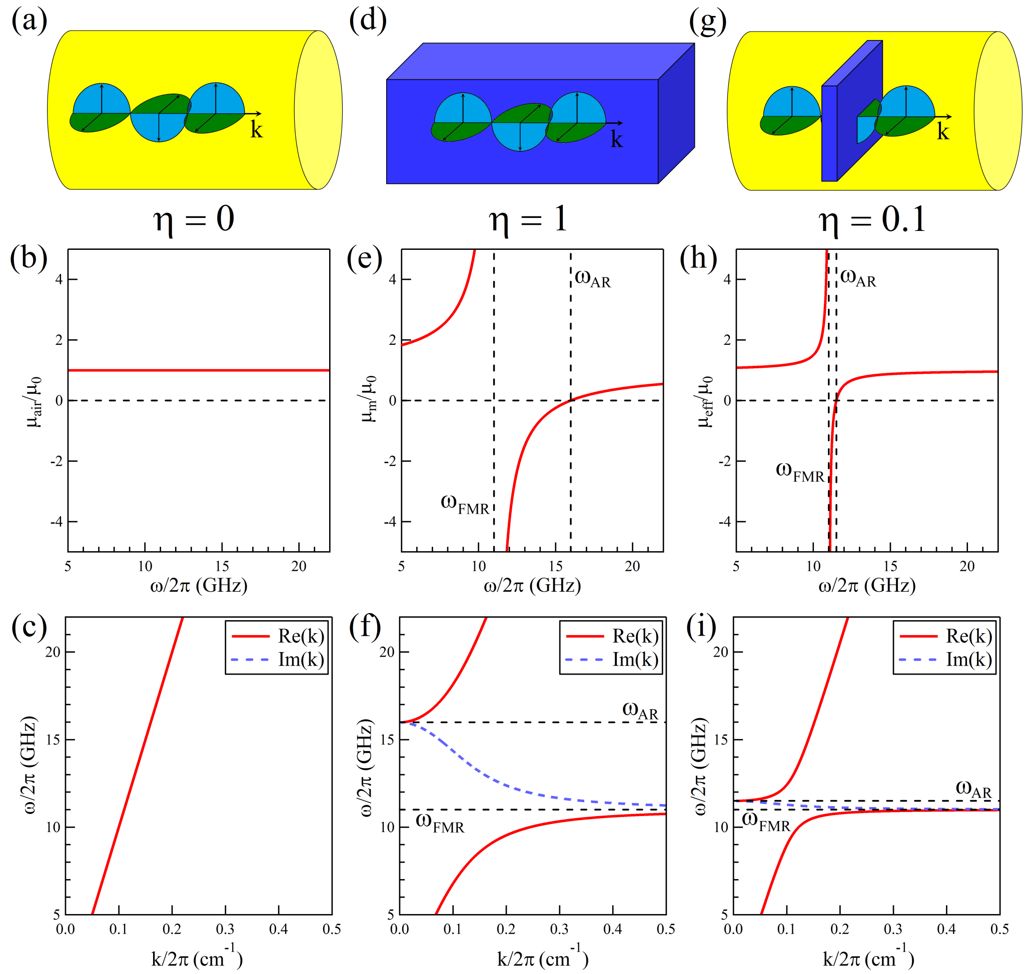

Figure 4.1: **(a)** In an empty cavity [filling factor η = 0] the permeability of the air inside **(b)** is independent of ω. **(c)** In this cavity, the magnitude of the propagation wave vector of EM waves, k, through the cavity increases linearly with ω. **(d)** For the case where the EM wave is travelling through a magnetic material [η = 1] the material permeability will exhibit a strong dependence on ω. **(e)** At ω_{FMR} the value of μ_m diverges, and at a higher frequency (called the antiresonance frequency), ω_{AR}, crosses zero. **(f)** The change in μ_m produces a wave vector k which approaches ∞ at ω_{FMR} and equals zero at ω_{AR}. Between these two values a negative μ_m value results in an entirely imaginary k value. **(g)** For a cavity partially filled with both air and a magnetic material, we can use Eq. 4.2.5 to approximate the filling factor of the system. **(h)** Modelling for $\eta = 0.1$, we see the effective permeability of the system, μ_{eff}, behave similar to μ_m in (e), but with the distance between ω_{FMR} and ω_{AR} reduced by a factor of η. **(i)** For a partially filled cavity the k vector also behaves similar to the $\eta = 1$ case, but again with the distance between ω_{FMR} and ω_{AR} reduced by a factor of η. Between ω_{FMR} and ω_{AR} the imaginary k values [dashed blue lines] seen in (f) and (i) prevent EM waves from passing through the material, meaning no resonance modes can be observed at these frequencies.

Looking at μ_m as frequency, ω, is changed in Fig. 4.1(e), we see several important features related to the coupling between photon and magnon systems. The most notable occurs at $\omega = \omega_{FMR}$, where we observe μ_m becoming divergent and approaching $\pm\infty$. This divergent behaviour indicates that at ω_m the material is almost entirely absorbing the incident wave, an effect caused by the magnetic moments in the material being excited into resonant motion by the electromagnetic wave. This absorption of the incident wave can be seen in Fig. 4.1(f), where at ω_{FMR} we can see that the the k vector of this wave approaches ∞, indicating that electromagnetic propagation is completely blocked at this frequency. This feature of magnon-photon coupling is known as ferromagnetic resonance and has been well studied[76][159]. A second notable feature in Fig. 4.1 occurs at a frequency $\omega_{AR} = \omega_{FMR} + \gamma M_0$, where $\mu_m = 0$ in the material. At this frequency a behaviour known as ferromagnetic antiresonance (FMAR) occurs, where coupling between the photon and magnon systems produces dynamics within the material that make it almost entirely transparent to electromagnetic waves at this frequency[175][176][140]. This transparency is visible in Fig. 4.1(f) where k approaches zero at ω_{AR}, resulting in near perfect transmission of electromagnetic waves through the material.

For frequencies between ω_{FMR} and ω_{AR} we can see in Fig. 4.1(e) that the value of μ_m is negative. Referring back to Eq. 4.2.1 we can see that this will result in a wave vector, k, which has a purely imaginary value. The result of this imaginary wave vector is to induce a large amplitude decay in the incident electromagnetic wave as it attempts to pass through the material. This effectively blocks the transmission of all signals with frequencies between ω_{FMR} and ω_{AR}, leaving a visible frequency gap in the $\omega - k$ dispersion shown in Fig. 4.1. Within this frequency range MPs are being generated as the electromagnetic wave interacts with the magnetic material, however they experience large damping forces (due to k having a large imaginary value) and quickly decay. Unlike the case for other ω values, there is no stable mode possible for MPs within this frequency range. The presence of this $\mu_m < 0$ frequency range is a characteristic feature of polariton coupling and the $\omega - k$ frequency gap that is produced is termed a 'Polariton Gap', an expected feature in systems coupling light-matter dynamics.

In our coupled CMP system, instead of having our EM wave travel through a homogeneous medium, we confine it to a microwave cavity partially filled with a magnetic material. This situation is described by the plots in the right-hand column of Fig. 4.1. In this case, we cannot define a single varying μ_m to be present throughout the system, as multiple materials with different permeabilities are present within the cavity. However, we can find an approximate solution to Maxwell's equations by calculating an average μ_m

value for the coupled system. To do this we calculate the filling factor, η, of the magnetic material within the cavity. This filling factor will depend on the field distribution, h_{em}, within the cavity and magnetic material, and can be calculated as the total magnetic energy stored in the magnetic material as a fraction of the total magnetic energy stored in the entire coupled CMP system[100]. Defining V_m as the volume of the magnetic material within the cavity, and V_{cav} as the total volume of the coupled CMP system (equal to the internal volume of the cavity), the filling factor can be written as;

$$\eta = \frac{\int_{V_m} |h_{em}| dV}{\int_{V_{cav}} |h_{em}| dV} \tag{4.2.5}$$

In general, mode dependent field distributions within both the cavity and magnetic subsystems will make calculating an exact value for η difficult. However, if we assume a roughly homogeneous field distribution within the system, then the integrals in Eq. 4.2.5 become very simple to calculate and the filling factor for the CMP system can be described as the volume ratio of the system's component subsystems, $\eta = V_m/V_{cav}$. This allows us to define the effective permeability, μ_{eff}, in the CMP system as;

$$\begin{aligned} \mu_{eff} &= \mu_0 \left(\mu_{air} \frac{V_{cav} - V_m}{V_{cav}} + \mu_m \frac{V_m}{V_{cav}} \right) \\ &= \mu_0 (1 - \eta + \eta \mu_m) \end{aligned} \tag{4.2.6}$$

where for the second expression we have approximated $\mu_{air} = \mu_0$. Applying this effective permeability to our expression for the wave vector in Eq. 4.2.1, the microwave dispersion in our coupled CMP system can be expressed as;

$$k^2 = \omega^2 \epsilon \mu_0 (1 - \eta + \eta \mu_m) \tag{4.2.7}$$

It should be remembered here that the magnetic permeability, μ_m, still has the frequency dependence described by Eqs. 4.2.2, 4.2.3, and 4.2.4. The right-hand side plots in Fig. 4.1 show the expressions for μ_{eff} and k as functions of input ω for the case of $\eta = 0.1$. This case would represent a coupled CMP system where the cavity is 10% filled with a magnetic material, which is still a significantly higher η value than we experimentally study (in our coupled CMP measurements typically $\eta \sim 2 \times 10^{-5}$), but allows us to see the effect of changes to η. In Fig. 4.1(h) we see that, as a function of ω, the behaviour of μ_{eff} for $\eta = 0.1$ is very similar to that of μ_m seen in Fig. 4.1(e). Both μ_m and μ_{eff} are observed to diverge to $\pm\infty$ at $\omega = \omega_{FMR}$ and both permeabilities are later seen to cross zero at a somewhat higher ω value. However, the frequency distance between ω_{FMR} and this zero crossing is seen to be significantly reduced for the CMP case where $\eta = 0.1$. Similarly, in Fig. 4.1(i) we that a visible polariton gap remains for $\eta = 0.1$, but that the position of ω_{AR} (still corresponding to $\mu_{eff} = 0$) has moved closer to ω_{FMR}, reducing the magnitude of the frequency gap. On inspection we can see that the magnitude of the polariton gap has been reduced by a factor of 0.1 by changing η from 1 to 0.1, indicating that a direct correlation exists between the filling factor, η, and the size of the polariton gap in a CMP system.

Taking the case for $\eta = 0$, representing the EM wave travelling through an empty cavity shown in Fig. 4.1(a), we can see that Eq. 4.2.7 becomes exactly equal to the equation for an EM wave in free space and the μ and k plots in Figs. 4.1(a) and (b) are reproduced. If we take the case for $\eta = 1$, representing a cavity entirely filled with material and similar to the system modelled in Fig. 4.1(d), we find that $\mu_{eff} = \mu_m$ and the MP coupling plots of Figs. 4.1(e) and (f) can be reproduced. Thus we find that by modelling the overall permeability of a coupled CMP system as an average effective permeability using Eq. 4.2.6 allows us not only to reproduce EM free-space dispersions and dispersions similar to those seen in phonon-polariton and exciton-polariton systems, but also to model the dispersions of coupled CMP systems. This effective permeability, μ_{eff}, thus provides a theoretical link between uncoupled EM waves, polariton coupling in phonon and exciton systems, and coupling in CMP systems, showing that the same physical description of polariton coupling can be used to describe all three systems. From the effects changes to μ_{eff} are expected to have on the observed polariton gap we can also expect that in experimental CMP systems such as ours (where $\eta \sim 2 \times 10^{-5}$) the magnitude of the measured polariton gap will be significantly reduced, though should remain detectable using the right measurement techniques.

4.3 Experimental Set-Up

To produce our coupled CMP system, we inserted a small sample of ferrimagnetic Yttrium Iron Garnet (YIG) into a cylindrical microwave cavity. This YIG sample was spherical in shape and had a diameter of 1 mm; further details of the sample are given in Sec. 2.2. During measurements this sample was positioned on the bottom of the microwave cavity, somewhat offset from the inner edge (shown in the inset of Fig. 4.2); this location was chosen for the YIG as it was expected to experience strong microwave fields from the cavity mode (TM_{011}) during coupling, and was a convenient location to keep the sample stable during measurements (no special YIG sample holder needed to be designed and placed inside the cavity). By applying an external static field, H, to the YIG sample we can excite it to resonant motion. Measuring the resonant frequency of the sample well away from cavity resonance modes (to minimize coupling effects) allows us to determine the material properties of the YIG. The measured resonance signal (the Kittel mode) occurs at a frequency $\omega_{FMR}/2\pi = \gamma(H + H_a)$, with the gyromagnetic ratio measured to be $\gamma = \mu_0 \times 176$ GHz/T and the anisotropy field of the spherical sample $\mu_0 H_a = -2.4$ mT. Further measurements on the YIG sample determined its saturation frequency to be $\omega_m/2\pi = 4.984$ GHz and its damping coefficient to equal $\alpha = 1.5 \times 10^{-4}$. Since we find $\alpha \ll 1$, we can assume that the magnon damping effects in this system will be small, allowing us to remove these damping terms from our calculations.

The key to our ability to measure a polariton gap within a coupled CMP system is our use of a specially designed microwave cavity with an adjustable height, the same cavity used in the experiments of the previous section. Using a plunger-type mechanism this cylindrical cavity is able to adjust its height, h, over a range between $h = 25 - 45$ mm, allowing the wave vector, k, of the cavity system to be adjusted. This cavity was constructed of oxygen-free copper and had a radius of $R = 12.5$ mm. For this cavity design, the resonant frequency of the TM_{011} mode (which has a circular EM field distribution about the cavity axis) can be calculated from;

$$\begin{aligned}\omega_{Cav}/2\pi &= \frac{1}{\sqrt{\epsilon\mu_0}}\sqrt{\left(\frac{X_{01}}{R}\right)^2 + \left(\frac{\pi}{h}\right)^2} \\ &= \frac{1}{\sqrt{\epsilon\mu_0}}\sqrt{k_\perp^2 + k_z^2}\end{aligned} \tag{4.3.1}$$

Here the term X_{01} refers to the first root of the zeroth Bessel function. In the second part of Eq. 4.3.1 we have relabelled the components within the square root term to $k_\perp$ representing the radius-dependent k wave vector component perpendicular to the axis of the cavity, and k_z representing the height-dependent wave vector component parallel to the axis of the cavity (labelled $\hat{z}$). The total k wave vector of the cavity system is a combination of $k_\perp$ and k_z where $k^2 = k_\perp^2 + k_z^2$. From Eq. 4.3.1 we can see that $k_z = \pi/h$, thus as we adjust the height of the cavity we are able to see ω_{Cav} shift. This is shown in Fig. 4.2, where we compare measured ω_{Cav} values for the TM_{011} cavity mode to those calculated from Eq. 4.3.1. As the height of the cavity decreases we can see corresponding increases in ω_{Cav}, similarly increasing the

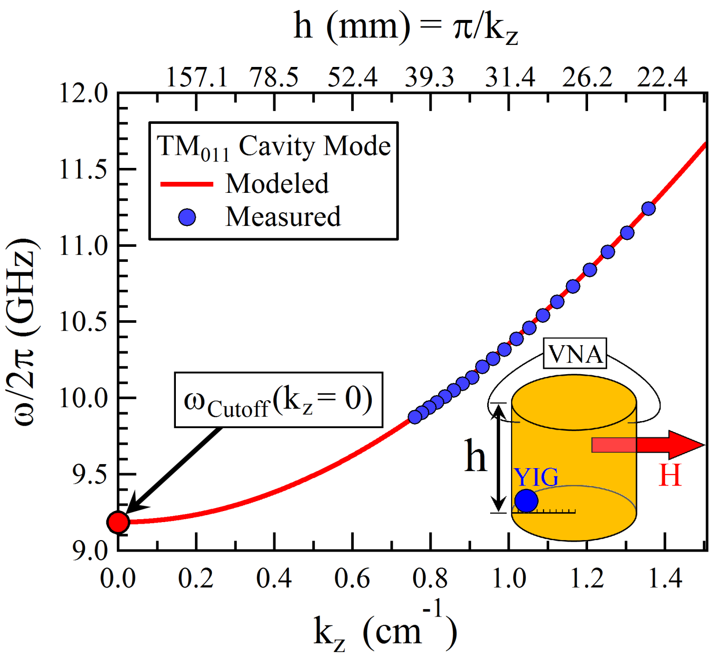

Figure 4.2: A plot of the $\omega - k_z$ dispersion of the TM_{011} resonance mode of our empty cavity. The solid curve is calculated from Maxwell's equations, while the markers denote measured resonance frequencies of this mode at various cavity height (k_z) values. Due to the geometry of our cavity, the TM_{011} mode frequency does not equal zero at $k_z = 0$, but approaches a minimum value indicated by ω_{Cutoff}. The inset depicts a diagram of the cavity/YIG system used during our measurements.

height of the cavity results in a general decrease in ω_{Cav}. However, we can note from Fig. 4.2 that as $k_z \to 0 (h \to \infty)$ the resonance frequency of the TM_{011} mode approaches a minimum value defined by $\omega_{Cutoff}/2\pi = k_{\perp}/\sqrt{\epsilon\mu_0} = 9.186$ GHz. This minimum k wave vector is generated entirely by the radial $k_{\perp}$ component of the TM_{011} cavity mode; as this component is independent of cavity height we have no way to change it in our system.

During measurements we examine the dynamics of the coupled CMP system by measuring the microwave transmission, $|S_{21}|^2$, through the system. Due to physical limitations, our height-adjustable cavity is unable to be adjusted over the entire $k_z = 0 - \infty$ range; the k_z range able to be measured can be interpreted from the spread of measured data points in Fig. 4.2, and ranges from $k_z/2\pi \sim 0.12$ to $k_z/2\pi \sim 0.22$. However, measuring over this range we are able to gather sufficient data to be able to fit our measured data to Eq. 4.2.7 and use this fitting to extrapolate the resonant frequencies of the system for extremely high/low k_z values. By changing the resonant properties of either the cavity subsystem (through changing cavity height) or the YIG sample (though changing applied H field strength) we are able to perform measurements of the resonant modes of the coupled system as functions of either k_z or H, with each measurement type produced leaving the other subsystem unaffected except through coupling effects. This allows us to study the connection between the polariton gap seen in $\omega - k_z$ measurements and the Rabi gap (the ω separation between coupled modes when $\omega_{Cav} = \omega_{FMR}$) observed in $\omega - H$ measurements.

4.4 $\omega - k_z$ Dispersion Measurements

We first investigate the effects of magnon-photon coupling in our CMP system by measuring the microwave transmission, $|S_{21}|^2$, through the system as a function of cavity height, h, and microwave frequency, ω, producing an $\omega - k_z$ dispersion plot like that shown in Fig. 4.3. During these measurements an external static field with a constant magnitude of $\mu_0 H = 0.4$ mT was applied to the system, directed along the axial vector of the YIG sample's position relative to the cavity as shown in the inset of Fig. 4.2. This applied field will polarize the magnetic moments within the YIG sample, causing it to undergo ferromagnetic resonance at a measured (far from coupling) frequency of $\omega_{FMR}/2\pi = 10.35$ GHz. This uncoupled YIG resonance frequency is indicated by the horizontal dashed line in the $\omega - k_z$ plot in Fig. 4.3(a). Leaving ω_{FMR} constant, we can adjust the height of the cavity to move the resonant frequency of the TM_{011} cavity mode, whose uncoupled dispersion is indicated by the diagonal dashed line in Fig. 4.3(a), near to ω_{FMR}. As ω_{FMR} and ω_{Cav} are brought near to each other the coupled CMP resonant modes, indicated by maxima in the measured $|S_{21}|^2$ dispersion of Fig. 4.3, are seen to display anti-crossing behaviour indicative of MP coupling, separated by a distinct Rabi gap. At a frequency somewhat higher than ω_{FMR} a second mode anti-crossing is visible, produced through CMP coupling between the TM_{011} cavity mode and a spin wave mode within the YIG sample. Although the physics of CMP coupling are expected to be the same for all magnon resonance modes when coupled to a cavity mode, for this study we choose to focus on CMP coupling displayed by the Kittel FM resonance mode at ω_{FMR}.

The $\omega - k_z$ coupling dispersion measured in Fig. 4.3(a) can be accurately described by the CMP coupling model developed in Eq. 4.2.7; in Fig. 4.3 the modelled dispersion is plotted as solid lines. Since the properties of both the YIG and cavity subsystems were both measured independent of coupling effects, the only unknown parameter when fitting the data in Fig. 4.3(a) is the value of the filling factor, η. For our coupled CMP system, a good fitting is obtained for $\eta = 2.3 \times 10^{-5}$; this value is similar to the ratio between the volumes of the YIG and cavity subsystems ($V_m/V_{cav} \sim 2.7 \times 10^{-5}$ for k_z near coupling), which supports the validity of our use of η to calculate the effective permeability of the CMP system. Although

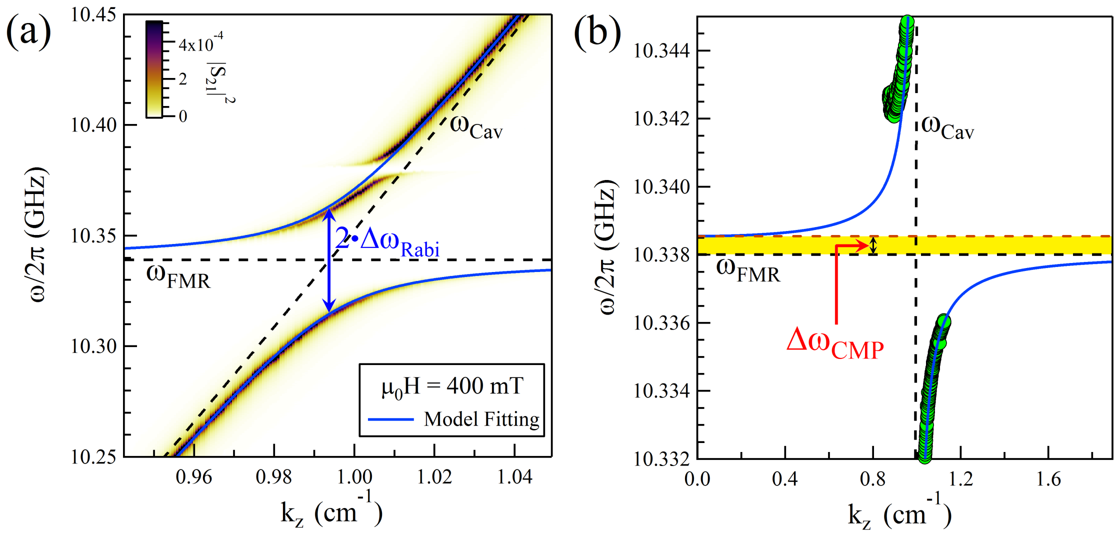

Figure 4.3: **(a)** An $\omega - k_z$ plot of the microwave $|S_{21}|^2$ transmission through our cavity/YIG system at an external field strength of 400 mT. Here the solid blue curve fits this data to the model in Eq. 4.2.7 using $\eta = 2.3 \times 10^{-5}$, and the black dashed lines indicate the positions of the YIG and cavity resonance modes for the case of no coupling. The Rabi coupling gap is half the frequency gap between the upper and lower modes, measured at the k_z value where the uncoupled cavity and YIG modes would cross. **(b)** Zooming in near ω_{FMR}, we see that the resonance frequencies of the measured modes do not approach the same ω value for $k_z \to 0$ and $k_z \to \infty$. This leaves a frequency gap, $\Delta\omega_{CMP}$ (highlighted in yellow), where no resonance modes can occur. A second coupling feature can be seen in (a) near $\omega/2\pi = 10.38$ GHz, and is the result of a spin wave magnon mode coupling to the photon system.

our measured range of k_z is not sufficiently large to allow us to directly see a polariton gap in the $\omega - k_z$ dispersion in Fig. 4.3, we can use our fitted value of η from this plot to extrapolate the resonance frequencies of the coupled CMP system at extreme k_z values. As discussed previously in this section, the magnitude of the CMP polariton gap, $\Delta\omega_{CMP}$, will be equal to the difference between the YIG FMR and FMAR frequencies. These frequencies are defined by the cases where $k_z \to \infty$ (ω_{FMR}) and $k_z \to 0$ (ω_{AR}), thus from Eq. 4.2.7 we expect the following dispersion limits in our CMP system;

$$\omega(k_z \to \infty) = \omega_{FMR} \tag{4.4.1}$$

$$\omega(k_z \to 0) \simeq \omega_{FMR} + \frac{\gamma M_0 \eta}{1 - \left(\frac{\omega_{Cutoff}}{\omega_{FMR}}\right)^2} \tag{4.4.2}$$

From the above equations, we can see that a notable influence on the coupled behaviour of a CMP system is contained within the $[1 - (\omega_{Cutoff}/\omega_{FMR})^2]^{-1}$ term in the $k_z \to 0$ case. This term is produced by the $k_\perp$

component of the cavity's wave vector and remains constant even as k_z goes to zero. In our coupled system this term becomes quite significant when ω_{FMR} is near the value of ω_{Cutoff}; for the data in Fig. 4.3 this term is seen to increase the value of $\Delta\omega_{CMP}$ by a factor of 5, compared to the case where $\omega_{Cutoff} = 0$. It would be possible in theory to remove this term by setting the external field such that $\omega_{FMR} \gg \omega_{Cutoff}$, this would essentially eliminate the influence of the $k_\perp$ wave vector component on CMP coupling within the system and result in our $\omega - k_z$ dispersions being more similar to the $\omega - k$ dispersions measured in other polariton coupled systems, however this would be impractical for our measurements.

A complication in measuring the $\omega - k_z$ dispersion of our CMP system is that our method for tuning k_z (through changing the height of the cavity) will also shift the value of the filling factor, η. As a result of this connection, a true fitting of the dynamics of our coupled CMP system to Eq. 4.2.7 would be very inaccurate over large spans of k_z. Our actual measured range of k_z, as seen in Fig. 4.3, is relatively narrow which allows us to approximate η as constant within this range. The comparison of this measured data to Eq. 4.2.7 fits the data within the measured range to this constant η value, then extends outside the measured range to extreme k_z values to allow us to see the polariton gap, $\Delta\omega_{CMP}$, produced by the fitted η value. If our system were able to cover the large k_z ranges required to experimentally see the polariton gap we would see that, due to the changes to η as k_z is changed, the magnitude of the gap would steadily decrease as $k_z \to 0$ due to the effect of $\eta = V_m/V_{cav} \to 0$. Fig. 4.3(b) shows a magnified plot of Fig. 4.3(a) at frequencies near ω_{FMR}; at this scale the polariton gap, $\Delta\omega_{CMP}$, is clearly visible as the difference between the modelled CMP resonance modes at high and low k_z values. Because η is so small within our coupled system the measured polariton gap, $\Delta\omega_{CMP}/2\pi = 0.54$ GHz, is significantly smaller than that typically seen in optical MP coupled systems where $\eta = 1$. However the presence of this polariton gap in our fitting results, and the agreement between our fitted and measured η values, shows that this filling factor is an important factor controlling the effective permeability, and thus coupling dynamics, of CMP systems.

4.5 $\omega - H$ Dispersion Measurements

Due to the necessity of using a specially designed adjustable cavity to perform $\omega - k_z$ dispersion measurements, most studies of coupled CMP systems perform simpler $\omega - H$ dispersion measurements to investigate coupling dynamics in these systems. Despite the fact that many features of coupling are found in both types of measurements, both theoretical and experimental studies have shown that the polariton gap, $\Delta\omega_{CMP}$, is not visible in $\omega - H$ dispersions[47][177]. To compare these two measured dispersion types to each other we set our adjustable cavity to a constant height of $h = 31.6$ mm ($k_z/2\pi = 0.158$ cm^{-1}) as the strength of the external static field, H, was adjusted. This produces a constant cavity resonance frequency of $\omega_{Cav}/2\pi = 10.34$ GHz, which allows us to write the CMP coupling described in Eq. 4.2.7 as;

$$(\omega^2 - \omega_{Cav}^2)(\omega - \omega_{FMR}) - (\eta\gamma M_0)\omega^2 = 0 \tag{4.5.1}$$

Looking at this expression we can see that it is equivalent to coupling expressions for CMP systems developed using quantum[178][179], equivalent circuit[180][181], and transfer matrix models[182], where in Eq. 4.5.1 we let the coupling coefficient $g = \omega\sqrt{\eta\gamma M_0}$. Coupling between magnon and photon systems is dependent on the magnetization of the ferromagnetic material $\omega_m = \gamma M_0$ (how easy it is for the electromagnetic field to influence the motion of the FM) and the relative number of photons and FM spins in the coupled system (odds of a photon and spin to interact). For a cavity system with many more excited photons

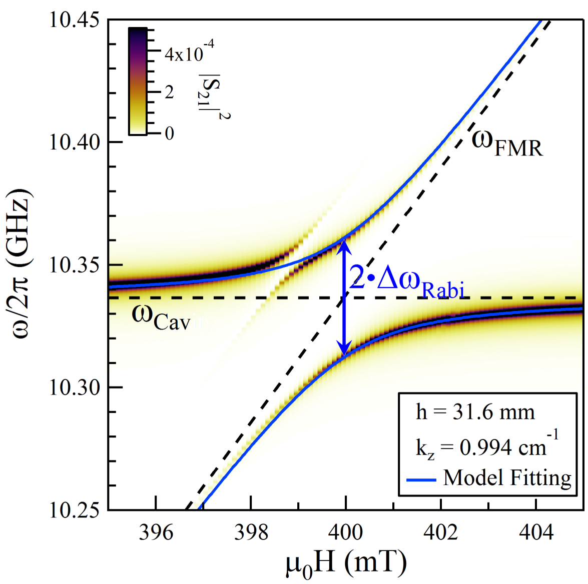

Figure 4.4: An ω-H plot of the $|S_{21}|^2$ transmission through our cavity/YIG system at a cavity height of 31.6 mm ($k_z/2\pi) = 0.158$ cm^{-1}). Similar to Fig. 4.3, the solid blue curve fits this measured data to the model in Eq. 4.2.7 using $\eta = 2.3 \times 10^{-5}$, with the dashed black lines indicating the positions of the YIG and cavity resonance modes for the case of no coupling. Here the Rabi coupling gap is half the frequency gap between the upper and lower modes, measured at the $\mu_0 H$ field where the uncoupled cavity and YIG modes would cross. For equal η values, $\Delta\omega_{Rabi}$ will be equal in measured $\omega - k_z$ and ω-H dispersions. A smaller second coupling feature is visible in this dispersion and is produced by a spin wave magnon mode coupling to the photon system, the same as seen in Fig. 4.3(a).

than spins, such as ours, the filling factor provides a simple method for estimating the relative chance of interaction between the photon and magnon system, as in CMP systems coupling is typically proportional to the square root of the number FM spins within the system. Of course this approximation assumes a homogeneous field distribution within the coupled system; the exact coupling coefficient between the magnon and photon components will depend on the exact EM field dispersions within the CMP system.

By tuning the applied static field strength, H, applied to our CMP system, and leaving k_z constant, the $\omega - H$ dispersion in Fig. 4.4 was produced. This plot has a very similar appearance to the $\omega - k_z$ plots shown in Fig. 4.2, except that now ω_{Cav} is seen to remain constant while ω_{FMR} is seen to linearly increase with H. Where the resonance frequencies of the two systems approach each other we can clearly see a mode anticrossing between the coupled modes, indicating strong coupling between them. By choosing to set the height of our cavity such that $k_z/2\pi = 0.158$ cm^{-1} in Fig. 4.4, we chose the value where $\omega_{FMR} = \omega_{Cav}$ in the $\omega - k_z$ dispersion of Fig. 4.2. In doing this we ensured that the applied field at the point where $\omega_{Cav} = \omega_{FMR}$ in Fig. 4.4 would occur at $\mu_0 H = 400$ mT, which is the magnitude of the constant H field applied to the coupled CMP system in our previous $\omega - k_z$ measurements. Setting H and k_z to these

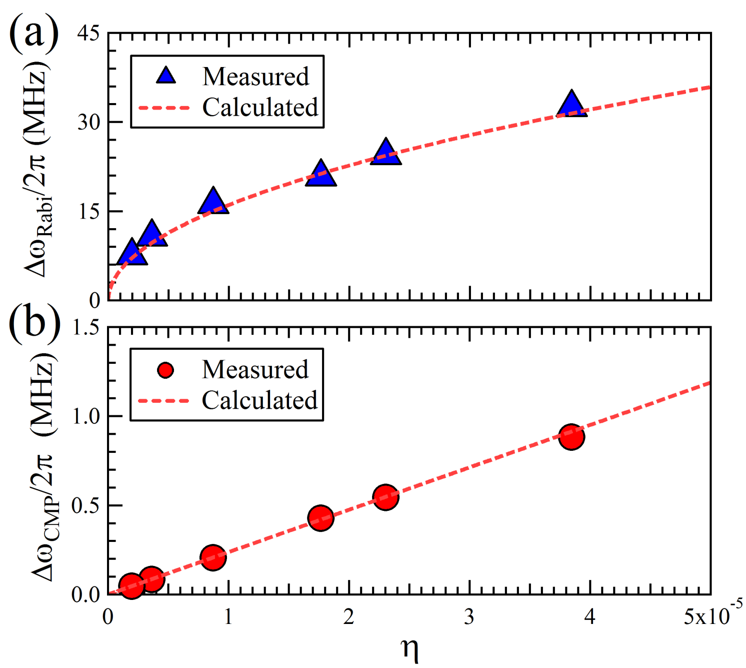

Figure 4.5: **(a)** A plot of the magnitude of $\Delta\omega_{Rabi}$ (triangles) from $\omega - k_z$ measurements as a function of η, compared to values predicted from Eq. 4.5.2 (dashed curve). **(b)** A plot of the magnitude of $\Delta\omega_{CMP}$ (circles) from $\omega - k_z$ measurements as a function of η, compared to values predicted from Eqs. 4.4.1 and 4.4.2 (dashed curve).

specific values means that during our $\omega - H$ and $\omega - k_z$ dispersion measurements the conditions where $\omega_{FMR} = \omega_{Cav}$ will be exactly the same; $\mu_0 H = 400$ mT and $k_z/2\pi = 0.158$ cm^{-1}. This allows us to directly compare the frequency differences between the two coupled CMP modes in both dispersions. The frequency gap between coupled modes at the $\omega_{Cav} = \omega_{FMR}$ point is called the Rabi gap, $\Delta\omega_{Rabi}$, and is a typical feature found in coupled multimode systems driven by an oscillating field[183]. From Eq. 4.5.1 the magnitude of the Rabi gap can be calculated (assuming $\eta < 5\%$) as;

$$\Delta\omega_{Rabi} = \sqrt{\frac{1}{2}\eta\gamma M_0 \omega_{Cav}} \tag{4.5.2}$$

The relation between this Rabi gap and the square root of $\eta\gamma M_0$, representing the total number of spins averaged over the volume of the cavity, is consistent with the predictions of other models[184]. Fitting the measured dispersion in Fig. 4.4 to Eq. 4.5.1 (solid lines) we can obtain a good fit to the observed coupled modes for $\eta = 2.3 \times 10^{-5}$, the same η value used to obtain a good fitting of the $\omega - H$ dispersion in Fig. 4.2 to Eq. 4.2.7. The agreement between both fittings indicates that the magnitudes of the polariton gap, $\Delta\omega_{CMP}$, and the Rabi gap, $\Delta\omega_{Rabi}$, are both related through the filling factor of the CMP system, η. The individual relations of both these gaps to η is further shown in Fig. 4.5, where the square root dependence of $\Delta\omega_{Rabi}$ and the linear dependence of $\Delta\omega_{CMP}$ are both seen to agree well with values from the measured $\omega - H$ and $\omega - k_z$ dispersions.

4.6 Summary

In summary, we have developed a model which links polariton coupling behaviours in cavity MP systems to those observed in other polariton systems through the effective permeability of the CMP system. In CMP systems this effective permeability value is calculated using the volume fraction of magnetic and non-magnetic materials inside the cavity, and thus is related to the proportion of resonant photons interacting with the magnon mode during coupling. Using a specially designed cavity with an adjustable height, we were able to adjust the resonance frequency of the cavity mode during CMP coupling. This allowed us to perform $\omega - k$ dispersion measurements on the CMP system similar to those typically performed in other polariton systems. These measurements revealed that a polariton gap is produced during CMP coupling, with its reduced amplitude (compared to other polariton systems) agreeing with that predicted by our effective permeability based coupling model. Changing the magnon resonance frequency, by adjusting the strength of the static field applied to the CMP system, further allowed us to measure the $\omega - H$ dispersion and Rabi coupling gap of the system during coupling. These measurements showed that both the $\omega - k$ polariton gap and $\omega - H$ Rabi gap are related through effective permeability of the CMP system. By accurately reproducing the results of $\omega - k$ dispersions typical in measurements of polariton systems and $\omega - H$ dispersions typical in cavity MP measurements, our model shows that the dynamics of polariton coupling in both systems are identical. Further, by relating the coupling gaps of both measurements to the relative permeability of the CMP system, we reveal that this value is crucial for controlling the dynamics of polariton coupling in cavity MP systems.

Chapter 5

Non-Linear Damping in CMP Systems

In this chapter we explore the effects of non-linear dynamics in CMP systems. Using a Fabry-Perot-like microwave cavity, we excite the magnon mode in a YIG sphere to high amplitudes where non-linear Kerr effects become significant. When this magnon mode is coupled to a cavity mode to produce a CMP system, the bistabilities produced by the non-linear magnon system are reproduced in the transmission lineshape of the coupled CMP modes. By tuning the resonant frequency of the magnon system relative to that of the cavity system we are able to produce bistable behaviours in the CMP system beyond those found in uncoupled magnon systems. Developing a model for non-linear behaviour in CMP systems through the addition of a non-linear Kerr term to the coupled CMP Hamiltonian, we are able to accurately reproduce the array of bistability features observed in our CMP system. Further, this model allows us to calculate the conditions necessary to produce bistable behaviour in CMP systems, allowing the limits of bistable CMP features to be accurately determined. The method used to produce our non-linear CMP model is additionally not limited to non-linearity in magnon systems, and can be extended to other coupled systems containing non-linear components.

5.1 Introduction

During resonance, we have seen that the dynamics of a magnetic moment can be analysed using harmonic oscillator models, and are in many respects quite similar to those of a classical swinging pendulum system. Pendulum systems have been studied for centuries and consequentially the equations governing their motion are well known[185][186]. However, in most cases these equations cannot be solved analytically;

meaningful results can only be approximated for low amplitude oscillations. This is also the case for resonant behaviour in ferromagnetic materials, which can be analytically solved only for cases where their magnetic moments are nearly parallel to an applied field[149]. As for many experimental systems the power actually transferred to the resonant system is relatively small, most studies of ferromagnetic resonance are able to accurately describe their results using low amplitude, parallel-to-field, approximations. However, as studies of ferromagnetic resonance became easier and more frequent, interest in the physics behind and the effects of higher amplitude resonance were increased[77][187].

In 1955 Anderson and Suhl studied the effects of high amplitude resonance in ferromagnetic systems and found that effects similar to those found in pendulum systems, notably a resonance peak shift, should be present[188]. These effects were soon experimentally verified in 1958 by high power resonance studies on YIG[189]. However, due to the difficulty in effectively transferring power to ferromagnetic systems, some of the more notable features of high power resonance remained undetected. It wasn't until 2009, when Y.S. Gui *et al.* published the results of experiments using their newly developed spin dynamo (which is able to efficiently inject a much stronger microwave field into ferromagnetic samples than traditional radiative measurements) that large resonance peak shifts and the notable 'foldover' behaviour were first measured in ferromagnetic conductors[77]. These results came at a critical period in the field of spintronics, for methods to generate dc currents through spin rectification and spin pumping had just been developed[62][85]. As both these methods rely on the resonant motion of ferromagnetic materials, the new spin dynamo technique for injecting strong microwave fields into samples allowed many new studies in the background of these effects to be performed[190][191].

By placing a magnetic material with non-linear dynamics into a cavity, strong coupling interactions between the photon and magnon systems can produce entirely new non-linear dynamics[192], such as enhanced cooling in optomechanical systems[193][194]. Recently, the first bistabilities have been produced in coupled MP systems composed of a small YIG sample placed in a high-Q 3D microwave cavity[195]. The cavity used in this experiment is specially designed with a third port connected to a loop antenna in the vicinity of the YIG sphere which efficiently drives the magnon mode at high powers to produce non-linear effects. Inspired by this new discovery, we created a non-linear CMP system by placing a highly polished YIG sphere in the center of a Fabry-Perot-like cavity[196]. This CMP system allows a high input power to excite the YIG magnon mode to the non-linear regime, while allowing us to use the same frequency to both drive and measure the dynamics of the CMP system. This experimental set-up reveals a rich array of CMP bistability features, beyond what has been seen in uncoupled magnon systems.

5.2 Non-Linear Damping in Ferromagnetic Resonance

To understand the effects of high amplitude ferromagnetic resonance, we begin with the Landau-Lifshitz-Gilbert (LLG) equation[149]. This equation, at both high and low powers, governs the dynamics of a magnetic moment, $\vec{M}$, in the presence of a periodically oscillating magnetic field;

$$\frac{\partial \vec{M}}{\partial t} = -\gamma \vec{M} \times \vec{H}_{eff} + \frac{\alpha}{M_0} \vec{M} \times \frac{\partial \vec{M}}{\partial t} \tag{5.2.1}$$

Here $\vec{H}_{eff}$ describes the effective magnetic field felt by the moment (both static and periodic), γ is the gyromagnetic ratio, α is the Gilbert damping term, and $\vec{H}_{eff}$ represents the total magnetic field acting on the moments (both static and periodic). The expression M_0 represents the vector magnitude of the ferromagnetic moment, $M_0 = |\vec{M}|$. If we assume our ferromagnetic sample to be a thin film normal to the $\hat{z}$ direction and align a large static external field perpendicular to the film then the vector orientations of both $\vec{M}$ and $\hat{H}$ can be written as combinations of a large static component and much smaller oscillating components;

$$\hat{M} = (m_x, m_y, M_z) \tag{5.2.2}$$

$$\hat{H}_{eff} = (h\text{cos}(\omega t), h\text{sin}(\omega t), H - M_z) \tag{5.2.3}$$

where it is assumed that the static field is large enough to overcome the demagnetizing effects produced by the shape of the sample, allowing the magnetic moments to oscillate around an axis parallel to the applied static field, H. The electromagnetic field applied to the sample to induce resonance is taken to have a propagation vector parallel to $\hat{z}$, producing periodic magnetic fields of magnitude h and frequency ω along the $\hat{x}$ and $\hat{y}$ directions. Inserting these $\vec{M}$ and $\vec{H}_{eff}$ terms into the LLG equation produces the following coupled differential equations;

$$\frac{\partial m_x}{\partial t} = -\gamma(H - M_z)m_y + \gamma M_z h\text{sin}(\omega t) + \frac{\alpha}{M_0}(-\frac{\partial m_y}{\partial t} M_z + m_y \frac{\partial M_z}{\partial t}) \tag{5.2.4}$$

$$\frac{\partial m_y}{\partial t} = \gamma(H - M_z)m_x - \gamma M_z h\cos(\omega t) + \frac{\alpha}{M_0}(\frac{\partial m_x}{\partial t}M_z - m_x\frac{\partial M_z}{\partial t}) \tag{5.2.5}$$

$$\frac{\partial M_z}{\partial t} = -\gamma(m_x h\sin(\omega t) - m_y h\cos(\omega t)) + \frac{\alpha}{M_0}(-\frac{\partial m_x}{\partial t}m_y + m_x\frac{\partial m_y}{\partial t}) \tag{5.2.6}$$

Although in general there will exist solutions to this system of coupled equations, they can be quite complicated and not analytically solvable. However, we can arrive at an approximate solution by using Bogoliubov and Mitropolsky's asymptotic method for general oscillating systems[197]. This method assumes that the damping forces felt by the moment are small relative to the forces on the moment from the applied external fields. Using this assumption, we first calculate an approximate solution by neglecting the damping components in Eqs. 5.2.4, 5.2.5, and 5.2.6. These first order solutions are;

$$m_x = a\cos(\omega_e t) \tag{5.2.7}$$

$$m_y = b\cos(\omega_e t + \varphi) \tag{5.2.8}$$

$$M_0^2 = m_x^2 + m_y^2 + M_z^2 \tag{5.2.9}$$

In these solutions we have defined a and b to be the respective amplitudes of the moment's oscillations in the $\hat{x}$ and $\hat{y}$ directions, with φ being the phase difference between these oscillations. ω_e is the eigenfrequency of the system when damping factors are neglected. For the case where $m_x, m_y \ll M_z$, we can approximate Eq. 5.2.9 as;

$$M_z \approx M_0 - \frac{m_x^2 + m_y^2}{2M_0} \tag{5.2.10}$$

For ease of calculations when we are taking m_x and m_y to be small, it is often assumed that $M_z \approx M_0$. Taking this assumption, the Kittel equations of motion for this system can be found. However, by letting M_z vary with m_x and m_y (and thus oscillation amplitude) we are able to find several interesting non-linear features in this resonant ferromagnetic system. With these zero-damping first order solutions we can now return to the full expressions of Eqs. 5.2.4, 5.2.5, and 5.2.6; inserting Eqs. 5.2.7, 5.2.8, and 5.2.10 we can now attempt to calculate solutions for the damped LLG equation. From the first two of the coupled differentials we get;

$$-a\omega_e \sin(\omega_e t) = -b\gamma(H-M_0)\cos(\omega_e t+\varphi) - \frac{\gamma b}{2M_0}[a^2\cos^2(\omega_e t)+b^2\cos^2(\omega_e t+\varphi)]\cos(\omega_e t+\varphi) \quad (5.2.11)$$

$$-b\omega_e \sin(\omega_e t+\varphi) = a\gamma(H-M_0)\cos(\omega_e t) + \frac{\gamma a}{2M_0}[a^2\cos^2(\omega_e t)+b^2\cos^2(\omega_e t+\varphi)]\cos(\omega_e t+\varphi) \quad (5.2.12)$$

Because we are analysing a harmonic oscillating system, we know that $\sin(\omega_e t)$ and $\cos(\omega_e t)$ cannot equal zero for all t values. Therefore we expect the sums of the $\cos(\omega_e t)$ and $\sin(\omega_e t)$ terms in Eqs. 5.2.11 and 5.2.12 will be equal to zero. Expanding the squared components in the last term of our equations using a Fourier series, and taking up to the cubic term, we find the following relations;

$$\cos\varphi = 0 \quad (5.2.13)$$

$$a\omega_e + \gamma b(H - M_0 + \frac{a^2+3b^2}{8M_0})\sin\varphi = 0 \quad (5.2.14)$$

$$\gamma a(H - M_0 + \frac{3a^2+b^2}{8M_0}) + b\omega_e \sin\varphi = 0 \quad (5.2.15)$$

From the first of these relations we can see that the phase difference between the $\hat{x}$ and $\hat{y}$ oscillations, φ, is $\pm\pi/2$, which intuitively makes sense for these orthogonal axes. If we assume that the motion of the magnetic moment is roughly circular about the applied field axis, then the amplitudes of the $\hat{x}$ and $\hat{y}$ oscillations will be equal, with $a \approx b$. With these relations, Eqs. 5.2.14 and 5.2.15 tell us that the eigenfrequency of the oscillating magnetic moment will be $\omega_e = \gamma(H - M_0 + \frac{a^2}{2M_0})$, with corresponding eigenvectors of (1,±1). Here we first see the effects of letting M_z vary in Eq. 5.2.10; for the case of negligibly small amplitude oscillations ($a = 0$) the eigenfrequency of the magnetic moment will be $\omega_e = \gamma(H - M_0)$, however allowing larger amplitude oscillations causes M_z to decrease and results in a higher eigenfrequency.

As we have taken the precession of the magnetic moment to be circular, we will have $\frac{\partial M_z}{\partial t} = 0$. This allows us to replace our amplitude parameters with a term representing the cone angle θ (angle between $\vec{M}$ and external field $\vec{H}$), where $a = b = M_0\text{sin}\theta$. Inserting this cone angle term into Eqs. 5.2.7, 5.2.8, and 5.2.10, we find the following expressions for the motion of the magnetic moment during resonance;

$$m_x = M_0\text{sin}\theta\text{cos}(\omega_e t + \phi) \approx M_0\theta\text{cos}(\omega_e t + \phi) \tag{5.2.16}$$

$$m_y = M_0\text{sin}\theta\text{sin}(\omega_e t + \phi) \approx M_0\theta\text{sin}(\omega_e t + \phi) \tag{5.2.17}$$

$$M_z = M_0\text{cos}\theta \approx M_0\left(1 - \frac{\theta^2}{2}\right) \tag{5.2.18}$$

where we have taken θ as small enough that $\text{sin}\theta \approx \theta$. The parameter ϕ is inserted here to represent possible phase differences between the precession of the ferromagnetic moment and the oscillations of the applied microwave field driving this motion. We can now take these non-linear equations describing $\vec{M}$ and insert them into our coupled LLG Eqs. 5.2.4 and 5.2.5. Combining terms from these equations gives the following expression;

$$\left[\gamma\left(H - M_0 + \frac{1}{2}M_0\theta^2\right) - \omega\right]\theta\text{sin}(\omega t + \phi) + \alpha\omega\left(1 - \frac{\theta^2}{2}\right)\theta\text{cos}(\omega t + \phi) = \gamma\left(1 - \frac{\theta^2}{2}\right)h\text{sin}(\omega t) \tag{5.2.19}$$

Expanding $\text{sin}(\omega t + \phi)$ and $\text{cos}(\omega t + \phi)$ using Fourier expansions and collecting $\text{sin}(\omega t)$ and $\text{cos}(\omega t)$ terms as before allows us to find the following expression relating the cone angle of the moment's resonance, θ, to the amplitude of the applied oscillating field, h.

$$\theta^2 = \frac{(1 - \theta^2/2)^2 h^2}{\left(H - M_0 + \frac{1}{2}M_0\theta^2 - \frac{\omega}{\gamma}\right)^2 + \left(\frac{\alpha\omega}{\gamma}\right)^2\left(1 - \frac{1}{2}\theta^2\right)^2} \tag{5.2.20}$$

Taking $\omega/\gamma + M_0 = H_0$ (the applied field needed to excite resonance for $\theta = 0$) and $\alpha\omega/\gamma = \Delta H$ (the line width of the resonance signal for $\theta = 0$), and assuming that $\theta^2/2 \ll 1$, this relation can be simplified to;

$$\theta^2 = \frac{h^2}{\left(H - H_0 + \frac{1}{2}M_0\theta^2\right)^2 + \Delta H^2} \tag{5.2.21}$$

This relation is similar in form to that of a non-linear driven pendulum, and we shall see that it shares many of the non-linear pendulum's characteristic features as well. Calculating the resonance field, H_r, of this system, we find;

$$H_r = H_0 - \frac{1}{2}M_0\theta^2 = H_0 - \frac{1}{2}M_0\frac{h^2}{\Delta H^2} \tag{5.2.22}$$

where the later term arises because at resonance $\theta^2 = h^2/\Delta H^2$. Thus we see that, just like in a swinging pendulum system, the applied field(frequency) required to produce resonance will decrease(increase) proportional to the square of the power of the driving force on the system. Calculating the dependence of θ on h using Eq. 5.2.21 we find that for small h values a unique cone angle, θ, is produced for any applied field value. However, at larger h values, as the shift in H_r increases, we will find that within a certain range of H values multiple stable θ solutions are possible. This range is termed the 'foldover' region, due to the resonance peak shifting far enough away from its $\theta = 0$ value that it begins to fold over itself. The presence of this foldover produces a hysteresis-like state within the foldover range, where H field measurements are held at one of two stable θ values until the field is shifted outside of the foldover range. Once outside of the foldover range sudden jumps in the cone angle θ of the resonance may occur as the multiple stable states within the foldover range converge onto a single stable state outside. The H field position of these jumps can be calculated as the fields where the slope of $d\theta/dH$ reaches infinity in Eq. 5.2.21. Calculating this derivative;

$$\frac{d\theta}{dH} = -\frac{\theta\left(H - H_0 + \frac{1}{2}M_0\theta^2\right)}{\left(H - H_0 + \frac{1}{2}M_0\theta^2\right)\left(H - H_0 + \frac{3}{2}M_0\theta^2\right) + \Delta H^2} \tag{5.2.23}$$

This derivative will reach infinity when the denominator equals zero. Using the quadratic equation we can calculate two real roots for θ, describing the cone angle θ at which each of the two expected jumps will occur.

$$\theta_{up}^2 = \frac{-4(H_{up} - H_0) - 2\sqrt{(H_{up} - H_0)^2 - 3\Delta H^2}}{3M_0} \tag{5.2.24}$$

$$\theta_{down}^2 = \frac{-4(H_{down} - H_0) + 2\sqrt{(H_{down} - H_0)^2 - 3\Delta H^2}}{3M_0} \tag{5.2.25}$$

where the subscripts up and down indicate whether the sudden change in the dynamics of the system is due to an increase in θ or a decrease in θ. If we simplify these expressions by assuming that the linewidth of the signal, ΔH, is significantly smaller than the resonance shift due to non-linear effects, so that $(H_{up/down} - H_0)^2 \gg 3\Delta H^2$ (assumes high relatively high amplitude oscillations), we can calculate the approximate cone angles where these H_{up} and H_{down} jump positions will occur. We thus find;

$$\theta_{up}^2 \approx \frac{-2(H_{up} - H_0)}{M_0} \tag{5.2.26}$$

$$\theta_{down}^2 \approx \frac{-2(H_{down} - H_0)}{3M_0} \tag{5.2.27}$$

We can then insert these cone angle values into Eq. 5.2.21 to find the relation between the H field position of these jumps and the strength of the input oscillating field h.

$$H_{up} \approx H_0 - \frac{3}{2}h^{2/3}M_0^{1/3} \propto P^{1/3} \tag{5.2.28}$$

$$H_{down} \approx H_0 - \frac{1}{2}\frac{h^2}{\Delta H^2}M_0 \propto P \tag{5.2.29}$$

where the total power input into the system by the oscillating field, P, is taken as proportional to h^2. Thus we see that these jump positions have very different dependences on the parameters of the system. While the H_{up} point will decrease relative to $P^{1/3}$ and be proportional to $M_0^{1/3}$, the H_{down} point will decrease linearly with input power and will have an inverse relationship to ΔH^2.

5.3 Extending Non-Linear Damping to Coupled CMP Systems

A non-linear magnetic system coupled to a resonant microwave cavity can be described by the following Hamiltonian (where $\hbar = 1$)[195];

$$H' = \omega_c a^\dagger a + \omega_m b^\dagger b + K b^\dagger b b^\dagger b + g(a^\dagger b + a b^\dagger) + \Omega(a^\dagger e^{-i\omega t} + a e^{i\omega t}) \tag{5.3.1}$$

where $a^\dagger$ and a describe the creation and annihilation operators of the cavity photons at a frequency of ω_c, and $b^\dagger$ and b describe the creation and annihilation operators of magnons within the magnetic material at a frequency ω_m. Thus the first two terms of this Hamiltonian describe the individual energies of the cavity and magnon systems. The fourth Hamiltonian term describes the energy produced through coupling interactions between the two systems, with a coupling strength g. The final term in the Hamiltonian describes the energy transferred to the cavity system by an applied oscillating force of magnitude Ω and frequency ω. The non-linearity of the FM system in this Hamiltonian is contained within the third term which depicts an energy proportional, through the Kerr constant K, to the square of the FM system's amplitude. This square relation is found in uncoupled FM resonance and is a result of the Kerr effect, where the refractive index of a material changing due to its resonant motion[198][199]. To make the following calculations simpler, we first transform the Hamiltonian of our coupled system to a rotating reference frame, with respect to the applied driving field, using the unitary transformation $R = e^{-i\omega a^\dagger a - i\omega b^\dagger b}$. This gives;

$$\begin{aligned} H &= R^\dagger H' R - iR^\dagger \frac{\partial R}{\partial t} \\ &= (\omega - \omega_c) a^\dagger a + (\omega - \omega_m) b^\dagger b + K b^\dagger b b^\dagger b + g(a^\dagger b + a b^\dagger) + \Omega(a^\dagger + a) \end{aligned} \tag{5.3.2}$$

The dissipation function, Q, for this system can be classically defined as;

$$Q = \frac{da^\dagger}{dt}\frac{da}{dt}\beta + \frac{db^\dagger}{dt}\frac{db}{dt}(\alpha + \alpha' b^\dagger b) \tag{5.3.3}$$

Here β describes the intrinsic linear damping parameter of the cavity photon, while α is the linear damping of the magnon excitation. The term α' represents the effects of non-linear damping related to the Kerr effect, which is proportional to the amplitude of the magnon excitation ($b^\dagger b$)[190]. From the Hamiltonian and the dissipation function we can determine the dynamic equations of motion for our coupled system using;

$$i\frac{da}{dt} = \frac{\partial H}{\partial a^\dagger} + \frac{\partial Q}{\partial(da^\dagger/dt)} \tag{5.3.4}$$

$$i\frac{db}{dt} = \frac{\partial H}{\partial b^\dagger} + \frac{\partial Q}{\partial(db^\dagger/dt)} \tag{5.3.5}$$

The resulting coupled dynamic equations are;

$$i\frac{da}{dt} = (\omega_c - \omega)a + gb + \Omega + \frac{da}{dt}\beta \tag{5.3.6}$$

$$i\frac{db}{dt} = (\omega_m - \omega)b + 2Kb^\dagger b + ga + \frac{db}{dt}(\alpha + \alpha' b^\dagger b) \tag{5.3.7}$$

For the coupled anharmonic oscillator systems described above, the exact dynamics may be quite complicated and are not always analytically solvable. However if we initially neglect the damping and non-linear terms we can take the system to have the periodic solutions $a = Ae^{-i\omega t}$ and $b = Be^{-i\omega t}$, with A and B representing the respective amplitudes of the cavity and magnon excitation modes. Inserting these periodic solutions into Eqs. 5.3.6 and 5.3.7 results in;

$$i\frac{da}{dt} = [(\omega_c - \omega)A + gB + \Omega - i\omega\beta A]e^{-i\omega t} \tag{5.3.8}$$

$$i\frac{db}{dt} = [(w_m - \omega)B + 2Kb^\dagger bB + gA - i\omega(\alpha + \alpha' b^\dagger b)B]e^{-i\omega t} \tag{5.3.9}$$

If the system is driven at equilibrium, where the energy supplied by the driving force is matched by the energy lost to damping, then we expect the system to be stable over relatively long periods. In this case we can state that $\frac{da}{dt} = \frac{db}{dt} = 0$ and $b^\dagger b = |B|^2$. This now gives us the equations of motion for our coupled CMP system;

$$(\omega_c - \omega - i\omega\beta)A + gB + \Omega = 0 \tag{5.3.10}$$

$$(\omega_m - \omega - i\omega\alpha + (2K - i\omega\alpha')|B|^2)B + gA = 0 \tag{5.3.11}$$

As these 2 equations contain 2 unknowns (A and B) we are able to solve for these unknowns and determine the dynamics of the system based on its intrinsic properties. Using Eq. 5.3.10 to solve for A and inserting this solution into Eq. 5.3.11 now gives us;

$$\left(\omega_m - \omega - i\omega\alpha + (2K - i\omega\alpha')|B|^2 - \frac{g^2}{\omega_c - \omega - i\omega\beta}\right) B = \frac{g\Omega}{\omega_c - \omega - i\omega\beta} \tag{5.3.12}$$

Before proceeding with further analysis, we simplify this equation to;

$$(\delta_m + 2K|B|^2 - i\omega(\alpha^0 + \alpha'|B|^2))B = \frac{g\Omega}{\omega_c - \omega - i\omega\beta} \tag{5.3.13}$$

Using the expressions;

$$\delta_m = \omega_m - \omega - \frac{g^2(\omega_c - \omega)}{(\omega_c - \omega)^2 + (\omega\beta)^2} \tag{5.3.14}$$

$$\alpha^0 = \alpha + \frac{g^2\beta}{(\omega_c - \omega)^2 + (\omega\beta)^2} \tag{5.3.15}$$

In these expressions δ_m describes the resonance frequency of the coupled FM magnon without non-linear effects. We see that the shift due to this coupling is largest near the frequency of the cavity resonance mode it is coupled to, and for the case of a linear FM system ($K = 0$ and $\alpha' = 0$) the frequency shift of the magnon mode calculated here will be the same as was calculated in previous chapters. Similarly, α^0 describes the damping of this coupled magnon mode without non-linear effects. With these substitutions we can clearly see that the remaining terms on the left-hand side of Eq. 5.3.13 relate to the non-linear resonance effects of the FM. By multiplying Eq. 5.3.13 by its complex conjugate expression, we can now obtain the following expression which links the frequency shift produced by non-linear effects to the strength of the applied oscillating field;

$$((\delta_m + \Delta_m)^2 + (\alpha^0\omega + \frac{\alpha'\omega}{2K}\Delta_m)^2)\Delta_m = \frac{2Kg^2\Omega^2}{(\omega_c - \omega)^2 + (\omega\beta)^2} \tag{5.3.16}$$

where we have let $\Delta_m = 2K|B|^2$ represent the non-linear frequency shift of the coupled magnon mode.

Calculating the magnitude of this frequency shift for various applied fields, Ω, we see that in addition to shifting the resonance frequency of the magnon mode, the presence of non-linear terms in our coupled CMP system leads to other interesting effects. At low Ω values Eq. 5.3.16 has only a single stable Δ_m solution across all δ_m values (representing a sweep of ω_m). However as Ω is increased the magnon frequency shift will become larger, eventually leading to resonance foldover similar to that seen in uncoupled FM systems. This foldover can be seen from the solutions of Eq. 5.3.16 for large Ω values, where there will exist a certain range of ω_m values where three different Δ_m solutions (two stable and one unstable) exist.

5.4 Effects of Non-Linear Damping in CMP Systems

The calculations of the previous section show that one of the most notable features produced by non-linear coupling in CMP systems is a foldover line shape. This foldover creates a bistable system within a certain range of external parameters such as applied field strength, and the exact limits of this range would be of vital importance to any possible application of this bistable behaviour. Because the bistable foldover range of the non-linear CMP system's dynamics described in Eqs. 5.3.10 and 5.3.11 is determined by the range where the magnon resonance B has multiple stable resonance amplitudes described by Eq. 5.3.16, we can determine the limits of foldover behaviour using this equation. As can be seen from the foldover lineshape, the limits of the foldover bistability (when sweeping ω_m) will occur where $\frac{d\Delta_m}{dH} = \infty$. Taking the derivative of Eq. 5.3.16 with respect to H, and remembering that when the FM is resonating in the Kittel mode $\frac{d\delta_m}{dH} = \gamma$ (γ being the gyromagnetic constant of the FM), we find:

$$\frac{d\Delta_m}{dH} = -\frac{2\gamma\Delta_m(\delta_m + \Delta_m)}{\delta_m^2 + 4\delta_m\Delta_m + 3\Delta_m^2 + (\alpha^0\omega)^2 + 4\alpha^0\omega\Delta_m\left(\frac{\alpha'\omega}{2K}\right) + 3\left(\frac{\alpha'\omega}{2K}\right)^2\Delta_m^2} \tag{5.4.1}$$

The foldover limits will thus occur at the Δ_m values where the denominator of this equation equals zero. Using the quadratic equation, we calculate these Δ_m values to be:

$$\Delta_m = \frac{-2\left(\delta_m + \alpha^0\omega\left(\frac{\alpha'\omega}{2K}\right)\right) \pm \sqrt{4\left(\delta_m + \alpha^0\omega\left(\frac{\alpha'\omega}{2K}\right)\right)^2 - 3\left(1+\left(\frac{\alpha'\omega}{2K}\right)^2\right)(\delta_m^2 + (\alpha^0\omega)^2)}}{3\left(1+\left(\frac{\alpha'\omega}{2K}\right)^2\right)} \tag{5.4.2}$$

5.4.1 Threshold Power

The first notable condition we can determine from the relation described by Eq. 5.4.2 is the threshold magnon frequency shift, Δ_m required to produce foldover. This threshold Δ_m is the minimum value where bistable solutions for the coupled non-linear CMP system can be found. For Δ_m values below this threshold there will exist only one stable solution to Eq. 5.3.16 across all δ_m values, while above the threshold Δ_m there will exist a range of δ_m values where foldover will occur and multiple solutions to Eq. 5.3.16 exist. This threshold Δ_m occurs when the two solutions described by Eq. 5.4.2 (differentiated by the $\pm$ square root term) are equal, and thus requires:

$$4\left(\delta_m + \alpha^0\omega(\frac{\alpha'\omega}{2K})\right)^2 - 3\left(1+(\frac{\alpha'\omega}{2K})^2\right)\left(\delta_m^2 + (\alpha^0\omega)^2\right) = 0 \tag{5.4.3}$$

Determining the δ_m value (and hence applied field strength, H) where this threshold occurs using the quadratic equation, we find:

$$\delta_{m,thresh} = \frac{-4\alpha^0\omega\left(\frac{\alpha'\omega}{2K}\right) \pm \sqrt{16(\alpha^0\omega)^2\left(\frac{\alpha'\omega}{2K}\right)^2 - \left(1-3(\frac{\alpha'\omega}{2K})^2\right)\left((\frac{\alpha'\omega}{2K})^2 - 3\right)(\alpha^0\omega)^2}}{1-3\left(\frac{\alpha'\omega}{2K}\right)^2} \tag{5.4.4}$$

This $\delta_{m,thresh}$ value can then be inserted into Eq. 5.4.3 to find an expression for the threshold magnon frequency shift required to produce foldover, $\Delta_{m,thresh}$. The $\pm$ resulting from the quadratic equation solution relates to whether the non-linear frequency shift is toward higher frequencies (for $K < 0$) or towards lower frequencies (for $K > 0$). Our expression for $\Delta_{m,thresh}$ can be considerably simplified if we assume that α' is small, and thus $\frac{\alpha'\omega}{2K} \ll 1$. In this case the foldover thresholds in Eqs. 5.4.4 and 5.4.2 become:

$$\delta_{m,thresh} \approx \pm\sqrt{3}(\alpha^0\omega) \tag{5.4.5}$$

$$\Delta_{m,thresh} \approx \frac{-\frac{2}{3}\alpha^0\omega\left(\pm\sqrt{3} + \frac{\alpha'\omega}{2K}\right)}{1 + \left(\frac{\alpha'\omega}{2K}\right)^2} \tag{5.4.6}$$

Inserting these threshold values into Eq. 5.3.16 allows us to determine the driving field strength, Ω_{thresh} (and hence power, $P \propto \Omega^2$) required to drive the coupled CMP system to foldover, assuming α' is small.

$$\Omega^2_{thresh} = \frac{4(\alpha^0\omega)^3\sqrt{3}}{9|K|}\left(\frac{(\omega_c - \omega)^2 + (\omega\beta)^2}{g^2}\right) \tag{5.4.7}$$

5.4.2 H Field Jump Points

For Ω values above Ω_{thresh} the two solutions of Eq. 5.4.2 will indicate the magnon frequency shift values where the upper and lower limits of foldover will occur. If α' is small then we can simplify Eq. 5.4.2 by setting $\alpha' = 0$, allowing us to determine the δ_m values at the foldover limits:

$$\Delta_{m,up} \approx \frac{-2\delta_m - \sqrt{4\delta_m^2 - 3\delta_m^2}}{3} = -\delta_m \tag{5.4.8}$$

$$\Delta_{m,down} \approx \frac{-2\delta_m + \sqrt{4\delta_m^2 - 3\delta_m^2}}{3} = -\frac{1}{3}\delta_m \tag{5.4.9}$$

where the up and down subscripts indicate the relative value of Δ_m before the critical value is crossed. At $\Delta_{m,up}$ the magnon frequency shift occupies the higher of the two stable Δ_m modes within the bistable foldover range before dropping to a lower value at the critical value described in Eq. 5.4.8, while at $\Delta_{m,down}$ the magnon frequency shift occupies the lower of the bistable Δ_m modes and suddenly increases to a higher value upon leaving the bistable range at Eq. 5.4.9. Inserting the values from Eqs. 5.4.8 and 5.4.9 back into Eq. 5.3.16 now allows up to see the δ_m value (and applied field strength, H) at which the limits of the bistable range will occur, relative to the applied driving field strength Ω.

$$(-\delta_{m,up})\left(\alpha^0\omega - \delta_{m,up}\left(\frac{\alpha'\omega}{2K}\right)\right)^2 = \frac{2Kg^2\Omega^2}{(\omega_c-\omega)^2+(\omega\beta)^2} \tag{5.4.10}$$

$$\left(-\frac{1}{3}\delta_{m,down}\right)\left(\frac{4}{9}\delta_{m,down}^2 + \left(\alpha^0\omega - \frac{1}{3}\left(\frac{\alpha'\omega}{2K}\right)\delta_{m,down}\right)^2\right) = \frac{2Kg^2\Omega^2}{(\omega_c-\omega)^2+(\omega\beta)^2} \tag{5.4.11}$$

where $\delta_{m,up}$ and $\delta_{m,down}$ are the δ_m values corresponding to the foldover limits described by Eqs. 5.4.8 and 5.4.9, respectively.

We begin by looking at the foldover limit at $\delta_{m,up}$ given by Eq. 5.4.10. Here we see that since in general both α^0 and α' will be small relative to δ_m, the relation between Ω and $\delta_{m,up}$ will be highly dependent on the magnitude of $\delta_{m,up}$ relative to these damping terms. For the case of small δ_m, corresponding to low amplitude magnon oscillations and low input power, we can approximate $\alpha^0\omega \gg \delta_{m,up}\left(\frac{\alpha'\omega}{2K}\right)$. This simplifies Eq. 5.4.10 to:

$$\delta_{m,up} \approx -\left(\frac{1}{\alpha^0\omega}\right)^2 \frac{2Kg^2\Omega^2}{(\omega_c-\omega)^2+(\omega\beta)^2} \tag{5.4.12}$$

As input power and magnon oscillation amplitude increases the magnitude of δ_m will also increase. Eventually at high input powers we will have $\alpha^0\omega \ll \delta_{m,up}\left(\frac{\alpha'\omega}{2K}\right)$, simplifying Eq. 5.4.10 to:

$$\delta_{m,up} \approx -\left(\frac{2K}{\alpha'\omega}\right)^{2/3}\left(\frac{2Kg^2\Omega^2}{(\omega_c-\omega)^2+(\omega\beta)^2}\right)^{1/3} \tag{5.4.13}$$

Turning our attention the the foldover limit at $\delta_{m,down}$ given by Eq. 5.4.11 we again note that $\delta_m \gg \alpha^0\omega$ except at very low input powers. Thus we can simplify Eq. 5.4.11 to:

$$\delta_{m,down} \approx -\left(\frac{27}{4+\left(\frac{\alpha'\omega}{2K}\right)^2}\right)^{1/3}\left(\frac{2Kg^2\Omega^2}{(\omega_c-\omega)^2+(\omega\beta)^2}\right)^{1/3} \tag{5.4.14}$$

The above relations between δ_m and Ω at the foldover limits show that the upper and lower boundaries can have very different relations to the power input into the coupled CMP system. To make this relation clearer we can insert the total input power, $P_d = \Omega^2/S^2$, into Eqs. 5.4.12, 5.4.13, and 5.4.14, where S is a parameter relating the input power to the driving force acting on the CMP system, and is dependent on the cavity design and input microwave frequency. We thus find:

$$
\begin{aligned}
\delta_{m,up} &\propto P_d && \text{(at low powers)} \\
\delta_{m,up} &\propto P_d^{1/3} && \text{(at high powers)} \\
\delta_{m,down} &\propto P_d^{1/3} && \text{(at all non-linear powers)}
\end{aligned}
\tag{5.4.15}
$$

These dependencies are exactly the same as those seen in uncoupled anharmonic oscillator systems (such as FM resonance) and are typical of results produced by a non-linear restoring force. Referring to Eq. 5.4.3 for the relation between δ_m and the magnon resonance frequency ω_m, we find that the same power relations hold. Thus when varying ω_m using an externally applied static field, we will find that the external fields at which the foldover limits occur will follow the above power relations.

5.5 Experimental Set-up

To study non-linearity in CMP coupling, we designed a system consisting of a microwave waveguide cavity coupled to a small sample of Yttrium Iron Garnet (YIG). The microwave cavity is based on a Fabry-Perot design, shown in Fig. 5.1, consisting of circular waveguides connected through circular-to-rectangular transitions to coaxial-rectangular adapters. In this type of cavity the circular and rectangular waveguides can be rotated relative to each other at the transition points to control the reflection of microwave signals at each transition port and change the off-resonance transmission through the cavity system[196]; for our experiments the rotation between the waveguides was set at 45^o to maximize microwave transmission through the cavity at off-resonance frequencies. This Fabry-Perot cavity design allows high microwave energies to be transferred to the magnon subsystem over a wide range of frequencies, permitting non-linear foldover effects to be seen both near and far from cavity resonance modes. This is in contrast to the typical 3-dimensional cavities used in the other experiments in this dissertation, where strong microwave fields are only present in the CMP system near cavity resonance frequencies.

The YIG sample coupled to the cavity during our measurements was a polished single crystal sphere, of 1 mm diameter. As in our previous experiments, YIG was chosen as the magnetic material for coupling to the cavity due to its properties as an electrical insulator and its relatively low damping compared to other FM materials. We see from Eq. 5.4.7 that the driving microwave power needed to produce foldover in a

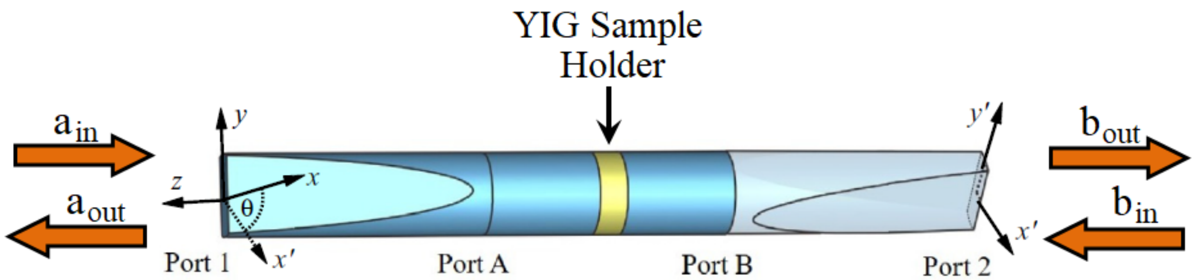

Figure 5.1: A diagram of the Fabry-Perot-type cavity used in our non-linear CMP measurements, displaying how the S_{21} microwave transmission through the system is measured. Microwave signals are sent into, and detected from the cavity resonator, while the dynamics of the FM resonator can be detected through its coupling effects on the field dispersion within the cavity. S_{21} is measured as b_{out}/a_{in} for $b_{in} = 0$.

ferromagnet is proportional to the cube of the material's damping constant, thus a low damping material is essential to achieving large foldover effects in our CMP system. During measurements the YIG sphere was placed at the centre of the mid-plane of the cavity, halfway along the length of waveguide, held in place by a thin plastic sample holder. This point is expected to have a maximum microwave field amplitude (directed along the length of the cavity), and was chosen so as to achieve maximum coupling between the cavity and YIG systems. The YIG was excited to ferromagnetic resonance through the use of an externally applied static magnetic field, H, applied perpendicular to the length of the cavity and along the [110] axis of the YIG's crystalline axis. The crystaline axes of our sample were set during during production of the sample, and marked by small dots on the sample to allow axis dependent measurements to be performed. When resonating about this axis the non-linear Kerr constant is expected to have a negative amplitude[195].

Due to the different cavity design used in this CMP system, the transmission coefficient, S_{21}, will be different from those in the previous experiments. Since in our Fabry-Perot-type waveguide microwave transmission is maximized away from the cavity resonance frequency and is minimized at the resonance frequency where the cavity absorbs microwave energy, the input/output equations for this type of cavity will be:

$$a_{in} - b_{out} = \sqrt{\Gamma}A \tag{5.5.1}$$

$$b_{in} - a_{out} = \sqrt{\Gamma}A \tag{5.5.2}$$

Here we assume that only the cavity system is being driven by the applied microwave field, and that the YIG subsystem is excited to resonance only through its coupling with the cavity. In this cavity system the field sent into the system, Γ, will be equal to the driving force required to produce resonant equilibrium and counteract damping forces (Ω in Eq. 5.3.1) plus an additional force representing the effects of extrinsic coupling forces at the input/output ports of the cavity (Ω_{ex}); thus $\Gamma = \Omega + \Omega_{ex}$. Combined with the previously calculated equations of motion for the CMP system in Eqs. 5.3.10 and 5.3.11, the above input/output equations allow us to calculate the S_{21} transmission coefficient for our coupled CMP system:

$$\begin{aligned} S_{21} &= \frac{b_{out}}{a_{in}}|_{b_{in}=0} \\ &= 1 - \frac{\Gamma}{i(\omega_c - \omega) + \omega\beta + \dfrac{g^2}{i(\omega_m + \Delta_m - \omega) + \omega\left(\alpha + \dfrac{\alpha'\Delta_m}{2K}\right)}} \end{aligned} \tag{5.5.3}$$

Before proceeding to high power measurements, we first characterize the individual subsystems of our coupled CMP system at low input powers. The cavity resonance mode we chose to excite during coupling was the h-mode with a resonance frequency at $\omega_c/2\pi = 12.082$ GHz. Measuring the damping of this cavity mode by fitting Eq. 5.5.3 to a frequency dispersion measurement taken far from coupling (where effects from coupling to the magnon system are almost zero) we can determine $\beta = 8.4 \times 10^{-3}$ and $\Gamma/2\pi = 99$ MHz. Measuring the YIG resonance far from this cavity mode, we see that its resonance frequency follows the Kittel mode dispersion described by $\omega_m/2\pi = \gamma(H_r + H_a)$, where $\gamma/2\pi = 26.9\mu_0$ GHz/T is the gyromagnetic ratio of the YIG, $\mu_0 H_a = 10.4$ mT is the anisotropy field of the spherical sample, and H_r is the strength of the applied static magnetic field needed to achieve resonance. The linear Gilbert damping constant of the YIG sample was determined at ω_m far from ω_c to be $\alpha = 1.1 \times 10^{-5}$. Knowing these values, we then tune the externally applied static field to $\mu_0 H = 438.8$ mT, which corresponds to $\omega_m = \omega_c$ as seen in Fig. 5.2(b). In this region of strong CMP coupling we can now fit Eq. 5.5.3 to the measured dispersion to determine the coupling strength between the cavity and YIG subsystems, finding $g/2\pi = 18.0$ MHz. With both the cavity and YIG subsystems now characterized, we are now able to accurately reproduce the measured S_{21} transmission values both far from CMP coupling [Fig. 5.2(c)] and during CMP coupling [Fig. 5.2(d)].

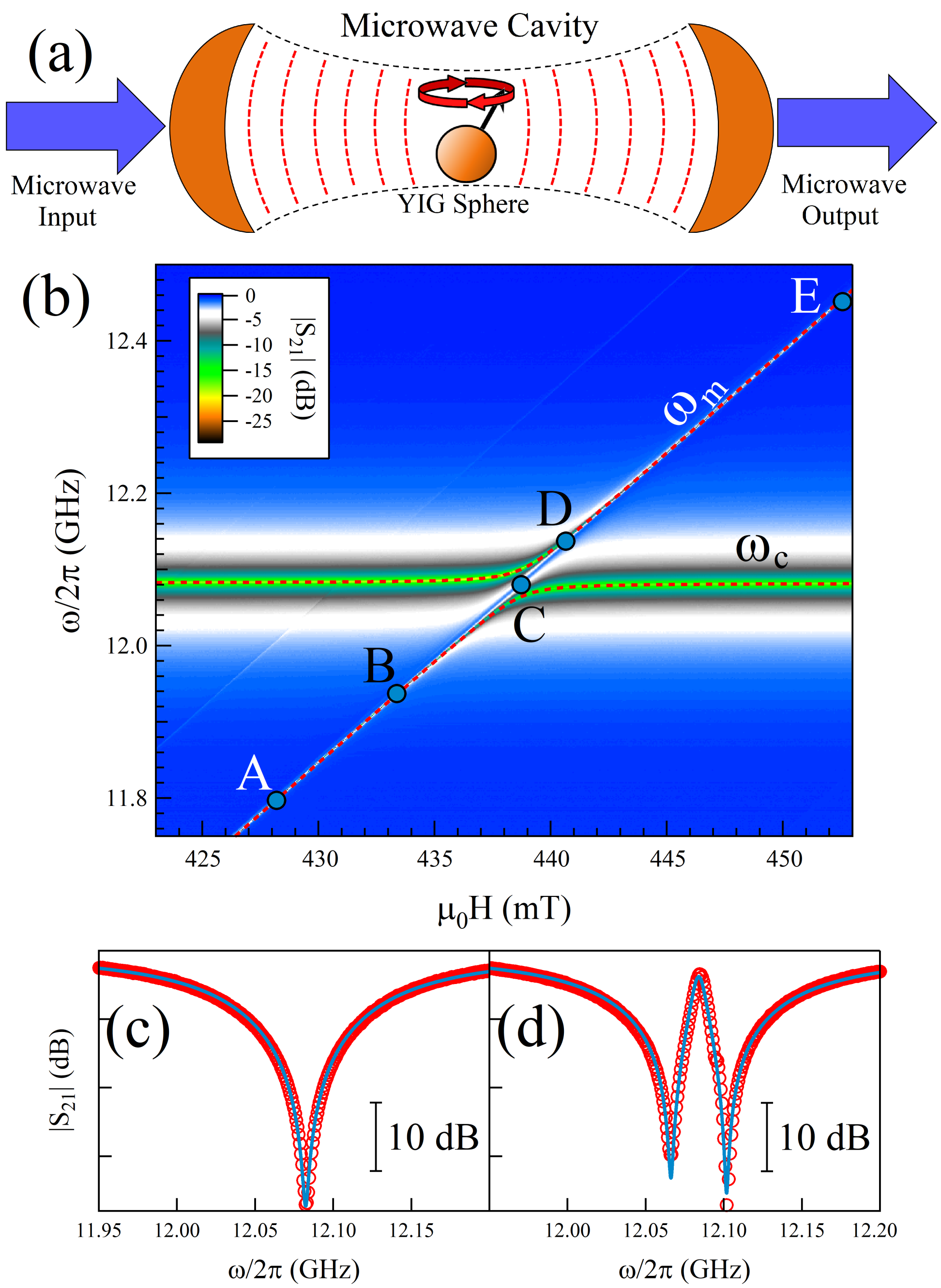

Figure 5.2: **(a)** A schematic diagram of the experimental setup, with a YIG sphere placed in the mid-plane of a waveguide cavity and a static magnetic field applied along the YIG's [110] crystal plane. **(b)** A plot of microwave transmission through our coupled CMP system, displaying level repulsion near coupling. The dashed lines indicate the CMP dispersion calculated by the model in Eq. 5.5.3 for $\Delta_m = 0$. **(c)** Fixed field transmission measurements cut from (b) measured far below coupling fields and **(d)** where $\omega_m = \omega_c$. The solid lines in (c) and (d) fit these dispersions to the model in Eq. 5.5.3.

5.6 H Field Sweeps

Having characterized our coupled CMP system, we can now study the non-linear dynamics of the system during coupling. This was done by sending high power microwave signals into the waveguide cavity using a microwave generator to excite resonance in the CMP system, then measuring the transmission signal through the CMP using a signal analyser. To first get a picture of what the linear transmission spectra of the CMP system look like we inject very low power microwave fields, with $P_d = 0.1$ mW, into the system. This low power microwave signal is still able to generate resonance within the CMP system, but is not strong enough to excite the magnon subsystem to amplitudes where non-linear effects would become significant. This allows us to fit these low input power transmission lineshapes by setting $\Delta_m = 0$ in Eq. 5.5.3.

The transmission measurements we perform involve sweeping the strength of the static magnetic field, H, which is applied to the CMP system. This has the effect of shifting the resonance frequency of the magnon subsystem through the relation $\omega_m/2\pi = \gamma(H + H_a)$, so that when the applied microwave frequency matches this ω_m a magnon resonance signal will be observed. In doing these sweeps we will see only a single transmission peak at the magnon resonance frequency, which will be shifted due to coupling and non-linear damping effects, due to the fact that only the magnon subsystem of our CMP is susceptible to changes in H. The cavity subsystem during these sweeps thus acts as a resonant background system which the magnon system couples to when ω_m is near ω_c, though the cavity resonance can be still play an important role in determining the transmission lineshape seen in H sweeps due to coupling effects between the two CMP subsystems.

The impact of coupling to the cavity subsystem can be seen when comparing transmission lineshapes at microwave frequencies far from ω_c to strongly coupled CMP lineshapes near $\omega_m = \omega_c$. In Fig. 5.3 we measure the transmission spectra of the CMP system at microwave frequencies of $\omega/2\pi = 12.450$ GHz, $\omega/2\pi = 12.082$ GHz, and $\omega/2\pi = 11.800$ GHz; respectively corresponding to the positions labelled E, C, and A in Fig. 5.2. Positions E and A are far from the resonant mode of the cavity, thus we see their lineshape matches the lorentzian dip expected for an uncoupled FM resonator in a Fabry-Perot type cavity[196], with high transmission away from H_r and low transmission near H_r where the YIG sample absorbs the microwave signals. Conversely at position C, which is at the cavity resonance frequency, we see that the lineshape is reversed to form a lorentzian peak due to coupling with the cavity system. Here there is low microwave transmission far from H_r, where the signal is absorbed by the cavity resonator, and high transmission near H_r, due to coupling effects shifting the resonance modes of the system away from ω_c at this field. Fitting the low input power transmission signals in Fig. 5.3 we determine the input driving force necessary to achieve stable resonance at microwave frequencies $\omega = 12.450$ GHz, $\omega = 12.082$ GHz, and $\omega = 11.800$ to be $\Gamma/2\pi = 180$ MHz, 89 MHz, and 175 MHz, respectively. The higher driving fields necessary to achieve stable resonance at frequencies farther from ω_c is an expected result of lower transfer efficiency of energy between the cavity and magnon subsystems at these frequencies.

Increasing the microwave power supplied to the CMP system, we can observe the resonance frequency of the coupled system to gradually shift to higher H fields. The shift, Δ_m, is positive due to the fact that the Kerr term, K, is negative for a YIG sphere magnetized along its [110] crystal axis. At sufficiently high microwave powers we begin to see that Up Sweeps (towards higher H fields) and Down Sweeps (towards lower H fields) begin to produce different S_{21} transmission spectra. In both of these sweep types we begin to notice that these differences occur over an H field range preceding a sudden discontinuity in the transmission spectra. These sudden discontinuities correspond to the $\delta_{m,up}$ and $\delta_{m,down}$ jump points analysed in Eqs. 5.4.12, 5.4.13, and 5.4.14, and the range of H values over which Up and Down H field sweeps differ represents the range of foldover for a CMP system driven to non-linear amplitudes. The two transmission values for each H field in the respective Up and Down sweeps thus represent the two stable resonance states of the non-linear CMP system within the bistable foldover range, with the sudden discontinuities representing the end of the bistable range and a return to parameters in which the CMP has only a single resonance state.

In Fig. 5.3 we show transmission spectra taken at high microwave input powers, where foldover effects have become clearly visible. The spectra shown were taken at the same microwave frequencies as the low power measurements ($\omega/2\pi = 12.450$ GHz, 12.082 GHz, and 11.800 GHz), but at microwave input powers high enough to produce considerable foldover effects; the input powers shown correspond to $P_d = 200$ mW, 400 mW, and 200 mW for the three frequencies plotted. The reason higher input powers are required to produce similar foldover ranges for frequencies nearer to ω_c is due to increased damping felt by the magnon sub-system produced through its extrinsic coupling to the cavity at these frequencies. In these plots we can clearly see the S_{21} transmission differences between the H field Up and Down sweeps within the bistable foldover ranges and the abrupt S_{21} jumps which occur at the limits of these ranges. These transmission spectra are fitted to Eq. 5.5.3 using the same parameters as were used to fit the low power spectra, now using non-zero Δ_m values corresponding to $KS^2 = 5.77 \times 10^{-8}$ GHz^3/mW, 1.58×10^{-8} GHz^3/mW, and

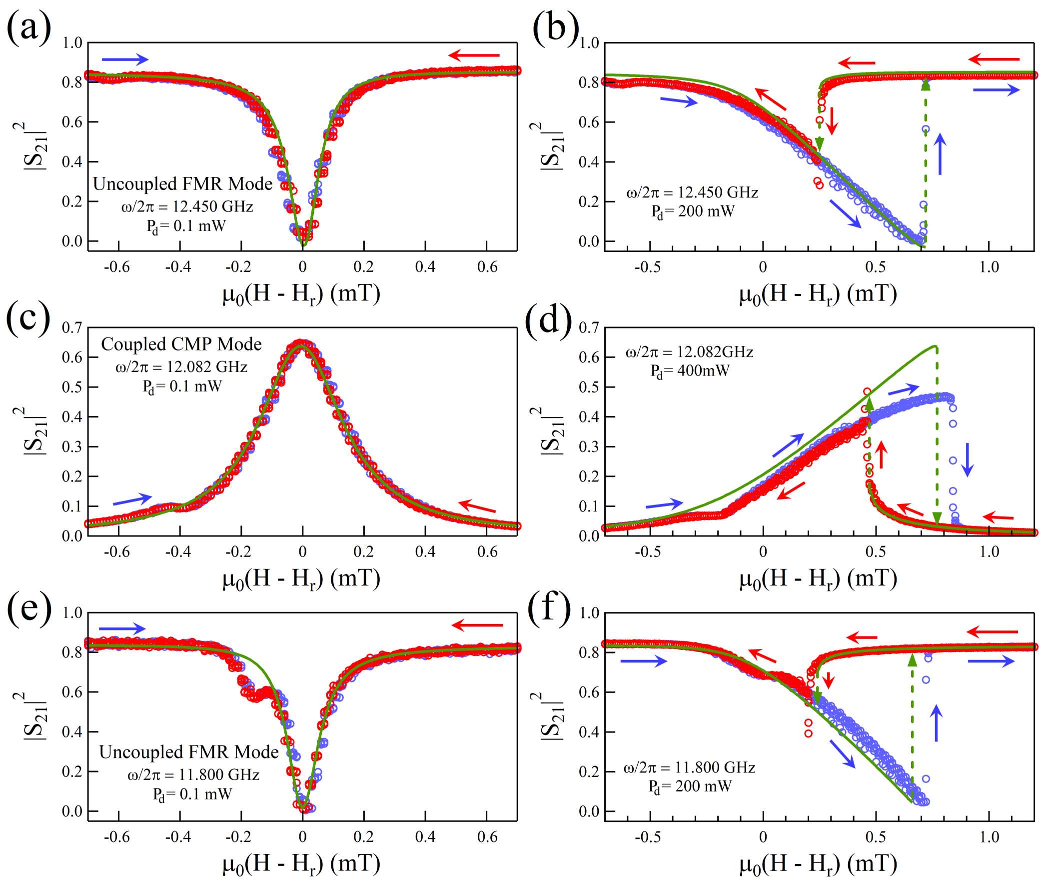

Figure 5.3: **(a)** A plot of the $|S_{21}|^2$ transmission signal of the uncoupled YIG FMR mode, measured at a microwave frequency far above ω_c ($\omega/2\pi = 12.450$ GHz) and at a low microwave input power of $P_d = 0.1$ mW. **(b)** A plot of the measured $|S_{21}|^2$ transmission at $\omega/2\pi = 12.450$ GHz and a high input power of $P_d = 200$ mW. **(c)** A plot of the measured $|S_{21}|^2$ transmission of our CMP system during coupling with $\omega_m = \omega_c$ ($\omega = 12.082$ GHz) at a low microwave input power of $P_d = 0.1$ mW. **(d)** A plot of $|S_{21}|^2$ measured at $\omega/2\pi = 12.082$ GHz for a high input power of $P_d = 400$ mW. **(e)** A plot of the $|S_{21}|^2$ transmission of the uncoupled YIG FMR mode measured at a microwave frequency far below ω_c ($\omega/2\pi = 11.800$ GHz) and at a low input power of $P_d = 0.1$ mW. **(f)** A plot of the measured $|S_{21}|^2$ at $\omega/2\pi = 11.800$ GHz for a high input power of $P_d = 200$ mW. In the low power plot of (a), (c), and (e) the paths of the H field up sweeps (blue symbols) and the H field down sweeps (red symbols) are seen to be equal. For the high power measurements in (b), (d), and (f) non-linear effects become significant and the up and down H field sweeps are no longer equal, with sudden $|S_{21}|^2$ jumps appearing at fields above H_r. The solid green lines in these plots represent H field up and down sweeps calculated using the model in Eq. 5.5.3, with the dashed portions indicating H field jump positions.

3.75×10^{-8} GHz^3/mW for $\omega = 12.450$ GHz, 12.082 GHz, and 11.800 GHz respectively. Where Δ_m is determined by solutions to Eq. 5.3.16 and KS is the Kerr constant multiplied by the parameter relating input microwave power to the CMP driving force ($P_d = \Gamma^2/S^2$). Due to the presence of S, a frequency dependent power conversion coefficient, we cannot determine the exact value of the Kerr coefficient in our

YIG sample, but we can still observe its effects in the bistable foldover range.

Notable in the plots shown in Fig. 5.3 is the change in the bistable range produced by ω being near ω_c. Far from ω_c we see that in the H field Up sweep the S_{21} transmission has a minimum value which shifts to higher fields as power is increased, until at the field corresponding to $\delta_{m,up}$ the transmission suddenly increases; in the Down sweep at these frequencies the transmission remains relatively high in the bistable region, until suddenly decreasing at $\delta_{m,down}$. At frequencies very near ω_c this behaviour is reversed, with Up sweeps having relatively low transmission in the bistable range before suddenly increasing at $\delta_{m,up}$ and Down sweeps rising to high transmissions before dropping at $\delta_{m,down}$. These differences represent the main impact of the cavity resonance modes when coupled to non-linear FM resonance in the form of CMP systems; by changing the transmission lineshape of the CMP, as seen in the low power plots shown in Fig. 5.3, the foldover behaviour of the CMP system is changed. H field Up sweeps transform from sudden transmission increases at $\delta_{m,up}$ (similar to uncoupled non-linear FM systems) to sudden transmission decreases at this point for frequencies near ω_c where coupling effects are strong, with the reverse happening to the jumps at $\delta_{m,down}$.

At intermediate frequencies between those very far from and very near to ω_c additional lineshape fea-

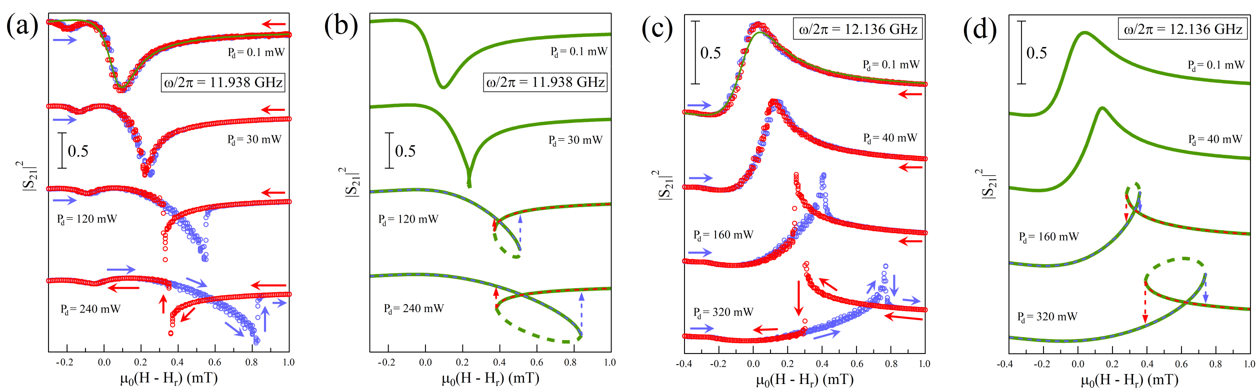

Figure 5.4: **(a)** A plot showing the $|S_{21}|^2$ transmission signals of our CMP system at $\omega/2\pi = 11.938$ GHz, showing how non-linear effects become apparent as input power is increased from $P_d = 0.1$ mW to $P_d = 240$ mW. Here the H field up sweeps are plotted as blue symbols and the H field down sweeps are plotted as red symbols. **(b)** Modelled results for the measured $|S_{21}|^2$ transmissions plotted in (a), using Eq. 5.5.3. **(c)** A plot showing the $|S_{21}|^2$ transmission signal at $\omega/2\pi = 12.136$ GHz, as input power is increased from $P_d = 0.1$ mW to $P_d = 320$ mW. H field up sweeps are plotted as blue symbols and H field down sweeps are plotted as red symbols. **(d)** Modelled results for the measured $|S_{21}|_2$ transmissions plotted in (c), using Eq. 5.5.3. In the plots of (b) and (c) the modelled paths of up and down sweeps are shown as blue and red dashed lines. The dashed green portions of the modelled curves in these plots represent unstable CMP resonant modes which cannot be measured in our system.

tures can be seen in observed S_{21} transmission spectra. In Fig. 5.4 we show measurements taken at intermediate frequencies above ω_c at $\omega/2\pi = 12.136$ GHz, and below ω_c at $\omega/2\pi = 11.938$ GHz, corresponding to the positions marked as D and B in Fig. 5.2. Focussing first on the low power ($P_d = 0.1$ mW) spectra we see a marked change in lineshape as compared to the low power measurements shown in Fig. 5.3. The lineshapes obtained during H field sweeps at these intermediate frequencies can be seen in Fig. 5.4 to be mainly asymmetric; these lineshapes are produced by coupling between the cavity and magnon subsystems within the CMP as the spectra changes from a negative Lorentzian lineshape at frequencies far from ω_c to a positive Lorentzian lineshape at ω_c. The low power spectra at these intermediate frequencies can again be reproduced by Eq. 5.5.3 for $\Delta_m = 0$, with $\Gamma/2\pi = 47$ MHz for $\omega/2\pi = 12.136$ GHz and $\Gamma/2\pi = 107$ MHz for $\omega/2\pi = 11.938$ GHz, as shown in Fig. 5.4.

As the microwave power input into the CMP system is increased at these intermediate frequencies we again see a gradual shift in their resonance features towards higher H fields. At a certain threshold power we again begin to see differences between the H field Up and Down sweeps, indicating the presence of foldover bistabilities in the CMP system. However, the characteristics of this foldover are seen to be quite different than for the previous cases. Instead of the resonance signal gradually folding over itself to produce a range containing two stable modes and one unstable mode, with each mode having a unique transmission, the foldover at intermediate frequencies produces a transmission loop within the foldover range; this loop is clearly shown in the modelled S_{21} dispersions shown in Fig. 5.4. Within this loop there are still two stable resonance modes and one unstable mode, but notably there exists a point where the two stable modes cross one another and have equal transmissions. These high power measurements at intermediate frequencies can again be fit using Eq. 5.5.3 using the same parameters as in the low power sweeps, with the values of $KS = 1.95 \times 10^{-8}$ GHz^3/mW and $KS = 2.3 \times 10^{-8}$ GHz^3/mW for $\omega/2\pi = 12.136$ GHz and $\omega/2\pi = 11.938$ GHz respectively determined based on the H field positions of the transmission jumps.

The behaviour of these transmission jumps are seen to also be changed due to the different foldover characteristics of the CMP system at these intermediate frequencies. While in the foldover lineshapes near to and far from ω_c the two jumps at the edges of the bistable range are in opposite directions (one from high to low transmission, the other from low to high transmission), at the intermediate frequencies shown in Fig. 5.4 both transmission jumps are in the same direction. This produces a unique butterfly-like hysteresis feature that has not previously been recorded in studies of either magnetic or coupled magnon-cavity systems. Notably, the polarity of the transmission jumps at intermediate frequencies is reversed when the input microwave frequency is changed from $\omega > \omega_c$ to $\omega < \omega_c$. Although the general butterfly-like hysteresis remains, we can see in Fig. 5.4 that at $\omega/2\pi = 12.136$ GHz ($> \omega_c$) both jumps are towards higher S_{21} transmissions, while at $\omega/2\pi = 11.938$ GHz ($< \omega_c$) the jumps are towards lower transmissions. This polarity change in the transmission jumps is a result of changes to the dispersive lineshape of the CMP system, which reverses sign due to coupling effects between the cavity and magnon subsystems around ω_c.

Measuring the H field positions of observed S_{21} transmission jumps in our H field sweeps, we can compare the change in these values relative to applied microwave power, P_d, to those predicted in Eqs. 5.4.12, 5.4.13, and 5.4.14. Due to the ω dependent nature of the relation between input microwave power,

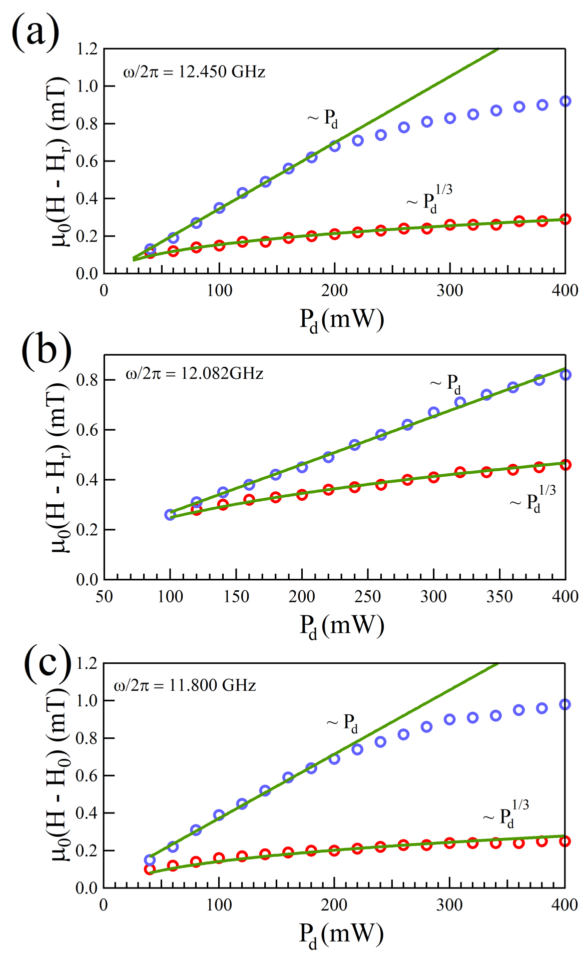

Figure 5.5: Plots of the measured H field up sweep jump positions $\delta_{m,up}$ (blue symbols) and H field down sweep jump positions $\delta_{m,down}$ (red symbols), at input microwave frequencies of **(a)** $\omega/2\pi = 12.450$ GHz, **(b)** $\omega/2\pi = 12.082$ GHz, and **(c)** $\omega/2\pi = 11.800$ GHz. These relation of these jump positions to the applied microwave power, P_d, are compared to that predicted by Eqs. 5.4.12, 5.4.13, and 5.4.14 (green curves). The discrepancy between the modelled and measured $\delta_{m,up}$ jump positions at high input powers in (a) and (c) is expected to be a result of higher order non-linear effects.

P_d, and the driving field felt by the CMP system, Γ, ($P_d = \Gamma^2/S^2$) we cannot determine the value of the Kerr constant K from these fittings. We can however still determine a value for KS^2, which combines the Kerr constant with the constant relating P_d and Γ, using this value to determine the magnon resonance shift, Δ_m, when comparing S_{21} measurement data to Eq. 5.5.3. In Fig. 5.5 we compare the measured S_{21} jump positions for frequencies near to and far from ω_c to the low power rates of change relative to P_d, with $\delta_{m,up}$ expected to have a linear dependence to P_d and $\delta_{m,down}$ expected to have a dependence relative to $P_d^{1/3}$. We find good agreement between the measured and expected rates of change as P_d is increased, and from the low power fittings determine $KS^2 = 5.77 \times 10^{-8}$ GHz^3/mW at $\omega = 12.450$ GHz, $KS^2 = 1.58 \times 10^{-8}$ GHz^3/mW at $\omega = 12.082$ GHz, and $KS^2 = 3.75 \times 10^{-8}$ GHz^3/mW at $\omega = 11.800$ GHz. At higher input microwave powers (< 200 mW) we begin to see significant deviations from the linear P_d relation described by 5.4.12 for $\delta_{m,up}$. This is expected from our model, as at high powers the linear P_d relation gradually shifts to the $P_d^{1/3}$ relation described by Eq. 5.4.13. The reason this deviation only occurs at frequencies far from ω_c is due to the increased extrinsic damping experienced by the magnon subsystem due to its coupling to the cavity subsystem at frequencies near ω_c; this increases the input power necessary to achieve foldover.

Because the butterfly-like hysteresis features observed in our CMP system are a product of resonance lineshape, it is expected that they are not limited to this kind of system. In uncoupled magnon systems similar dispersive lineshapes can be obtained for resonance measurements performed using electrical detection measurements or by manipulating the phase of the of the microwave signal relative to the oscillation of the magnon[200]. By exciting magnon systems in these conditions to high amplitude oscillations, so that non-linear damping effects become significant, it is expected that the butterfly-like bistability features seen in our CMP system at intermediate frequencies should become visible. Additionally, since the dispersive lineshape of Fano-like resonant systems is a general wave phenomenon, we expect that butterfly-like bistability features should not be limited to magnon-based systems, but should be observable across many areas of physics and engineering involving resonant systems.

5.7 Constant Field Power Sweeps

In addition to performing H field sweeps on our non-linear CMP system at a constant input microwave power, P_d, we can also perform sweeps at a constant H field where P_d is swept toward increasing or decreasing values. In the H sweeps discussed in the previous section, the resonance signals are formed when the changing H field shifts the magnon subsystem's resonance frequency to match that of the input microwave signal. This allows us to observe the magnon subsystem being shifted to higher amplitude resonance states, and eventually to bistable foldover states. Alternatively, in sweeping P_d the characteristics of the magnon subsystem are unchanged during coupling to the cavity subsystem; the only change experienced in the CMP system is the dynamic response of the coupled magnon system to the input microwave signal as microwave power is either increased or decreased.

In performing a P_d sweep we first choose to set the static H field on the system to a value where large S_{21} variations are expected to occur as P_d is changed. Looking back to our H field sweep measurements in Figs. 5.3 and 5.4 and focussing on the transmission at a single field value at different P_d values, we see that the largest changes in S_{21} will occur at fields above the low power magnon resonance frequency (for our $K < 0$ system), where $H > H_r$. As the coupled magnon resonance peak is shifted to higher fields due to non-linear damping effects the measured S_{21} at these fields will increase as the shifted resonance signal moves towards a specific H field, reach a maximum when the shifted resonance is equal to H, then again decrease as the resonance peak moves to higher H values. If the selected H field is above the value of $\delta_{m,thresh}$, the minimum resonance shift required to produce foldover effects, then we will expect to see the effects of foldover in our P_d sweeps due to the presence of bistable resonance modes at H for at least some P_d values.

In Fig. 5.6 P_d sweeps are presented for the same frequencies whose resonance lineshapes were measured via H sweeps in the previous section, namely $\omega/2\pi = 12.450$ GHz, 12.136 GHz, 12.082 GHz, 11.938 GHz, and 11.800 GHz. The respective H fields these sweeps were taken at, $\mu_0 H = 452.70$ mT, 441.08 mT, 439.02 mT, 433.67 mT, and 428.54 mT, were selected as fields above the lower limit of foldover bistability defined by $\delta_{m,thresh}$ in Eq. 5.4.5 but still low enough to be below both the $\delta_{m,up}$ and $\delta_{m,down}$ jump positions at the maximum P_d available to our microwave generator ($\sim$ 500 mW). By choosing H fields within this range we are able to see the effects of the S_{21} jumps at the upper and lower limits of the foldover range as they pass through our chosen field with either increasing or decreasing P_d.

Observing the P_d sweeps in Fig. 5.6, the first thing we notice is the similarity between these dispersions and the corresponding H field dispersions plotted in Figs. 5.3 and 5.4 at the same ω. Far from ω_c at $\omega/2\pi = 12.450$ GHz and 11.800 GHz the S_{21} transmission is relatively high at very high and very low P_d values, decreasing at intermediate values as the resonance signal is shifted through the static H values selected at these frequencies. Near ω_c at $\omega/2\pi = 12.082$ GHz the reverse is true, with S_{21} increasing at intermediate P_d values where the resonance peak is shifted through the selected H field. At the intermediate frequencies $\omega/2\pi = 12.136$ GHz and 11.938 GHz the measured Up and Down P_d sweeps are seen to cross each other and produce butterfly-like dispersion curves, very similar to those observed in the H field sweeps of Fig. 5.4. From these similarities, we can deduce that the dispersion lineshapes produced by P_d sweeps are highly dependent on the shape of the H field dispersions observed at the same frequency.

The main difference between H field and P_d sweep dispersions are the positions of the S_{21} jumps occurring at the edges of the bistable range. When comparing the jumps at frequencies near to and far from ω_c it is clear that the positions of the jumps to higher S_{21} and the jumps to lower S_{21} values appear to switch positions in the P_d sweeps as compared to the H field sweeps. If we follow the S_{21} values at a constant field in H sweep measurements as P_d is changed the reason for this switch becomes clear. Beginning at a low input power P_d and an H field just above the critical threshold field where foldover appears (defined in Eq. 5.4.5), the measured S_{21} transmission will (for ω far from ω_c) remain high as the coupled magnon resonance peak begins to shift to higher H. When foldover begins the S_{21} at our static H field will now

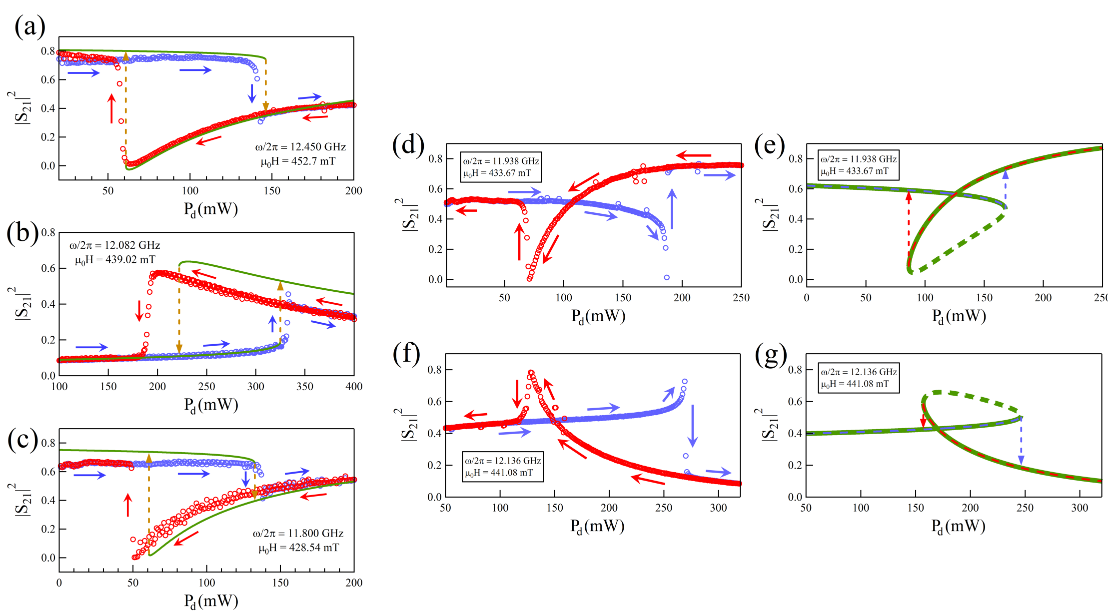

Figure 5.6: Plots of $|S_{21}|^2$ transmission measurements taken by sweeping the input microwave power, P_d, up (blue symbols) or down (red symbols) while leaving the applied H field constant. The plotted measurements were taken at microwave frequencies of **(a)** $\omega/2\pi = 12.450$ GHz, **(b)** $\omega/2\pi = 12.082$ GHz, **(c)** $\omega/2\pi = 11.800$ GHz, **(d)** $\omega/2\pi = 11.938$ GHz, and **(f)** $\omega/2\pi = 12.136$ GHz. The green curves in (a), (b), and (c) are modelled results for the measured systems, produced using the model in Eq. 5.5.3. For $\omega/2\pi = 11.938$ GHz and $\omega/2\pi = 12.136$ GHz, these modelled $|S_{21}|^2$ plots are shown in **(e)** and **(g)** respectively, where the unstable resonant mode of the CMP system is shown as the dashed portion of the green curves.

have two bistable solutions, a high transmission one and a lower transmission one.

In an H field Up sweep we would measure beginning from behind the resonance peak at high S_{21}, moving along the resonance signal towards lower S_{21} values until encountering the jump at $\delta_{m,up}$ and suddenly returning to high S_{21} values. Because this H field Up sweep follows the folded over resonance peak, the lower S_{21} values would be measured within the bistable foldover range. This is in contrast to a P_d Up sweep where as foldover begins the measured S_{21} transmission, which at low powers will be high, will remain high as the shifted resonance peak folds over it. In this P_d Up sweep the higher S_{21} values would be measured within the bistable range, encountering the sudden transmission jump at $\delta_{m,down}$ as the bistable foldover range is eventually shifted past the static H field being measured. For H and P_d Down sweeps the reverse happens, with H sweeps remaining at high transmissions before experiencing a sudden jump at $\delta_{m,down}$ and P_d measurements beginning on the crest of the folded over resonance signal, moving to lower transmissions as the resonance peak passes through the selected H value, then experiencing a jump to higher transmission at $\delta_{m,up}$. Thus the Up and Down sweeps of H field and P_d appear as mirror images of each other, as can be seen from comparing the sweeps shown in Figs. 5.3 and 5.6. The same reversal of sweep behaviour is true for ω values near ω_c and for intermediate frequencies, with the folded over resonance peak and butterfly-like resonance signals measured in H sweeps being mirrored in P_d sweeps.

5.8 CMP Hysteresis Loop Evolution

In Fig. 5.7 we summarize the foldover behaviour of the coupled CMP system as the input microwave frequency is shifted through ω_c. In this plot we show the CMP resonance modes as green lines, plotted relative to the uncoupled magnon resonance mode H field, H_r, and the uncoupled cavity resonance mode frequency, ω_c. The solid black line indicates the low H field limit of foldover, at any fields below this value no foldover effects can be observed. This value is determined by;

$$H = H_r + \frac{1}{\gamma}\left(-(\pm)\sqrt{3}\left(\alpha\omega + \frac{g^2\omega\beta}{(\omega_c-\omega)^2+(\omega\beta)^2}\right) - \frac{g^2(\omega_c-\omega)}{(\omega_c-\omega)^2+(\omega\beta)^2}\right) \tag{5.8.1}$$

Here the sign of the $\pm$ is determined by the sign of the Kerr constant of the material coupled to the cavity system, in our measurements and in Fig. 5.7 $K < 0$ and thus the $-$ sign is taken. As the input microwave frequency approaches ω_c the effects of CMP coupling on foldover become apparent, with the foldover lineshape changing significantly from its uncoupled state and the lower H field foldover limit moving away

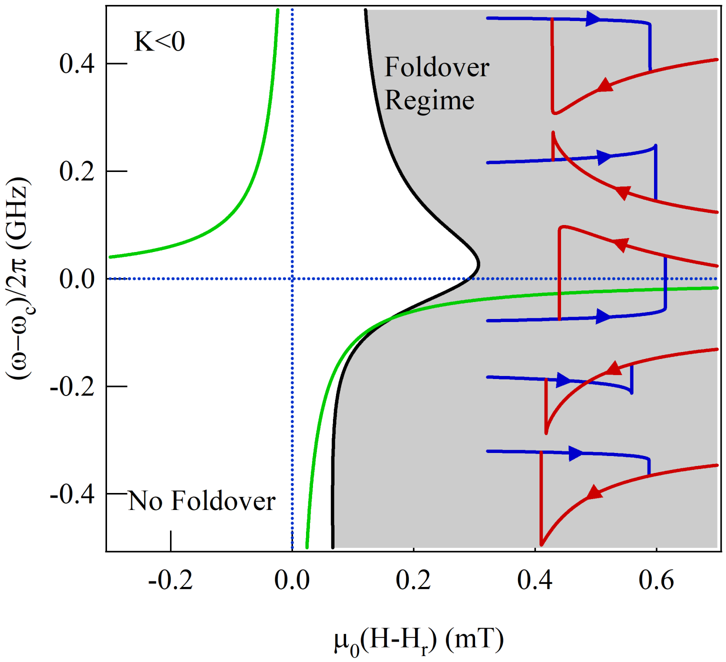

Figure 5.7: A 'Phase diagram' of CMP power hysteresis loops for a negative Kerr term, where the grey region indicates where CMP bistabilities are observed. Within this region distinct bistable behaviours are observed: termed clockwise, butterfly-like, or counterclockwise. As the measured frequency of the system is increased from far above to far below ω_c the bistable lineshapes will evolve, as indicated by the modelled plots in this grey region. Arrows in these plots indicate the sweeping direction of the microwave power. The green curves indicate the positions of the coupled CMP modes in this system.

from H_r. This shift in the foldover limit is a result of coupling effects between the cavity and magnon subsystems increasing the damping forces felt by the magnon subsystem at frequencies near $\omega = \omega_c$.

In contrast to previous studies of uncoupled magnon systems[77][190] and coupled CMP systems[195], we find that by coupling a resonant magnon system to a cavity resonator allows several forms of bistable behaviour to be produced; with the type of behaviour strongly dependent on the strength of coupling between the cavity and magnon systems. These same foldover behaviours are expected to be produced for a CMP system having $K < 0$, but in this case magnon resonance shift will be towards fields below H_r, resulting in the foldover H field limit and foldover lineshape behaviour being mirrored about the ω_c and H_r axes.

5.9 Summary

In summary, we have both theoretically and experimentally studied the effects of non-linear magnon resonance behaviour in a coupled CMP system. Using a specially designed Fabry-Perot-like cavity resonator, we excite the Kittel mode of a YIG sphere to amplitudes where non-linear Kerr effects become significant. When coupled to a resonant mode of the cavity system, these non-linear effects produce bistability effects unlike those seen previously in uncoupled magnon systems. By adjusting the frequency of the magnon system relative to that of the cavity mode, we are able to tune our CMP system through a range of these bistable lineshapes, producing clockwise, butterfly-like, or counterclockwise hysteresis loops in the transmission spectrum of the CMP system. These bistable hysteresis loops appear in both H field and input power sweeps, with the lineshapes produced by both sweep types closely corresponding. Developing a model for non-linear behaviour in CMP systems through the addition of a non-linear Kerr term to the coupled CMP Hamiltonian, we are able to accurately reproduce the bistable hysteresis loops observed in our measurements. This model also allows us to calculate the limits of the bistable regions in our CMP system, with the calculated power dependence of these limits agreeing with both our measurements and power dependencies previously reported for uncoupled magnon systems. Because bistable systems are a key component of many current data storage and processing systems, we expect that non-linear CMP systems similar to ours (which combine coherent magnon-photon coupling with the ability to tune the relative energies of bistable states) could play a key role in the development of future computing technologies. Further, because the method used to produce our non-linear CMP model is not limited to non-linear magnon behaviour, and because the Fano-like resonance lineshapes produced in our CMP system are a general wave feature, we expect that the non-linear features observed in our system should be reproducible across many other areas of physics and engineering.

Chapter 6

Conclusions

As a recently developed field, the study of coupling between photons and magnons has advanced rapidly over the past few years. The discovery that magnon-polaritons (MPs) can be created as hybridized quasi-particles combining the properties of both photon and magnon excitations has further fuelled advancement by presenting the possibility that these particles could combine the data storage capabilities of magnetic systems with the data carrying capacity of photons in new communications and data processing systems. Although magnon-photon interactions have formed the basis for magnetic resonance studies for many decades, only recently have techniques been developed to directly study the nature of the coupling between them. This has historically been due to the relatively low coupling strengths between individual photons and magnetic spins, as well as the short coherence time of coupling interactions between them. Predictions that collective excitations of certain magnetic materials could form macrospin states, behaving as a single spin system while increasing magnon-photon coupling strengths by several orders of magnitude, revolutionized the study of MPs by suggesting that their quantum properties could be observed even in macroscopic magnon systems. Combined with mature microwave cavity excitation techniques already developed for magnetic resonance studies, these predictions allowed continuous magnon-photon interactions to be studied as cavity magnon-polaritons (CMPs), a new sub-field of MP quasi-particles.

Representing a new method to investigate magnon-photon interactions, the study of CMP systems has quickly progressed from its theoretical origins. In 2014, when I began my PhD research, only a few studies had demonstrated strong coupling in CMP systems at room temperature. Today, only a few years later, these systems are now the subject of nearly 100 publications per year, in influential journals such as Physics Review Letters, Nature, and Science. During the development of the field, research on CMP systems has also led to the creation of entirely new areas of research, such as the field of cavity spintronics. Combining the manipulation of spin polarization through magnetic and non-magnetic materials (spintronics) with magnon excitations produced through CMP coupling, the field of cavity spintronics has worked to harness the quantum coherence demonstrated in CMP systems to produce spin currents (currents where spin polarization is transported as opposed to electric charge) able to carry quantum information. Although still in the early stages of development, future cavity spintronic systems present the possibility for converting photon signals directly into information carried by the polarization of a spin current. As opposed to present systems, where information carried by photons is converted to magnetic bits only after being converted into an electric charge current, cavity spintronic systems could produce data processing technologies with a much reduced size and power consumption (by eliminating the Joule heating effects associated with electric currents) while allowing for the transport and storage of quantum information required by quantum computing systems.

Although CMP systems show significant promise for use in future information technologies, the relative immaturity of the field means that much work remains to be done in learning how to control and apply the effects of coupling in these systems. Towards this end, the ability of CMP coupling to help form a bridge between multiple resonant photon systems was demonstrated in Chap. 3. Previous publications have shown that multiple resonant magnetic systems can exchange energy when both coupled to the same cavity mode excitation. The obvious next step in developing a method in which coupled CMP systems could be used for data processing would be to link multiple cavity photon excitations together by coupling them each to a single magnon excitation. Here difficulties in producing cavity resonators with mode frequencies near enough to be able to simultaneously couple to another system were overcome with the development of a high-Q cavity with an adjustable height. This allowed us to achieve indirect coupling between two orthogonal cavity resonance modes via their simultaneous CMP coupling to a magnon mode in a YIG sphere. Studying this indirect coupling, we found that its strength can be controlled through tuning the resonance frequencies of the component subsystems relative to each other. The dynamics of indirect coupling were also found to be highly dependent on the relative oscillation phases of the two cavity systems, with energy transfer being either enhanced or suppressed when the cavity modes were in-phase or out-of-phase with each other, respectively. By experimentally showing that CMP systems can be used to indirectly couple both photon and magnon resonant systems together, the work demonstrated in this chapter reveals the possibility for similar systems to couple large numbers of photon and magnon excitations together simultaneously, a goal which would represent substantial progress towards a quantum based computing and telecommunications system.

CMP systems are significant in their ability to use magnetic macrospin states and confined cavity systems to create sustained coherent coupling between magnon and photon resonance states, but other systems have also been developed to study light-matter interactions. These include phonon -polariton systems, which couple infrared photons to material lattice oscillations, and exciton-polaritons, which couple optical photons to electron hole or quantum well excitations. In these other polariton systems light-matter coupling has been shown to produce a visible frequency gap, known as the polariton gap, where no stable coupled modes can occur. However, despite similar light-matter interactions being present in these polariton systems and cavity MP systems, no polariton gap was previously reported in CMP systems. In Chap. 4 we investigate the connection between light-matter coupling in cavity MP and other polariton systems, developing a new model to describe how differences between the systems leads to different frequency dispersions. This model relates the two systems through the effective permeability the input photons experience; in CMP systems (where photons travel through both the cavity and material volumes) the effective permeability will be the average of both the material and cavity systems. Since most microwave cavities are designed to have an unchanging permeability during coupling, the magnetic material permeability changes that occur during magnon-photon coupling will appear significantly reduced when averaged with the cavity system to produce an effective permeability. The effective permeability model we develop thus not only accounts for the much reduced polariton gap in CMP systems, but also provides a single simple model which can describe polariton coupling in all systems involving light-matter interactions. We further demonstrate that the height adjustable cavity developed for previous measurements can be used to measure the polariton gap in CMP systems, with the measured gap agreeing with that expected from our effective permeability model. The work in this chapter thus conclusively shows that light-mater interactions in all coupled polariton systems are equivalent, and demonstrates that changing the effective permeability of a CMP system through relative volume changes could represent a method for controlling the coupled dispersions of these systems.

Much of modern information storage is dependent on magnetic bistabilities, with the hysteresis states of magnetic bits being used to store information in binary form. In 2009 a new form of magnetic bistability was discovered in resonant systems[77], where non-linear damping effects can cause resonant transmission peaks to fold-over themselves so that multiple stable resonant states are possible for the same magnetic configuration. In Chap. 5 we studied how non-linear Kerr effects in magnetic systems can be used to produce bistable foldover states in CMP systems, and how the behaviour of these bistabilites can be controlled through tuning the CMP system. Although the non-linear effects were only present in the magnon subsystem, the coupled resonance states of the CMP system (which involve both magnon and photon dynamics) were able exhibit foldover behaviour and produce bistable modes. Beyond the simple foldover behaviour of uncoupled magnetic systems, the foldover behaviour in CMP systems was found to be extremely variable. The resonant energies of the bistable modes in CMP systems can be adjusted relative to each other, and even reversed (high energy modes becoming low energy modes), as the state of the coupled CMP system is changed. The behaviour of the CMP bistable modes in CMP systems is accurately described by a model combining non-linear resonant dynamics in magnon systems with a quantum description of CMP coupling. This model additionally allows us to calculate the limits of foldover behaviour in CMP systems and how tuning the driving frequency, input power, or applied field can affect the relative energies of the bistable CMP modes. In addition to showing that non-linear magnetic bistabilites can be produced in coupled CMP systems and how their tunable states could be used to extend the data storage and processing capabilities of these systems, the non-linear model we use to describe them is not limited to CMP systems and is generally applicable for non-linear behaviours in other coherently coupled systems. Thus the myriad array of foldover behaviours seen in our measurements may be reproducible across many areas of physics and engineering.

In addition to the studies discussed in detail in this dissertation, I have had the opportunity to contribute to several other works exploring the dynamic properties of coupled CMP systems. One of these works[180] studied the relative phase properties of coupled CMP systems, which is seen to vary substantially as different coupled resonance states are reached by the system. Of particular note in this study was the observation of an antiresonance mode corresponding to the dynamic properties of the uncoupled magnon system. In this antiresonance state the magnon dynamics are uncoupled from those of the cavity system, similar to the dynamics of magnon dark modes explored in other studies[24] which have been proposed for use as long-term coherent data storage technologies. The exploration of CMP phase dynamics near these antiresonance modes, and other coupled CMP modes, allows an enhanced understanding of the evolution of these systems near these states which can be extended to other examples of coupled systems. Another work I participated in[201] examined the topological properties of CMP systems near the boundary between weak and strong coupled states. By controlling the coupling strength of a CMP system an exceptional point was found, at which both the eigenfrequencies and eigenvectors of the coupled modes were equal. Near this exceptional point careful tuning of the CMP system permits switching between different resonant modes, revealing new applications for CMP systems in data processing systems. Understanding coupled dynamics near this exceptional point could allow for the engineering of topological structures in CMP systems to create additional stable resonance states and further the exploration of non-Hermitian dynamics in coupled systems. A further work I contributed to during my doctoral studies[43] used spintronic-based measurements to directly observe magnon dynamics during CMP coupling. By inserting multiple magnon systems into a single resonant cavity, we demonstrated that spin systems could be electrically manipulated by each other over distances much greater than the spin diffusion length through mutual coupling to the cavity mode. By combining the coupling properties of CMP systems with spintronic measurement techniques, this work contributed to the development of a new research field, cavity spintronics.

The research performed during my PhD studies has led to a greater understanding of the dynamics of coupling in CMP systems and has produced several new methods for utilizing and controlling these systems, yet there remains much new physics waiting to be explored in them. The coupling studies presented in this dissertation have all been of coherently coupled photon-magnon systems, but recently a new form of coupling between magnon and photon excitations has been observed[152]. In this new coupling, termed dissipative coupling, the coupling forces exerted on each system are out-of-phase with their general resonant motion, such that coupling effects act to damp the resonant energies in the coupled systems. This is opposed to the effects of coherent coupling, where coupling effects act in-phase with resonant motion and help to drive resonant motion. Although the physical background of dissipative coupling remains unclear, its effects can clearly be seen as changes to the coupled CMP mode dispersion and lineshape. The fact that dissipative coupling can be achieved in coherently coupled CMP systems by simply changing the position of the magnon system relative to the cavity excitation fields, in addition to the fact that it has recently been demonstrated in planar CMP systems, reveal that studying this form of coupling may lead to a much greater understanding of the dynamics of CMP systems and permit an entirely new range of possible applications. The development of feedback-coupled cavities[202], which exhibit Q factors far in excess of normal cavity systems through external amplification of the resonant signal, promise to allow far greater coupling strengths in CMP systems and permit further exploration of the non-linear regime of coupling discussed in this dissertation. The planar design of these feedback-coupled cavities and the new coupling dynamics they may allow should further accelerate the development of new applications for CMP systems in information processing technologies.

In combining the quantum nature of magnon-photon interactions with macroscopic cavity and magnon systems, coupled CMP systems permit a unique view of the physics underlying these interactions while providing the ability to harness these interactions in near-future applications. The near exponential increase in publications related to CMP systems over the past few years serves to highlight how these systems have advanced our understanding of magnon-photon interactions, while the combination of CMP systems with spintronic techniques to control and utilize magnon excitations has produced an entirely new sub-field of spintronic research. In the relatively new field of CMP studies, the models developed and the observations made of CMP systems in this dissertation have helped to lay the foundation of the field, and will pave the way for future theoretical and experimental development. With the recent intermingling of CMP systems with other cutting-edge developments producing new fields of study such as cavity spintronics, cavity quantum electrodynamics[203] and cavity optomechanics[204][205], it is certain that CMP systems have the potential to reveal much more to future research.

Bibliography

[1] C. P. Poole, H. A. Farach, R. J. Creswick, and R. Prozorov, *Superconductivity* (Academic Press, 2007)

[2] P. Busch, P. Lahti, and R.F. Werner, *Proof of Heisenberg's Error-Disturbance Relation*, Physical Review Letters. **111**, 160405 (2013) arXiv:1306.1565

[3] A. Aspect, P. Grangier, and G. Roger, *Experimental Realization of Einstein-Podolsky-Rosen-Bohm Gedankenexperiment: A New Violation of Bell's Inequalities*, Physical Review Letters. **49** (2): 91-94 (1982)

[4] Y. Tokura, M. Kawasaki, and N. Nagaosa, Nat. Phys. **13**, 1056 (2017)

[5] P. W. Anderson, Science **177**, 393 (1972)

[6] R. B. Laughlin, *A Different Universe: Reinventing Physics From The Bottom Down* (Basic Books, 2005)

[7] J.M.D. Coey, *Magnetism and Magnetic Materials* (Cambridge University Press, Cambridge, 2010)

[8] V. K. Arkad'yev, J. Russ. Phys.-Chem. Soc. **44**, 165 (1912)

[9] J.H.E. Griffiths, Nature **158**, 670 (1946)

[10] B. Lax and K. J. Button, *Microwave Ferrites and Ferrimagnetics* (McGraw-Hill, 1962)

[11] B. Hillebrands and K. Ounadjela, *Spin Dynamics in Confined Magnetic Structures I*, Topics in Applied Physics (Springer, 2002)

[12] L.D. Landau and E.M. Lifshitz, *Theory of the dispersion of magnetic permeability in ferromagnetic bodies*, Phys. Z. Sowjetunion. **8**, 153

[13] T.L. Gilbert, *A Lagrangian formulation of the gyromagnetic equation of the magnetic field*, Physical Review. **100** (4): 1243 (1955)

[14] M. Harder, Y. Gui, and C.-M. Hu, Phys. Rep. **661**, 1 (2016), arXiv:1605.00710

[15] Richard P. Feynman, Robert Leighton, and Matthew Sands, *The Feynman Lectures on Physics*, Vol. 2. Addison-Wesley. pp. Ch. 37. (1963)

[16] F. Bloch, *Zur Theorie des Ferromagnetismus*, Zeitschrift für Physik, **61** (3-4): 206-219 (1930)

[17] M. Plihal, D.L. Mills, and J. Kirschner, *Spin wave signature in the spin polarized electron energy loss spectrum in ultrathin Fe film: theory and experiment*, Phys. Rev. Lett. **82**: 2579-2582. (1999)

[18] N. Bloembergen and R. Pound, Phys. Rev. **203**, 1949 (1954)

[19] C.-M. Hu, Phys. Canada **72**, 76 (2016), arXiv:1508.01966.

[20] Ö. O. Soykal and M. E. Flattè, Phys. Rev. Lett. **104**, 077202 (2010) arXiv:0907.3926

[21] Ö. O. Soykal and M. E. Flattè, Phys. Rev. B **82**, 104413 (2010), arXiv:1005.3068

[22] H. Huebl, C.W. Zollitsch, J. Lotze, F. Hocke, M. Greifenstein, A. Marx, R. Gross, and S.T.B. Goennenwein, Phys. Rev. Lett. **111**, 127003 (2013) arXiv:1207.6039

[23] X. Zhang, C.-L. Zou, L. Jiang, and H. X. Tang, Phys. Rev. Lett. **113**, 156401 (2014) arXiv:1405.7062.

[24] Y. Tabuchi, S. Ishino, A. Noguchi, T. Ishikawa, R. Yamazaki, K. Usami, and Y. Nakamura, Science **349**, 405 (2015) arXiv:1410.3781.

[25] M. Harder, L. Bai, C. Match, J. Sirker, and C. Hu, Sci. China Physics, Mech. Astron. **59**, 117511 (2016) arXiv:1601.06049v1.

[26] G.B.G. Stenning, G.J. Bowden, L.C. Maple, S.A. Gregory, A. Sposito, R.W. Eason, N.I. Zheludev, and P.A.J. de Groot, Opt. Express **21**, 1456 (2013)

[27] B. Bhoi, T. Cliff, I.S. Maksymov, M. Kostylev, R. Aiyar, N. Venkataramani, S. Prasad, and R.L. Stamps, J. Appl. Phys. **116**, 243906 (2014) arXiv:1409.5499.

[28] S.A. Gregory, G.B.G. Stenning, G.J. Bowden, N.I. Zheludev, and P.A.J. de Groot, New J. Phys. **16**, 063002 (2014)

[29] S. Kaur, B. Yao, Y.-S. Gui, and C.-M. Hu, J. Phys. D. Appl. Phys. **49**, 475103 (2016) arXiv:1507.06940.

[30] D. Zhang, W. Song, and G. Chai, J. Phys. D. Appl. Phys. **50**, 205003 (2017)

[31] H. Maier-Flaig, M. Harder, S. Klingler, Z. Qiu, E. Saitoh, M. Weiler, S. Geprägs, R. Gross, S.T.B. Goennenwein, and H. Huebl, Appl. Phys. Lett. **110**, 132401 (2017) arXiv:1701.08969.

[32] M. Goryachev, S. Watt, J. Bourhill, M. Kostylev, and M. E. Tobar, Phys. Rev. B **97**, 155129 (2017) arXiv:1711.09980.

[33] L. V. Abdurakhimov, S. Khan, N. A. Panjwani, J. D. Breeze, S. Seki, Y. Tokura, J.J.L. Morton, and H. Kurebayashi, (2018), arXiv:1802.07113

[34] M. Goryachev, W.G. Farr, D.L. Creedon, Y. Fan, M. Kostylev, and M.E. Tobar, Phys. Rev. Appl. **2**, 054002 (2014) arXiv:1408.2905

[35] X. Zhang, C.-L. Zou, L. Jiang, and H.X. Tang, Phys. Rev. Lett. **113**, 156401 (2014) arXiv:1405.7062.

[36] J. Bourhill, N. Kostylev, M. Goryachev, D.L. Creedon, and M.E. Tobar, Phys. Rev. B **93**, 144420 (2016) arXiv:1512.07773v2

[37] H. Maier-Flaig, M. Harder, R. Gross, H. Huebl, and S.T.B. Goennenwein, Phys. Rev. B **94**, 054433 (2016) arXiv:1601.05681.

[38] N.J. Lambert, J.A. Haigh, and A.J. Ferguson, J. Appl. Phys. **117**, 053910 (2015) arXiv:1506.02902.

[39] X. Zhang, C. Zou, L. Jiang, and H.X. Tang, J. Appl. Phys. **119**, 023905 (2016)

[40] M. Goryachev, M. Kostylev, and M.E. Tobar, (2017), arXiv:1710.06601.

[41] Y. Tabuchi, S. Ishino, A. Noguchi, T. Ishikawa, R. Yamazaki, K. Usami, and Y. Nakamura, Comptes Rendus Phys. **17**, 729 (2016) arXiv:1508.05290

[42] P. Hyde, L. Bai, M. Harder, C. Match, and C.-M. Hu, Appl. Phys. Lett. **109**, 152405 (2016) arXiv:1606.03469.

[43] L. Bai, M. Harder, P. Hyde, Z. Zhang, C.-M. Hu, Y. P. Chen, and J. Q. Xiao, Phys. Rev. Lett. **118**, 217201 (2017) arXiv:1706.00347.

[44] N.J. Lambert, J.A. Haigh, S. Langenfeld, A.C. Doherty, and A.J. Ferguson, Phys. Rev. A **93**, 021803 (2016) arXiv:1506.06049v2

[45] X. Zhang, C.-L. Zou, N. Zhu, F. Marquardt, L. Jiang, and H.X. Tang, Nat. Commun. **6**, 8914 (2015) arXiv:1507.02791v1

[46] A. Morin, C. Lacroix, and D. Menard, in 2016 17th Int. Symp. Antenna Technol. Appl. Electromagn., Vol. **114** (IEEE, 2016) pp. 1-2.

[47] L. Bai, M. Harder, Y.P. Chen, X. Fan, J.Q. Xiao, and C.-M. Hu, Phys. Rev. Lett. **114**, 227201 (2015) arXiv:1504.01335.

[48] M. Harder, L. Bai, P. Hyde, and C.-M. Hu, Phys. Rev. B **95**, 214411 (2017) arXiv:1702.04797

[49] D. Zhang, X.-Q. Luo, Y.-P. Wang, T.-F. Li, and J.Q. You, Nat. Commun. **8**, 1368 (2017)

[50] Y.-P. Wang, G.-Q. Zhang, D. Zhang, X.-Q. Luo, W. Xiong, S.-P. Wang, T.-F. Li, C.-M. Hu, and J.Q. You, Phys. Rev. B **94**, 224410 (2016) arXiv:1609.07891.

[51] Y.-P. Wang, G.-Q. Zhang, D. Zhang, T.-F. Li, C.-M. Hu, and J. Q. You, Phys. Rev. Lett. **120**, 057202 (2018) arXiv:1707.06509

[52] S. Kaur, B.M. Yao, J.W. Rao, Y.S. Gui, and C.-M. Hu, Appl. Phys. Lett. **109**, 032404 (2016)

[53] Z. Tay, W. Soh, and C. Ong, J. Magn. Magn. Mater. **451**, 235 (2018)

[54] R. Hisatomi, A. Osada, Y. Tabuchi, T. Ishikawa, A. Noguchi, R. Yamazaki, K. Usami, and Y. Nakamura, Phys. Rev. B **93**, 174427 (2016) arXiv:1601.03908

[55] B.M. Yao, Y.S. Gui, J.W. Rao, S.Kaur, X.S. Chen, W. Lu, Y. Xiao, H. Guo, K.P. Marzlin, and C.-M. Hu, Nat. Commun. **8**, 1437 (2017)

[56] P. Hyde, B.M. Yao, Y.S. Gui, Guo-Qiang Zhang, J.Q. You, and C.-M. Hu, Physical Review B **98**, 174423 (2018)

[57] Paul Hyde, Lihui Bai, Michael Harder, Christopher Dyck, and Can-Ming Hu, Physical Review B **95**, 094416 (2017)

[58] Simon Haykin, *Communication Systems* (4th ed.), John Wiley & Sons, pp. 1-3 (2001)

[59] William Stallings, *Data and Computer Communications* (7th edition), Pearson Prentice Hall (2004)

[60] David A. Patterson and John L. Hennessy, *Computer Organization and Design: The Hardware/Software Interface* (3rd ed.), Amsterdam: Morgan Kaufmann Publishers (2005)

[61] V.K. Arkad'yev, J. Russ. Phys.-Chem. Soc. **44**, 165 (1912)

[62] Y.S. Gui, N. Mecking, X. Zhou, G. Williams, and C.-M. Hu, Phys. Rev. Lett. **98**, 107602 (2007)

[63] M.N. Baibich, J.M. Broto, A. Fert, F.N. Van Dau, and F. Petroff, Phys. Rev. Lett. **61**, 2472 (1988)

[64] A. Brataas, Y. Tserkovnyak, G.E.W. Bauer, and B.I. Halperin, Phys. Rev. B. **66**, 060404(R) (2002)

[65] Alfred Landé, *Uber den anomalen Zeemaneffekt*, Zeitschrift für Physik **5**, 231 (1921)

[66] B. Hillebrands and K. Ounadjela, *Spin Dynamics in Confined Magnetic Structures I, Topics in Applied Physics*, Springer, (2002)

[67] F. Bloch, *Nuclear Induction*, Phys. Rev. **70**, 460 (1946)

[68] T. Gilbert, *A Phenomenological Theory of Damping in Ferromagnetic Materials*, IEEE Trans. Magn. **40**, 3443 (2004)

[69] J.H.E. Griffiths, *Anomalous high-frequency resistance of ferromagnetic metals*, Nature **158**, 4019 (1946)

[70] E. Zavoisky, *Spin magnetic resonance in the decimeter-wave region*, Fizicheskiĭ Zhurnal. **10** (1946)

[71] M.C. Hickey and J.S. Moodera, *Origin of Intrinsic Gilbert Damping*, Phys. Rev. Lett. **102**, 137601 (2009)

[72] B.A. Calhoun, J. Overmeyer, and W.V Smith, *Ferrimagnetic Resonance in Gadolinium Iron Garnet*, Physical Review **107**, 993 (1957)

[73] H. Maier-Flaig, M. Harder, S. Klingler, Z. Qiu, E. Saitoh, M. Weiler, S. Geprägs, R. Gross, S.T.B. Goennenwein and H. Huebl, *Tunable magnon-photon coupling in a compensating ferrimagnet - from weak to strong coupling*, Appl. Phys. Lett. **110**, 132401 (2017)

[74] M.S. Soda and N.C. Srivastava, *Microwave Propagation in Ferrimagnets*, Springer (1981)

[75] D. Polder, *On the theory of ferromagnetic resonance*, The London, Edinburgh, and Dublin Philosophical Magazine and Journal of Science **40** (1949)

[76] C. Kittel, *On the theory of ferromagnetic resonance absorption*, Phys. Rev. **73**, 155 (1948)

[77] Y.S. Gui, A. Wirthmann, N. Mecking, and C.-M. Hu, *Direct measurement of nonlinear ferromagnetic damping via the intrinsic foldover effect*, Phys. Rev. B **80**, 060402(R) (2009)

[78] C. Herring and C. Kittel, *On the theory of spin waves in ferromagnetic media*, Phys. Rev. **81**, 869 (1951)

[79] D.S. Schmool and H. Kachkachi, *Single-Particle Phenomena in Magnetic Nanostructures*, Elsevier (2015)

[80] L.R. Walker, *Magnetostatic modes in ferromagnetic resonance*, Phys. Rev. **105**, 390 (1957)

[81] W.G. Egan and H.J. Juretschke, J. Appl. Phys. **34**, 1477 (1963)

[82] Y.S. Gui, N. Mecking, X. Zhou, Gwyn Williams, and C.-M. Hu, Phys. Rev. Lett. **98**, 107602 (2007)

[83] A. Wirthmann, Xiaolong Fan, Y.S. Gui, K. Martens, G. Williams, J. Dietrich, G.E. Bridges, and C.-M. Hu, *Direct phase probing and mapping via spintronic Michelson interferometry*, Phys. Rev. Lett. **105**, 017202 (2010)

[84] M. Harder, Z.X. Cao, Y.S. Gui, X.L. FAn, and C.-M. Hu, *Analysis of the line shape of electrically detected ferromagnetic resonance*, Phys. Rev. B **84**, 054423 (2011)

[85] E. Saitoh, M. Ueda, H. Miyajima, and G. Tatara, Appl. Phys. Lett. **88**, 182509 (2006)

[86] Y. Kajiwara, K. Harii, S. Takahashi, J. Ohe, K. Uchida, M. Mizuguchi, H. Umezawa, H. Kawai, K. Ando, K. Takanashi, S. Maekawa, and E. Saitoh, Nature **464**, 262 (2010)

[87] T.J. Silva, C.S. Lee, T.M. Crawford, and C.T. Rogers, *Inductive measurement of ultrafast magnetization dynamics in thin-film Permalloy*, J. Appl. Phys. **85**, 7849 (1999)

[88] M. Covington, T.M. Crawford, and G.J. Parker, *Time-resolved measurement of propagating spin waves in ferromagnetic thin films*, Phys. Rev. Lett. **89**, 237202 (2002)

[89] J.P. Park, P. Eames, D.M. Engebretson, J. Berezovsky, and P.A. Crowell, *Spatially resolved dynamics of localized spin-wave modes in ferromagnetic wires*, Phys. Rev. Lett. **89**, 277201 (2002)

[90] S. Neusser, G. Duerr, H.G. Bauer, S. Tacchi, M. Madami, G. Wolsterdorf, G. Gubbiotti, C.H. Back, and D. Grundler, *Anisotropic Propagation and Damping of Spin Waves in a Nonopatterned Antidot Lattice*, Phys. Rev. Lett. **105**, 067208 (2010)

[91] J. Goulon, A. Rogalev, F. Wilhelm, N. Jaouen, C. Goulon-Ginet, and C. Brouder, *X-ray detected ferromagnetic resonance in thin films*, Eur. Phys. J. B **53**, 169 (2006)

[92] D. Backes, F. Macià, S. Bonetti, R. Kukreja, H. Ohldag, and A.D. Kent, *Direct Observation of a Localized Magnetic Soliton in a Spin-Transfer Nanocontact*, Phys. Rev. Lett. **115**, 127205 (2015)

[93] S.O. Demokritov, B. Hillebrands, and A.N. Slavin, *Brillouin Light Scattering Studies of of Confined Spin Waves: Linear and Nonlinear Confinement*, Phys. Rep. **348**, 441 (2001)

[94] T. Sebastion, K. Schultheiss, B. Obry, B. Hillebrands, and H. Schultheiss, *Micro-focused Brillouin light scattering: imaging spin waves at the nanoscale*, Front. Phys. **3**, 1 (2015)

[95] J. Podbielski, F. Giesen, and D. Grundler, *Spin-Wave Interference in Microscopic Rings*, Phys. Rev. Lett. **96**, 167207 (2006)

[96] A. Yamaguchi, K. Motoi, H. Miyajima, and Y. Nakatani, *Magnetic field dependence of rectification radio frequency current flowing through a single layered ferromagnetic wire*, J. Appl. Phys. **105**, 07D301 (2009)

[97] Y.S. Gui, N. Mecking, and C.-M. Hu, *Quantized spin excitations in a ferromagnetic microstrip from microwave photovoltage measurements*, Phys. Rev. Lett. **98**, 217603 (2007)

[98] R.H. Dicke, Phys. Rev. **93**, 99 (1954)

[99] D. Schuster, A. Sears, E. Ginossar, L. DiCarlo, L. Frunzio, J. Morton, H. Wu, G. Briggs, B. Buckley, D. Awschalom, *et al.*, Phys. Rev. Lett. **105**, 140501 (2010)

[100] J.-M. LeFloch, N. Delhote, M. Aubourg, V. Madrangeas, D. Cros, S. Castelletto, and M.E. Tobar, Journal of Applied Physics **119**, 153901 (2016)

[101] F. Brennecke, T. Donner, S. Ritter, T. Bourdel, M Köhl, and T. Esslinger, Nature **450**, 268-271 (2007)

[102] Y. Colombe, T. Steinmetz, G. Dubois, F. Linke, D. Hunger, and J. Reichel, Nature **450**, 272-276 (2007)

[103] G. Morigi, J. Eschner, and C.H. Keitel, *Ground State Laser Cooling Using Electromagnetically Induced Transparency*, Phys. Rev. Lett. **85**, 4458 (2000)

[104] A.H. Safavi-Naeini, *et al.*, *Electromagnetically induced transparency and slow light with optomechanics*, Nature **472** 7341 69-73 (2011)

[105] P. Lodahl, A.F. van Driel, I.S. Nikolaev, A. Irman, K. Overgaag, D. Vanmaekelbergh, and W.L. Vos, *Controlling the dynamics of spontaneous emission from quantum dots by photonic crystals*, Nature, **430**, 654 (2004)

[106] X. Wang, *Metallic Spintronic Devices*, CRC Press (2014)

[107] Photograph by Krizu, distributed under a Creative Commons Attribution-Share Alike 3.0 Unported licence

[108] X.F. Zhang, C.-L. Zou, L. Jiang, H.X. Tang, J. Appl. Phys. **119**, 023905 (2016)

[109] Y. Cao, P. Yan, H. Huebl, S.T.B. Goennenwein, and G.E.W. Bauer, Phys. Rev. B **91**, 094423 (2015)

[110] A.A. Serga, A.V. Chumak, and B. Hillebrands, *YIG Magnonics*, J. Phys. D: Appl. Phys. **43** 264002 (2010)

[111] Vladimir Cherepanov, Igor Kolokolov, and Victor L'vov, *The saga of YIG: Spectra, thermodynamics, interaction and relaxation of magnons in a complex magnet*, Physics Reports, Volume 229, Issue 3, pp 81-144 (1993)

[112] M. Gilleo and S. Geller, Phys. Rev. **110**, 73 (1958)

[113] Y. Kajiwara, K. Harii, S. Takahashi, J. Ohe, K. Uchida, M. Mizuguchi, H. Umezawa, H. Kawai, K. Ando, K. Takanashi, S. Maekawa, and E. Saitoh, Nature (London) **464** 262 (2010)

[114] David M. Pozar, *Microwave Engineering*, Fourth Edition (Wiley, New York, 2012)

[115] S.-W. Wong, S.-F. Feng, L. Zhu, and Q.-X. Chu, *Triple and Quadruple-Mode Wideband Bandpass Filter Using Simple Perturbation in Single Metal Cavity*, IEEE Trans. Microw. Theory and Techniques **63**, 10 (2015)

[116] David J. Griffiths, *Introduction to Electrodynamics* (4th ed.), Prentice Hall (2013)

[117] J.D. Jackson, *Classical Electrodynamics*, 3rd edition (Wiley, New York, 1998)

[118] R.E. Collin, *Foundations for Microwave Engineering*, 2nd edition, IEEE Press, New York, NY (2001)

[119] X. Zhang, C.-L. Zou, L. Jiang, and H.X. Tang, *Strongly Coupled Magnons and Cavity Microwave Photons*, Phys. Rev. Lett. **113**, 156401 (2014)

[120] M. Goryachev, W.G. Farr, D.L. Creedon, Y. Fan, M. Kostylev, and M.E. Tobar, *High-Cooperativity Cavity QED with Magnons at Microwave Frequencies*, Phys. Rev. Appl. **2**, 054002 (2014)

[121] O. Klein, S. Donovan, M. Dressel, and G. GrÃ¼ner, *Microwave Cavity Perturbation Technique: Part 1: Principles*, International Journal of Infrared and Millimeter Waves **14**, 12 (1993)

[122] M.S. Venkatesh and G.S.V. Raghavan, *An overview of dielectrical properties measuring techniques*, Can. Biosyst. Eng. **47**:7315-7330 (2005)

[123] X. Zhang, C.-L. Zou, L. Jiang, and H.X. Tang, *Strongly Coupled Magnons and Cavity Microwave Photons*, Phys. Rev. Lett. **113**, 156401 (2014)

[124] M. Harder, L.H. Bai, C. Match, J. Sirker and C.-M. Hu, *Study of the cavity-magnon-polariton transmission line shape*, Sci. China Phys. Mech. Astron. **59**, 117511 (2016)

[125] S.I. Kiselev, J.C. Sankey, I.N. Krivorotov, N.C. Emley, R.J. Schoelkopf, R.A. Buhrman, and D.C. Ralph, Nature (London) **425**, 380 (2003)

[126] Lihui Bai, K. Blanchette, M. Harder, Y.P. Chen, X. Fan, J.Q. Xiao, C.-M. Hu, *Control of the Magnon-Photon Coupling*, IEEE Trans. Magn. **52**, 7 (2016)

[127] C.G. Montgomery, Robert H. Dicke, and Edward M. Purcell, *Principles of microwave circuits*, Institution of Electrical Engineers, London, U.K., (1987)

[128] E.L. Albuquerque and M. G. Cottam, *Polaritons in Periodic and Quasiperiodic Structures*, Elsevier (2004)

[129] D. L. Mills and E. Burstein, Reports Prog. Phys. **37**, 817 (1974)

[130] K. Huang, Nature **167**, 779 (1951)

[131] F. Bloch, *Zur Theorie des Ferromagnetismus*, Zeitschrift für Physik (in German) **61**, 206-219 (1930)

[132] L.C. Andreani, *Strong Light Matter Coupling*, edited by A. Auffèves, D. Gerace, M. Richard, S. Portolan, M.d.F. Santos, L.C. Kwek, and C. Miniatura (Word Scientific, 2014) Chap. 2.

[133] W.L. Barnes, A. Dereux, and T.W. Ebbesen, Nature **424**, 824 (2003)

[134] W.L. Barnes, J. Opt. A Pure Appl. Opt. **8**, S87 (2006)

[135] H. Deng, H. Haug, and Y. Yamamoto, Rev. Mod. Phys. **82**, 1489 (2010)

[136] G. Khitrova and H.M. Gibbs, Rev. Mod. Phys. **71**, 1591 (1999)

[137] V. Timofeev and D. Sanvitto, *Exciton Polaritons in Microcavities* (Springer, 2013)

[138] C.H. Henry and J.J. Hopfield, Phys. Rev. Lett. **15**, 964 (1965)

[139] D.F. Walls and G.J. Milburn, *Quantum Optics*, 2nd Ed. (Springer, 2008)

[140] Y.S. Gui, S. Holland, N. Mecking, and C.-M. Hu, *Resonances in Ferromagnetic Gratings Detected by Microwave Photoconductivity*, Phys. Rev. Lett. **95**, 056807 (2005)

[141] M. Sparks, *Ferromagnetic Relaxation Theory* (McGraw Hill, 1964)

[142] E. Jaynes and F. Cummings, Proc. IEEE **51**, 89 (1963)

[143] B.M. Garraway, Philos. Trans. A. Math. Phys. Eng. Sci. **369**, 1137 (2011)

[144] T. Holstein and H. Primakoff, Phys. Rev. **58**, 1098 (1940)

[145] N. Majlis, *The Quantum Theory of Magnetism* (World Scientific, 2000)

[146] Y.-P. Wang, G.-Q. Zhang, D. Zhang, T.-F. Li, C.-M. Hu, and J.Q. You, Phys. Rev. Lett. **120**, 057202 (2018)

[147] K. Kawasaki, *Simple derivations of generalized linear and nonlinear Langevin equations*, J. Phys. A: Math. Nucl. Gen. **6**, 1289 (1973)

[148] L. Bai, M. Harder, Y.P. Chen, X. Fan, J.Q. Xiao, and C.-M. Hu, Phys. Rev. Lett. **114**, 227201 (2015)

[149] L.D. Landau and E.M. Lifshitz, *Mechanics*, 3rd ed. (Elsevier, 1976)

[150] D.F. Walls and G.J. Milburn, *Quantum Optics*, 2nd ed. (Springer, 2008)

[151] A.A. Clerk, M.H. Devoret, S.M. Girvin, F. Marquardt, and R.J. Schoelkopf, Rev. Mod. Phys. **82**, 1155 (2010)

[152] M. Harder, Y. Yang, B.M. Yao, C.H. Yu, J.W. Rao, Y.S. Gui, R.L. Stamps, and C.-M. Hu, *Level Attraction Due to Dissipative Magnon-Photon Coupling*, Phys. Rev. Lett. **121**, 137203 (2018)

[153] P. Chak, S. Pereira, and J.E. Sipe, *Coupled-mode theory for periodic side-coupled microcavity and photonic crystal structures*, Phys. Rev. B **73**, 035105 (2006)

[154] J. Li, R. Yu, C. Ding, and Y. Wu, *PT-symmetry-induced evolution of sharp asymmetric line shapes and high-sensitivity refractive index sensors in a three-cavity array*, Phys. Rev. A **93**, 023814 (2016)

[155] A.M. Armani, R.P. Kulkarni, S.E. Fraser, R.C. Flagan, and K.J. Vahala,*Label-free, single-molecule detection with optical microcavities*, Science **317**, 783 (2007)

[156] J. Zhu, S.K. Ozdemir, Y.F. Xiao, L. Li, L. He, D.R. Chen, and L. Yang, *On-chip single nanoparticle detection and sizing by mode splitting in an ultrahigh-Q microresonator*, Nat. Photonics **4**, 46 (2010)

[157] A. Osada, R. Hisatomi, A. Noguchi, Y. Tabuchi, R. Yamazaki, K. Usami, M. Sadgrove, R. Yalla, M. Nomura, and Y. Nakamura, *Cavity optomagnonics with spin orbit coupled photons*, Phys. Rev. Lett. **166**, 223601 (2016)

[158] Aymeric Delteil, Zhe Sun, Stefan Fält, and Atac Imamoğlu, *Realization of a Cascaded Quantum System: Heralded Absorption of a Single Photon Qubit by a Single-Electron Charged Quantum Dot*, Phys. Rev. Lett. **118**, 177401 (2017)

[159] J.M.D. Coey, *Magnetism and Magnetic Materials* (Cambridge University Press, Cambridge, 2010)

[160] L. Bai, K. Blanchette, M. Harder, Y. Chen, X. Fan, J. Xiao, and C.-M. Hu, *Control of the magnon-photon coupling*, IEEE Trans. Magn. **52**, 1000107 (2016)

[161] J.-M. Le Floch, N. Delhote, M. Aubourg, V. Madrangeas, D. Cros, S. Castelletto, and M.E. Tobar, *Towards achieving strong coupling in three-dimensional-cavity with solid state spin resonance*, J. Appl. Phys. **119**, 153901 (2016)

[162] D.L. Creedon, J.-M. Le Floch, M. Goryachev, W.G. Farr, S. Castelletto, and M.E. Tobar, *Strong coupling between P1 diamond impurity centers and a three-dimensional lumped photonic microwave cavity*, Phys. Rev. B **91**, 140408(R) (2015)

[163] X. Zhang, C.-L. Zou, L. Jiang, and H.X. Tang, *Strongly coupled magnons and cavity microwave photons*, Phys. Rev. Lett. **113**, 156401 (2014)

[164] B. Bhoi, T. Cliff, I.S. Maksymov, M. Kostylev, R. Aiyar, N. Venkataramani, S. Prasad, and R.L. Stamps, *Study of photon-magnon coupling in a YIG-film split-ring resonant system*, J. Appl. Phys. **116**, 243906 (2014)

[165] L.V. Abdurakhimov, Y.M. Bunkov, and D. Konstantinov, *Normal-mode splitting in the coupled system of hybridized nuclear magnons and microwave photons*, Phys. Rev. Lett. **114**, 226402 (2015)

[166] R. Loudon, *The Quantum Theory of Light* (Oxford University Press, Oxford, 2000)

[167] E.L. Albuquerque and M.G. Cottam, *Polaritons in Periodic and Quasiperiodic Structures* (Elsevier, 2004)

[168] D.L. Mills and E. Burstein, Reports Prog. Phys. **37**, 817 (1974)

[169] L.C. Andreani, *Strong Light Matter Coupling*, edited by A. Auffèves, D. Gerace, M. Richard, S. Portolan, M.d.F. Santos, L.C. Kwek, and C. Miniatura (Word Scientific, 2014) Chap. 2.

[170] W.L. Barnes, A. Dereux, and T.W. Ebbesen, Nature **424**, 824 (2003)

[171] K. Huang, Nature **167**, 779 (1951)

[172] C.H. Henry and J.J. Hopfield, Phys. Rev. Lett. **15**, 964 (1965)

[173] J.F. Cochran and B. Heinrich, IEEE Trans. Magn. **16**, 660 (1980)

[174] C. Kittel, *Introduction to Solid State Physics* (John Wiley & Sons, Inc., New York, 1986) 6th ed.

[175] G.G. Robbrecht and J.L. Verhaeghe, Nature (London) **182**, 1080 (1958)

[176] W.A. Yager, Phys. Rev. **75**, 316 (1949)

[177] Y. Cao, P. Yan, H. Huebl, S.T.B. Goennenwein, and G.E.W. Bauer, *Exchange magnon-polaritons in microwave cavities*, Phys. Rev. B **91**, 094423 (2015)

[178] X. Zhang, C.-L. Zou, L. Jiang, and H.X. Tang, *Strongly Coupled Magnons and Cavity Microwave Photons*, Phys. Rev. Lett. **113**, 156401 (2014)

[179] L. Bai, M. Harder, Y.P. Chen, X. Fan, J.Q. Xiao, and C.-M. Hu, *Spin Pumping in Electrodynamically Coupled Magnon-Photon Systems*, Phys. Rev. Lett. **114**, 227201 (2015)

[180] M. Harder, P. Hyde, L. Bai, C.Match, and C.-M. Hu, *Spin dynamical phase and antiresonance in a strongly coupled magnon-photon system*, Phys. Rev. B **94**, 054403 (2016)

[181] L. Bai, K. Blanchette, M. Harder, Y.P. Chen, X. Fan, J.Q. Xiao, and C.-M. Hu, *Control of the Magnon-Photon Coupling*, IEEE Trans. Magn. **52**, 1000107 (2016)

[182] B.M. Yao, Y.S. Gui, Y. Xiao, H. Guo, X.S. Chen, W. Lu, C.L. Chien, and C.-M. Hu, *Theory and experiment on cavity magnon-polariton in the one-dimensional configuration*, Phys. Rev. B **92**, 184407 (2015)

[183] R. Loudon, *The Quantum Theory of Light* (Oxford University Press, Oxford, 2000)

[184] D.I. Schuster, A.P. Sears, E. Ginossar, L. DiCarlo, L. Frunzio, J.J.L. Morton, H. Wu, G.A.D. Briggs, B.B. Buckley, D.D. Awschalom, and R.J. Schoelkopf, *High-Cooperativity Coupling of Electron-Spin Ensembles to Superconducting Cavities*, Phys. Rev. Lett. **105**, 140501 (2010)

[185] Robert Nelson and M.G. Olsson, *The pendulum - Rich physics from a simple system*, American Journal of Physics **54**, 112 (1986)

[186] Karlheinz Ochs, *A comprehensive analytical solution of the nonlinear pendulum*, European Journal of Physics **32** 2 (2011)

[187] G. Bertotti, I.D. Mayergoyz, and C. Serpico, Phys. Rev. Lett. **87**, 217203 (2001)

[188] P.W. Anderson and H. Suhl, Phys. Rev. **100**, 1788 (1955)

[189] M.T. Weiss, Phys. Rev. Lett. **1**, 239 (1958)

[190] Y.S. Gui, A. Wirthmann, and C.-M. Hu, *Foldover ferromagnetic resonance and damping in permalloy microstrips*, Phys. Rev. B **80**, 184422 (2009)

[191] P.A.P. Janantha, B. Kalinikos, and M. Wu, *Foldover of nonlinear eigenmodes in magnetic thin film based feedback rings*, Phys. Rev. B **95**, 064422 (2017)

[192] M. Aspelmeyer, T.J. Kippenberg, and F. Marquardt, *Cavity optomechanics*, Rev. Mod. Phys. **86**, 1391 (2014)

[193] S. Huang and G.S. Agarwal, *Enhancement of cavity cooling of a micromechanical mirror using parametric interactions*, Phys. Rev. A **79**, 013821 (2009)

[194] Y.C. Liu, Y.F. Xiao, X. Luan, and C.W.Wong, *Dynamic Dissipative Cooling of a Mechanical Resonator in Strong Coupling Optomechanics*, Phys. Rev. Lett. **110**, 153606 (2013)

[195] Y.-P. Wang, G.-Q. Zhang, D. Zhang, T.-F. Li, C.-M. Hu, and J.Q. You, *Bistability of Cavity Magnon Polaritons* Phys. Rev. Lett. **120**, 057202 (2018)

[196] B.M. Yao, Y.S. Gui, Y. Xiao, H. Guo, X.S. Chen,W. Lu, C.L. Chien, and C.-M. Hu, *Theory and experiment on cavity magnon-polariton in the one-dimensional configuration* Phys. Rev. B **92**, 184407 (2015)

[197] N.N. Bogoliubov and Y.A. Mitropolski, *Asymptotic methods in the theory of non-linear oscillations*, New York: Gordon and Breach (1961) (translated from Russian)

[198] John Kerr, *A new relation between electricity and light: Dielectrified media birefringent*, Philosophical Magazine **50**, 332: 337-348 (1875)

[199] P. Weinberger, *John Kerr and his Effects Found in 1877 and 1878*, Philosophical Magazine Letters **88**, 12: 897-907 (2008)

[200] M. Harder, Y. Gui, and C.-M. Hu, *Electrical detection of magnetization dynamics via spin rectification effects*, Phys. Rep. **661**, 1 (2016)

[201] Michael Harder, Lihui Bai, Paul Hyde, and Can-Ming Hu, *Topological properties of a coupled spin-photon system induced by damping*, Phys. Rev. B **95**, 214411 (2017)

[202] Bimu Yao, Y.S. Gui, J.W. Rao, S. Kaur, X.S. Chen, W. Lu, Y. Xiao, H. Guo, K.-P. Marzlin, and C.-M. Hu, *Cooperative polariton dynamics in feedback-coupled cavities*, Nature Communications **8**, 1437 (2017)

[203] S. Haroche and J.-M. Raimond, *Exploring the Quantum: Atoms, Cavities, and Photons* (Oxford University Press, 2006)

[204] M. Aspelmeyer, T.J. Kippenberg, and F. Marquard, *Cavity Optomechanics*, edited by M. Aspelmeyer, T. J. Kippenberg, and F. Marquardt (Springer, Berlin, Heidelberg, 2014)

[205] M. Aspelmeyer, T.J. Kippenberg, and F. Marquardt, Rev. Mod. Phys. **86**, 1391 (2014)

[206] D.F. Walls and G.J. Milburn, *Quantum Optics*, 2nd ed. (Springer, 2008)